



University of HUDDERSFIELD

University of Huddersfield Repository

Jorge, Pedro

Modelling and enhancing track support through railway switches & crossings

Original Citation

Jorge, Pedro (2020) Modelling and enhancing track support through railway switches & crossings. Doctoral thesis, University of Huddersfield.

This version is available at <http://eprints.hud.ac.uk/id/eprint/35561/>

The University Repository is a digital collection of the research output of the University, available on Open Access. Copyright and Moral Rights for the items on this site are retained by the individual author and/or other copyright owners. Users may access full items free of charge; copies of full text items generally can be reproduced, displayed or performed and given to third parties in any format or medium for personal research or study, educational or not-for-profit purposes without prior permission or charge, provided:

- The authors, title and full bibliographic details is credited in any copy;
- A hyperlink and/or URL is included for the original metadata page; and
- The content is not changed in any way.

For more information, including our policy and submission procedure, please contact the Repository Team at: E.mailbox@hud.ac.uk.

<http://eprints.hud.ac.uk/>

Modelling and enhancing track support through railway switches & crossings

Pedro Filipe Mascarenhas Jorge

A thesis submitted to the University of Huddersfield in partial fulfilment of the requirements of the degree of Doctor of Philosophy

Institute of Railway Research
School of Computing and Engineering
University of Huddersfield

November 2020

To my parents
and brother

Executive Summary

Railway turnouts, also known as Switches and Crossings (S&Cs), are important systems in the railway network that enable railway vehicles to change routes. Nevertheless, severe impact loads occur when the vehicle negotiates a turnout due to the wheel load transfer from one rail to another, which leads to high maintenance costs. In turn, the design of S&Cs is currently a complex task for which the development of accurate computational models represents a great value not only to better investigate the vehicle-turnout interaction but also to support the design of turnouts.

This thesis proposes a complete computational study that includes: the development of a detailed model of a railway crossover; model calibration against site measurements; performance assessment of the crossover; and proposing alternative designs that enhance the resistance to damage.

Different track models are compared to select the most suitable one to study S&Cs. A UK site with Under Sleeper Pads (USPs) is the case study considered in this thesis and a numerical model is built using the track model selected. Two measurement campaigns, one performed in 2016 and the other in 2019, are used in this work, comprising bearer displacements measured at the switch and crossing panels. Every 2 bearers on the cress side and a few bearers on the 6ft side of the track were recorded on the first campaign. The model trackbed stiffnesses are calibrated against the site measurements and a good agreement is achieved. The data from the second campaign showed an increase in displacements that most likely indicate the existence of voided bearers. Also, from observations in situ and photos taken from the site, it was possible to assume that some of the connection devices between bearers of the two tracks were damaged. This required changes to be made on the proposed model developed, including the consideration of bearer flexibility and the use of non-linear force elements to model the varying trackbed stiffness and accommodate voids underneath the bearer. A new calibration of the model is performed but reducing the trackbed stiffness was not enough to reach the level of displacements measured. An incremental process of the model development is then used, considering voids under the bearers, removing the connection from bearers where loose bolts were spotted and considering some level of flexibility at the other connections rather than assuming they are rigid as initially intended. Finally, the reduction of the trackbed stiffness of the second track was included to simulate the hypothesis of voids being present at that track. From all these changes, the voided bearers

and the low stiffness of the connection are the ones that lead to the biggest increase of the displacements.

The calibrated model is then used to investigate the effect of different turnout characteristics, such as, the variation on track stiffness due to the S&C components, the use of USPs and alternative bearer connections. Thus, several numerical simulations of a typical railway vehicle running over a turnout have been carried out. Here, special attention has been given to the wheel-rail contact forces, which leads to wear of the rails, to the reaction forces on the bearer connection, which leads to its failure, and to the forces transmitted to the ballast, which leads to track settlement. The choice of installing two different types of USPs on the site has been investigated and concluded that they do not offer an ideal smoothing of the track stiffness. Yet, they reduce the ballast forces, particularly in the areas with the higher transient loads. Regarding the bearer connections, it is concluded that high reaction forces occur around the crossing nose and the load transfer area at the switch panel, which justifies their failure. Two alternative connection designs are studied, namely the “pinned” and the “sandwich” joints. It has been concluded that the sandwich joint reduces the stresses on the connection device and thus would improve its reliability, although higher displacements would occur, which can lead to faster development of voids.

Acknowledgements

I would like to thank all people who contributed to both my professional and personal growth.

First, I would like to thank my main Supervisor Dr Yann Bezin for all the support and guidance. He was always happy to assist and support me throughout the whole process. This work is a continuation of his PhD work and I learned so much from him during the past four years.

Second, I would like to thank my external advisor Dr Sergio Neves who was present from the beginning and who told me about this PhD opportunity. He was more than a supervisor, he was a true friend who helps me to get work done.

Lastly, I would like to thank my second Supervisor Dr Hugo Magalhães, which entered last on my supervising team, but was always so passionate to support and was a crucial help to finish this work.

A special thanks to Dr Ilaria Grossoni, who I worked directly on some tasks from this research and in other projects. Since I arrived at the IRR, she was always very supportive.

Many thanks also to Prof Simon Iwnicki for providing always well-thought advises.

To all the IRR staff and ex-staff, but in particular, those who help me and supported my work, I would like to acknowledge Dr Dimitrios Kostovasilis, who was part of my supervising team and he is a good friend and Dr Samuel Hawksbee, who I have been working with in the past year.

In addition to that, I would like to acknowledge the UK EPSRC project Track to the Future (grant agreement no. EP/M025276/1) and the University of Southampton to fund my work.

Lastly, but absolutely not least, thanks to my amazing parents and my brother, for their daily encouragement. They were always the first to believe and support me with the decision of doing a PhD.

Table of Contents

Executive Summary	ii
Acknowledgements	v
Table of Contents	vii
List of Figures	xi
List of Tables.....	xvii
1 Introduction	1
1.1 Aims of the research	2
1.2 Objectives	2
1.3 Methodology	3
1.4 Novelty of the research	4
1.5 Contents of the thesis	5
1.6 Acknowledgement of contribution	6
2 Background and Literature review	7
2.1 Ballasted track.....	7
2.1.1 <i>Components of the ballasted track</i>	7
2.1.2 <i>Track composite stiffness</i>	9
2.2 Switches and Crossings	10
2.2.1 <i>Switch panel</i>	13
2.2.2 <i>Crossing panel</i>	15
2.2.3 <i>Degradation methods at S&Cs</i>	17
2.3 Vehicle-Track Interaction models	18
2.3.1 <i>Finite Element approach</i>	19
2.3.2 <i>Multibody Systems approach</i>	20
2.3.3 <i>Coupling FE and MBS</i>	22

2.3.4	<i>The wheel-rail contact problem</i>	22
2.3.5	<i>Switches & crossing studies</i>	23
2.3.6	<i>Complementary literature on S&C</i>	25
2.3.7	<i>Summary</i>	27
3	Development of flexible track models using multibody formulation	29
3.1	Track models description	29
3.1.1	<i>Model a: Continuous supported track model</i>	29
3.1.2	<i>Model b: Discretely supported track model - beam element</i>	32
3.1.3	<i>Model c: Discretely supported track model - modal decomposition method</i>	37
3.1.4	<i>Model d: In-house vehicle-track interaction model built in MATLAB</i>	40
3.2	Selection of the track model to study S&C	41
3.2.1	<i>Case study</i>	41
3.2.2	<i>Results for single wheelset</i>	45
3.2.3	<i>Results for Manchester passenger vehicle</i>	53
3.2.4	<i>Summary of results</i>	56
3.3	Conclusions	57
4	Numerical modelling of a railway crossover	61
4.1	General description.....	61
4.2	Numerical model and mechanical properties	63
4.2.1	<i>The rails</i>	64
4.2.2	<i>Sleepers and bearers</i>	66
4.2.3	<i>Fastening and trackbed support</i>	68
4.2.4	<i>Output and track file creation</i>	69
4.3	VI-Rail crossover model	71
4.3.1	<i>Numerical model in VI-Rail</i>	71
4.3.2	<i>Track irregularities (TRC data)</i>	73

4.4	Long bearers flexibility in VI-Rail	74
4.4.1	<i>Hypothesis</i>	74
4.4.2	<i>Methodology</i>	74
4.4.3	<i>Validation against ANSYS</i>	75
4.5	Discussion	80
5	Calibration of the railway crossover model	83
5.1	Model calibration for the first campaign	83
5.1.1	<i>Site measurements description</i>	83
5.1.2	<i>Assumptions from the numerical model used</i>	86
5.1.3	<i>Model calibration</i>	87
5.2	Model calibration for the second campaign	93
5.2.1	<i>Site measurement description</i>	93
5.2.2	<i>Adjustments of the crossover model</i>	98
5.2.3	<i>Model calibration</i>	100
5.3	Conclusions	110
6	Application of calibrated model to crossover design	113
6.1	The influence of Track bed Stiffness	114
6.2	Design choice for Under Sleeper Pads	119
6.3	Degradation around the bearer connections	123
6.4	Alternative design to the long bearer connection	128
6.4.1	<i>Pinned joint</i>	128
6.4.2	<i>Sandwich joint</i>	131
6.5	Conclusions	134
7	Conclusions and further work	137
7.1	Conclusions	137
7.2	Future work	141

References.....	143
Appendix A.....	153
Appendix B.....	154

List of Figures

Figure 1.1 – Diagram with methodology	4
Figure 2.1 – Ballasted track scheme.....	7
Figure 2.2 – Composite stiffness scheme	10
Figure 2.3 – Top view of a turnout system	10
Figure 2.4 – Overview of switch panel including the switch rails and switching machines.....	14
Figure 2.6 – Overview of the crossing panel with a cast monoblock crossing.	15
Figure 2.9 –Continuously supported beam on a spring foundation with the rail deformation represented in a dashed line [4].....	19
Figure 2.10 – Four layers discretely supported ballasted track (adapted from [31])	20
Figure 2.11 – Continuous track model implemented in: a) VAMPIRE and b) VI-Rail.	21
Figure 3.1. Cross-section of the continuous track model used in VI-Rail: a) front view; b) side view (adapted from [4]).	30
Figure 3.2. Sleeper UDE: a) front view; b) side view (adapted from [4]).	33
Figure 3.3. ADAMS beam element used to connect two rigid bodies.....	34
Figure 3.4. Deformed rail beam calculation (adapted from [4]).	36
Figure 3.5. Shape functions to: a) force distribution; b) torque distribution.....	37
Figure 3.6. Flexible body animation tool – first 5 vertical bending modes of the rail beam.	40
Figure 3.7. FE model built in MATLAB (adapted from [38]).....	41
Figure 3.8. Schematic representation of the vertical irregularity.	42
Figure 3.9. VI-Rail discretely supported track model: a) ADAMS beam; b) MNF.	44
Figure 3.10. Track model scheme.	44
Figure 3.11. Effect of VI-Rail damping ratio in the contact algorithm using the discretely supported track model.	45
Figure 3.12. Contact forces of VI-Rail track model using MNF.	46
Figure 3.13. Vertical contact force of single wheelset for total irregularity.	47

Figure 3.14. Vertical contact forces of single wheelset for: a) medium wavelength irregularity; b) short wavelength irregularity.	48
Figure 3.15. Vertical wheel displacements of single wheelset for total irregularity.	48
Figure 3.16. Vertical wheel displacements of single wheelset for: a) medium wavelength irregularity; b) short wavelength irregularity.....	49
Figure 3.17. Vertical sleeper displacements for: a) and b) total irregularity; c) and d) medium wavelength irregularity; e) and f) short wavelength irregularity.	51
Figure 3.18. Vertical contact forces for up to four beam elements: a) and b) discretely supported track using ADAMS beam; c) and d) discretely supported track using MNF.	52
Figure 3.19. Vertical contact forces of Manchester Passenger vehicle for: a) and b) total irregularity; c) and d) medium wavelength irregularity; e) and f) short wavelength irregularity.....	55
Figure 3.20. Vertical sleeper displacements for Manchester Passenger vehicle for: a) and b) total irregularity; c) and d) medium wavelength irregularity; e) and f) short wavelength irregularity.....	56
Figure 4.1. Schematic plan of the study site (adapter from [91]).	61
Figure 4.2. a) The switch panel and b) the two southern crossings. Both photos were taken pointing north [5].	62
Figure 4.3. Site overview. The numbered bearers identify monitored locations [92].	63
Figure 4.4. Rail CEN56E1 (mm).....	65
Figure 4.5. Cross-sections locations from the crossing	66
Figure 4.6. Scheme of concrete sleeper type G44 (m).....	67
Figure 4.7. 56E1 Rail profiles for: a) CV Switch and b) Full cant crossing 1 in 9.25 [21, 97].....	71
Figure 4.8. Full railway crossover modelled in VI-Rail	72
Figure 4.9. Detailed view from: a) Switch and b) crossing	72
Figure 4.10. Track irregularities for both rails on: a) vertical and b) lateral planes.	73
Figure 4.11. Long bearer model: a) rigid, b) semi-flexible type 1 (bearer 38 to 49) , c) semi-flexible type 2 (bearer 50 to 53) and d) semi-flexible type 3 (bearer 54 to 65)	75
Figure 4.12. Long bearer model comparison: a) VI-Rail rigid model, b) VI-Rail semi-flexible model and c) ANSYS flexible model	76

Figure 4.13. Long bearer support distribution.....	77
Figure 4.15. Long bearer vertical bending modes for frequencies below 100Hz	78
Figure 4.16. Long bearer vertical bending modes for frequencies above 100Hz	79
Figure 4.17. Long bearer displacements considering constant support stiffness	80
Figure 5.1. Locations monitored on the UK site (adapted from [91]).	84
Figure 5.2. Monitored locations at a) zone 1 at the switch panel and b) zone 2 at the crossing panel [5].	84
Figure 5.3. Deflection time trace for a Class 91 locomotive hauling nine Mark IV coaches and one DVT (adapted from [5]).	85
Figure 5.4. Bearer movements for the third axle of the fifth Mark IV coach [5]......	86
Figure 5.5. Mark IV coach and crossover assembly in VI-Rail.	86
Figure 5.6. Transversal cross-section of a long bearer in (a) VTI model and (b) VI-Rail [5].	87
Figure 5.7. Iterative process to tune the trackbed stiffness.	88
Figure 5.8. Bearer displacements along the switch panel: a) on the cress side; b) on 6ft side.....	91
Figure 5.9. Vertical contact forces along the switch panel: a) on the cress side; b) on 6ft side.....	91
Figure 5.10. Bearer displacements along the crossing panel: a) on the cress side; b) on 6ft side.....	92
Figure 5.11. Vertical contact forces along the crossing panel: a) on the cress side; b) on 6ft side....	93
Figure 5.12. Average measured bearer deflections obtained from bearer vibration measurements collected from UoS.....	95
Figure 5.13. Comparison from bearer deflections of first and second campaigns for: a) switch panel; b) crossing panel.....	96
Figure 5.14. Site pictures from the second campaign (photos taken from UoH).....	98
Figure 5.15. Non-linear bushing element characteristic with preload.	99
Figure 5.16. Effect on the displacement from using linear and non-linear force elements underneath the long bearer.	100
Figure 5.17. Objective function evolution.	101
Figure 5.18. Bearer displacements after tuning trackbed stiffness on: a) cress side; b) 6ft side.....	102

Figure 5.19. Vertical trackbed stiffness after tuning of both sides of track.....	103
Figure 5.20. Gap values to use on: a) cess side; b) 6ft side.....	104
Figure 5.21. Void distribution below each bearer model type.....	105
Figure 5.22. Non-linear bushing with gap.....	106
Figure 5.23. Effect on the bearer displacements from considering or not the void underneath.....	107
Figure 5.24. Diagram with calibration steps.....	107
Figure 5.25. Final bearer displacements from different cases studied.....	110
Figure 6.1. Composite stiffness for two different trackbed stiffness: 20 and 40 kN/mm.....	115
Figure 6.2. Vertical contact forces from the front Wheelset of the Mark IV coach, on the 6ft side for two trackbed stiffness of 20 and 40 kN/mm	116
Figure 6.3. Ballast forces underneath the rails of Down through route for two different trackbed stiffness: 20 and 40 kN/mm.....	117
Figure 6.4. Vertical force a) and torque b) at the connection for different trackbed stiffness, 20 and 40 kN/mm	118
Figure 6.5. Maximum bearer displacements for two different trackbed stiffness: 20 and 40 kN/mm.....	119
Figure 6.6. Composite stiffness considering constant trackbed stiffness equal to 40 kN/mm and two different USP distributions for: a) cess side and b) 6ft side.....	121
Figure 6.7. Vertical contact forces from the front wheelset of Mark IV coach, a constant trackbed stiffness equal to 40 kN/mm and two different USP distributions for: a) and b) switch panel and c) and d) crossing panel.....	122
Figure 6.8. Ballast forces for Mark IV coach passage, a constant trackbed stiffness equal to 40 kN/mm and two different USP distributions on: a) cess side b) 6ft side.....	123
Figure 6.9. Composite stiffness considering constant trackbed stiffness equal to 40 kN/mm and a series of gap of 3 mm.....	125
Figure 6.10. Vertical contact forces from the front wheelset of Mark IV coach on the 6ft side considering a constant trackbed stiffness equal to 40 kN/mm and a gap of 3 mm.....	125
Figure 6.11. Effect of voided sleepers on a) bearer displacements and b) ballast forces.....	126

Figure 6.12. Effect of voided bearers on the reaction a) forces and b) torques of the bearer connections.....	127
Figure 6.13. Composite stiffness considering constant trackbed stiffness equal to 40 kN/mm and a gap of 3 mm.....	128
Figure 6.14. Pinned-pinned joint.....	128
Figure 6.15. Maximum bearer displacements for Mark IV coach considering the rigid connection and the pinned-pinned connection.....	129
Figure 6.16. Bearer deformation for the maximum displacement under the 6ft rail caused by the passage of Mark IV coach considering the rigid connection and the pinned connection.	130
Figure 6.17. Deformation of the bearer underneath the crossing nose using the rigid and pinned-pinned connections.	131
Figure 6.18. Sandwich type joint.	131
Figure 6.19. Maximum bearer displacements for Mark IV coach considering sandwich joint and for a) cess side; b) 6ft side.	132
Figure 6.20. Deformation of the bearer underneath the crossing nose for the sandwich joint.....	133
Figure 6.21. Effect of the connection stiffness properties on the a) forces and b) torques transmitted to the connection.	133
Figure 6.22. Effect of the connection stiffness properties on the ballast force on the 6ft side of the Down track. b) shows a zoom around the crossing nose.	134
Figure A.1. Receptance curves [4].	153

List of Tables

Table 2.1. S&C layout designation [15].....	11
Table 2.2. Turnout combinations [15].....	12
Table 2.3. Crossing classification	12
Table 3.1. Track input parameters.....	44
Table 3.2. Summary of peak results	57
Table 4.1. Stock rail properties	65
Table 4.2. Crossing element properties relative to stock rail	66
Table 4.3. Model pad and ballast stiffness and damping parameters.....	69
Table 5.1. Final differences and trackbed stiffness values from calibration 1 [5].	90
Table A.1. Receptance peak frequencies [4].....	153
Table B.1. Final differences and trackbed stiffness values from switch panel for calibration 2. ...	154
Table B.2. Final differences and trackbed stiffness values from crossing panel for calibration 2..	155

1 INTRODUCTION

Railway track has been experiencing a rising demand for passenger and freight capacity associated with higher traffic, speeds and axle loads. In addition, the time available for maintenance is decreasing and pressure is growing to reduce cost and environmental impacts, including noise and vibration. Also, guaranteeing a higher level of passenger satisfaction is another challenge of the railway industry.

This research is part of the project Track to the Future (T2F), which is a prestigious programme funded by EPSRC and which involves the universities of Huddersfield, Southampton, Birmingham and Nottingham and key railway stakeholders such as Network Rail and Progress Rail. The key objectives and research challenges of the T2F programme are: 1) development of a low-maintenance, long-life track system with optimised material use in terms of whole life cost and embedded carbon; 2) design of crossings and transitions in order to optimise vehicle behaviour and hence maximise resistance to damage and 3) develop an integrated approach to designing a low-noise and vibration track. The present work is linked with the first two research challenges.

Switches and Crossings (S&Cs) are important elements of the railway track which confer versatility to the traffic and allow railway lines to converge, diverge or intersect. The railway network is extremely influenced by the number of S&C elements [1]. The simplest S&C layout, also called turnout allows the train to diverge from the main line. It is divided into the switch panel with all the movable parts that allow the train to change direction, the crossing panel where the two tracks intersect and the closure panel located between the other two.

Along the S&C panels, severe impact loads occur in the wheel-rail interaction area, which leads to local damage on the wheel and rail surfaces and transmission of noise and vibrations to the environment. Therefore, turnout components, such as the rails and connection of bearers, experience the highest number of failures [2, 3]. From a track designer's and infrastructure manager's point of view, these impact loads observed in turnouts must be minimised to reduce maintenance costs, noise and vibration. Hence, the development of computational models to represent the train-turnout interaction are of crucial importance to

support the design processes and provide a better understanding of the influence of key parameters.

1.1 AIMS OF THE RESEARCH

The main aims of this research are analysing the effects of the non-homogeneous track support stiffness at railway switches and crossings on the vehicle-track system, understanding the main degradation mechanisms at the switch and crossing panels, and studying alternative solutions to optimise their performance. This implicates the development of a detailed numerical model capable of representing the full S&C and its calibration against site measurements. The S&C model must be capable of representing the degradation observed in site measurements and allow to study and optimise the performance of alternative track designs.

1.2 OBJECTIVES

The main objectives of this research work are:

1. Understand which type of track modelling approach should be considered to accurately take into account the varying support stiffness and rail section along the S&Cs. This includes a literature review of the existing methodologies for analysing the vehicle-track interaction, with a specific focus on S&C models.
2. Select a S&C site to use as a case study and build a numerical model using the track model selected. The model should account for the varying properties, potential non-linearities and component flexibility that exist in a S&C.
3. Calibrate the track model against site measurements available.
4. Identify the main degradation mechanism on the site and update the model to capture their effect.
5. Application of the calibrated model to:
 - Study the role of the track support stiffness and the contribution of the different track elements to the variability of the entire system response to load. Analyse how this affects the contact forces.

- Support the understanding of the influence of using under sleeper pads in S&Cs and the rationale behind their specific properties.
- Investigate the influence of long bearers in crossing panels and support the scientific understanding of different existing solutions for connecting them between two adjacent tracks.

1.3 METHODOLOGY

The main steps adopted in this thesis, which are directly related to the objectives listed in section 1.2, are as follows (Figure 1.1):

1. A vehicle-track interaction models benchmark is carried out, comparing different approaches to evaluate the dynamic behaviour of the vehicle-track system under the impulse of a short wavelength irregularity. From that comparison, a discretely supported track model is selected to build the full railway crossover.
2. A UK site equipped with Under Sleeper Pads (USPs) is selected as a case study. The full crossover is built in AutoCAD, and its geometry exported to the selected MBS software VI-Rail. The model considers all the bearer positions, the two main lines joined by the crossover and the diverging line.
3. The trackbed stiffnesses from the model are calibrated against site measurements from a first campaign done in 2016.
4. A second campaign has shown large bearer deflections in key areas of the S&C and in particular at the crossing panel. The crossover model is adjusted to better match the obtained bearer displacements. This includes the consideration of the flexibility from the bearers joining the two tracks, the inclusion of voided bearers and degraded connections to the areas with very big displacements.
5. With such a complex model, it is possible to perform studies involving: the variation of the track stiffness due to the S&C components; the effect on the contact forces, ballast stresses and forces transmitted to the connection from considering different trackbed stiffnesses; and the effect of the USPs. Additionally, alternative designs solutions for the connection between the bearers from the two tracks are analysed to understand their impact on the overall crossover behaviour.

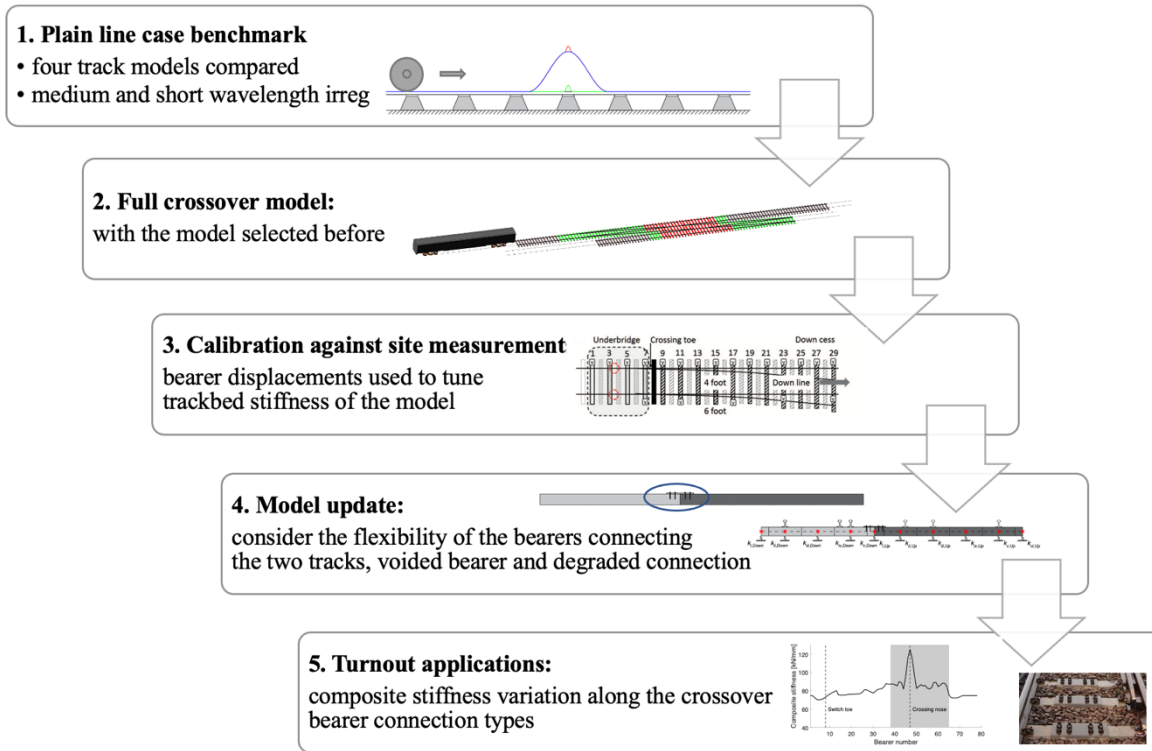


Figure 1.1 – Diagram with methodology

1.4 NOVELTY OF THE RESEARCH

The novelty of this research starts with the methodology applied here. There are only a few studies that model the whole system (track, vehicle and wheel-rail contact) in detail for S&C situations entirely in a multibody system (MBS) environment, thus offering reasonable simulation speed. Although some of the methodologies used here can be found in the literature, they are not readily accessible or are not always directly usable to S&C problems.

The methodology used here is entirely built in a commercial MBS software, which makes it applicable by any user, including the track designers and infrastructure managers. The methodology was initially created by [4] and was extended to S&Cs in this research work.

An efficient and versatile process is developed here, allowing to build different types of track layout very fast. A full crossover numerical model is built here, where all the different tracks were considered, and the bearers are placed in the right places with their different sizes and flexibility considered. The variable rail properties from the switch, crossing and other components from the S&C layout are considered. This is the 1st model of its kind to investigate and enable the modelling of such a complex S&C layout.

From the site measurements of two campaigns spaced of three years, it was allowed not only to tune the support stiffness of the numerical model against the bearer movements recorded, but to understand the stiffness conditions underneath the entire crossover layout. The model allowed to prove the evolution that occurred at the site in those three years. This included voided bearers and broken connection between bearers, based on the observations of the track rolling towards the centre of the two tracks and connections showing loosed bolts.

The model allowed to understand better the stiffness variability that the vehicle experiences when traversing the crossover and to study the different types of fixing used in Europe and the UK and established the fundamental differences between them. The methodology presented here proved to be an invaluable tool to support the future design of optimum fixings, S&C layouts and its components.

1.5 CONTENTS OF THE THESIS

Chapter 2 provides a detailed description of the main characteristics of the switch and crossing panels, different S&C layouts and their classification. Then, a literature review on track models, dividing them by models built using MBS, FE or coupling both approaches. A particular focus is given to the studies related to S&C. A brief description of the main degradation mechanisms observed in S&Cs is given.

In chapter 3, different track models are presented and compared. The responses of each model under the impulse of a short wavelength irregularity are discussed, where wheel-rail contact forces and sleeper displacements are used for the comparison analysis. In the end, the advantages and disadvantages of each model are numbered and the most suitable model to study an S&C is selected.

Chapter 4 has a detailed explanation of the UK site used as a case study. All the steps to build the track model in VI-Rail are described. This chapter also describes the methodology considering the flexibility of the long bearers.

Chapter 5 has a detailed description of the site measurements from two campaigns performed in 2016 and 2019. The trackbed stiffness of the crossover model is tuned against the measured displacements of the bearers. This chapter also presents the adjustments of the model from Chapter 4 to represent the degradation observed at the site.

In chapter 6, the model created in the previous Chapters 4 and 5 is used to study the non-homogeneous stiffness of the railway crossover. The choice of using USPs and alternative solutions to the bearer connections are also assessed.

Finally, the main conclusions and suggestions for further work are summarised in Chapter 7.

1.6 ACKNOWLEDGEMENT OF CONTRIBUTION

Paper A: This thesis has contributed to the publication of the paper entitled “**The role of support stiffness in switches and crossings: comparison of vehicle-track interaction models against field measurements**” – published in Part F: Journal of Rail and Rapid Transit [5].

The main contributions of the author were the development of a complete crossover that validate with other vehicle-track interaction model with simpler track and vehicle designs. The model was used to test the trackbed stiffnesses obtained from the simpler model where wheel-rail contact forces and bearer displacements were compared. The author also helped with the writing up and editing of the paper.

Paper B: This thesis has also contributed to the publication of the paper entitled “**Modelling Track Flexibility in Turnouts Using MBS Approach**” – presented in IAVSD 2019: Advances in Dynamics of Vehicles on Roads and Tracks conference and published in a book named Advances in Dynamics of Vehicles on Roads and Tracks from Springer International Publishing [6].

The author did all the modelling in VI-Rail and the dynamic analysis, comparing contact forces from all the models. The author also did the writing up and editing of the paper.

2 BACKGROUND AND LITERATURE REVIEW

A detailed description of switches and crossings on ballasted track is presented first in this chapter, where the focus is put on a single turnout, composed by the switch, closure and crossing panels. Then, a state-of-the-art of vehicle-track interaction models and their applications in S&Cs is discussed.

2.1 BALLASTED TRACK

The ballasted railway track is often found in railway networks comprising interesting characteristics such as easy maintenance and low cost to build compared to other solutions, capability to mitigate ground vibrations and good performance at draining. Track design engineers often prefer the use of the ballasted track due to the greater experience that has been gained with its use [7]. Other track configurations can be found, such as slab tracks, but the work presented here is focused on a turnout in ballasted track.

Figure 2.1 shows the scheme of a ballasted track. This typical railway track can be split into superstructure and substructure. The superstructure comprises the elements above the ballast that are the rails, sleepers, rail pads and the fastening system, whereas the substructure comprises the ballast, sub-ballast and subgrade [8].

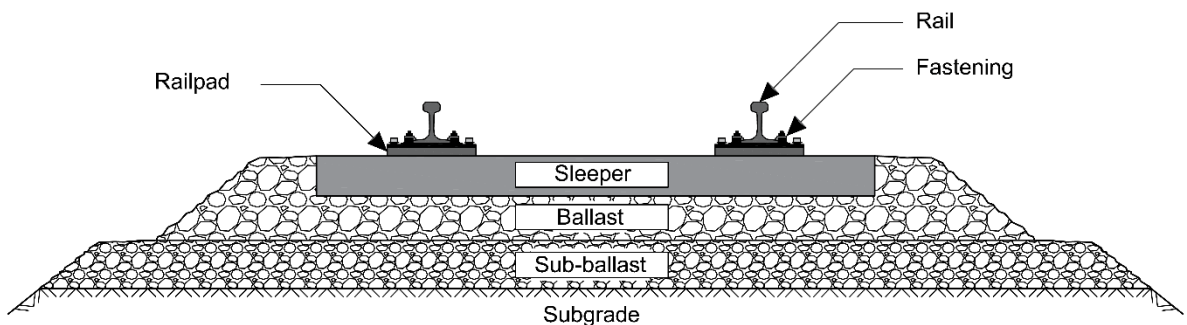


Figure 2.1 – Ballasted track scheme

2.1.1 Components of the ballasted track

The rail is in contact with the wheels of the train, directing its trajectory and receiving the vertical and the transversal axle loads and also the longitudinal forces such as braking. The

rail behaves like a discretely supported beam with high bending stiffness. The rail and sleeper are connected through a fastening system that assures the right position of the rail and an adequate load distribution by the sleepers. The distance between the inner faces of the rails is the gauge. The standard gauge which, is 1.435 m, is found in the majority of the European railway networks, such as, in the UK and in the European High-speed train lines. The rail cross-section for a given track is selected depending on the typical operating speed and axle load, for instance, the UIC60 rail profile, which weights 60 kg per meter, is frequently used in high-speed lines [9].

The sleepers give support to the rails, guarantee the track alignment and distribute the load to the ballast. Sleeper length varies typically between 2.3 m and 2.6 m. In S&Cs the sleepers are named as bearers and can be longer than the normal sleepers for plain track.

Pads are installed between the sleepers and rails to protect the sleeper from impact loads and filter higher vibrations due to the wheel-rail contact. The stiffness of the pad plays a key role in distributing the axle load across the sleepers. In Europe, the pad stiffness of rail pads varies between 27 and 500 kN/mm [10].

The sleepers rest on the ballast layer, which constrains their vertical, lateral and longitudinal displacements. The ballast layer provides a load distribution from the superstructure and the soil underneath, confers some damping to the track and gives some draining capabilities to the track. Ballast and sub-ballast height varies between 0.20 and 0.50 m each. The mechanical properties of the ballast layer depend on the type of material used, i.e., particle dimensions and specific weight *in situ*, and the compactness of the material, subsequent from the mechanical compaction in the installation process and the natural compaction resulting from the rail traffic [10].

The sub-ballast layer has similar functions like the ballast layer with the extra job of preventing the migration of small particles to the ballast layer. Usually, the particle size is intermediate between the neighbouring layers.

The subgrade layer gives support to the other layers. In the case where the soil is not capable of receiving the loads from the track and traffic, the use of geotechnical retrofitting techniques is required to improve support stiffness and resistance to long-term settlements. In this thesis and when no information is available from the layers underneath the ballast,

the ballast, sub-ballast and subgrade can be grouped in only one spring-damper with the equivalent stiffness and damping values, which is named as trackbed stiffness.

Although the ballasted track has not evolved significantly, some of its components have been modified over the years to improve the reliability and safety of the track, such as [11]:

- Pre-stressed concrete or steel sleepers replace timber sleepers as it gives better support for the rail, track stability and higher durability. Also, different designs were suggested over the years to maximize its efficiency to transmit the load from the rail to the ballast;
- Optimisation of the rail head geometry and the section shape for an enhanced wheel-rail contact condition and load bearing capacity;
- Optimisation of rail pads and fastenings to provide better attenuation of the wheel-rail contact forces and noise;
- Improvement of techniques for the ballast layer maintenance, such as stone blowing and tamping machines, which correct track alignment and longitudinal level and use of new materials for the ballast and sub-ballast layers;
- The use of under sleeper pads, geogrids and geosynthetics at the interface between the different layers (sleeper to ballast, ballast to sub-ballast and sub-ballast to subgrade) to improve the overall track resilience and resistance to settlements.

2.1.2 Track composite stiffness

The support stiffness of a railway track is formed from the combined effects of the bending stiffness of the rails and the vertical support of the rail-pad and trackbed, as shown in Figure 2.2. The composite stiffness, which is defined here as the ratio between the wheel vertical load (F) and the rail vertical displacement (δ), can be used to assess the stiffness variation on S&Cs. Note that the force F and vertical displacement δ is depicted in Figure 2.2. The track components which form composite stiffness can be categorised between those that are well controlled and those that are less well controlled. The first ones are the components from the superstructure such as the rail bending stiffness and railpad vertical stiffness, while the second ones are the ones from the substructure, such as the ballast and other soil layers (grouped and named as trackbed).

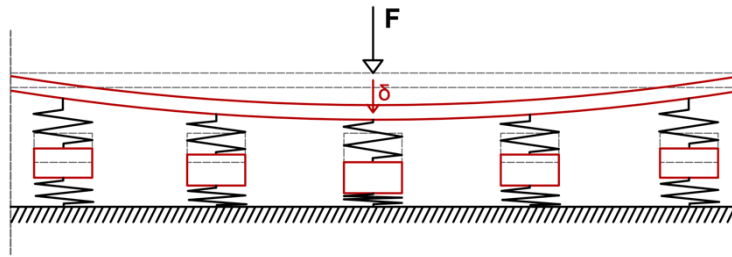


Figure 2.2 – Composite stiffness scheme

In a plain line, the composite stiffness variability depends mainly on the trackbed stiffness, which has been shown to vary significantly [12-14]. In the case of a turnout, the sleepers properties and rail sections play also a role in the composite stiffness [5].

2.2 SWITCHES AND CROSSINGS

Switches & Crossings (S&C), also called turnouts, are mechanical systems that enable railway vehicles to be guided from one track to another, such as at a railway junction. A turnout is composed of a switch panel, a crossing panel, and a closure panel (see Figure 2.3). The switch panel consists of two movable switch rails, switching machines, and two stock rails, which guides the vehicle to the through or diverging route. The crossing panel allows the intersection of two tracks at the same level. The closure panel makes the link between the switch and the crossing panels.

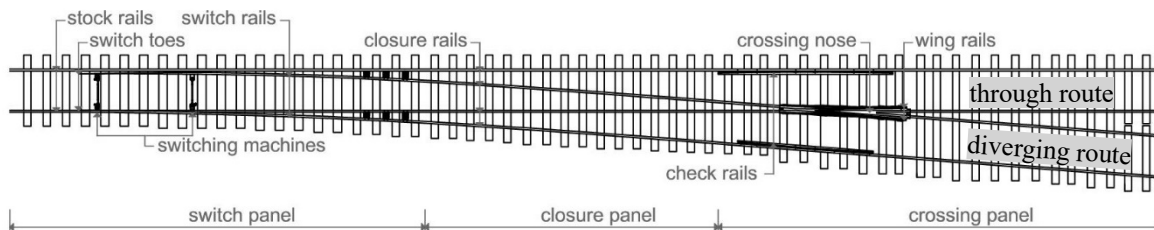
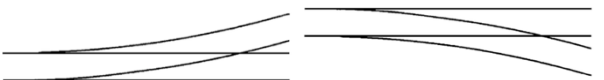
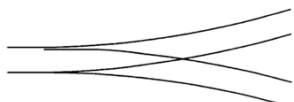
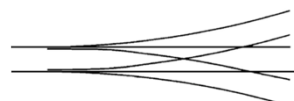
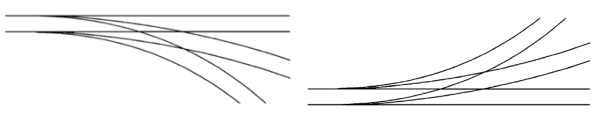
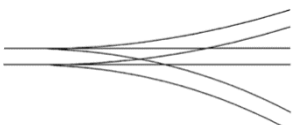


Figure 2.3 – Top view of a turnout system

On the turnout shown in Figure 2.3, there are four possible ways to negotiate it, depending on which line the vehicle is travelling and the direction. The *through* and *diverging* routes, identified in Figure 2.3 are the main and diverging lines of the turnout. When the vehicle runs from the crossing nose to the switch toe, it is called *trailing*, while in the opposite direction it is called *facing*.

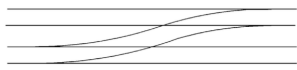
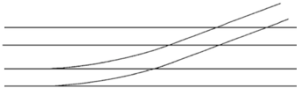
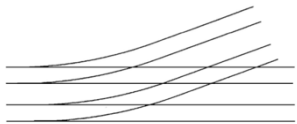
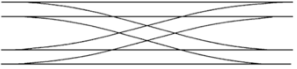
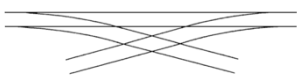

Many layouts of S&Cs can be found and, according to the European standards [15], the following turnout layouts are designated as presented in Table 2.1. The abbreviations in brackets in Table 2.1 are used to classify an S&C, in addition to the rail type.

Table 2.1. S&C layout designation [15]

Description	Scheme
<p><u>Diverging turnout</u>: the stock rails of the main line are bent either to the right (RH) or to the left (LH)</p>	
<p><u>Equal split or symmetrical turnout (S)</u>: two tracks diverge symmetrically from the common track</p>	
<p><u>Tanden or three-throw turnout</u>: formed by the junction between two tracks and a common track. The following types are titled:</p>	
<ul style="list-style-type: none"> • <u>Symmetrical (S3)</u>: two tracks diverge symmetrically from a common central track. 	
<ul style="list-style-type: none"> • <u>Non-symmetrical to the same side</u>: two tracks diverge from a common main line either to the left (LL) or to the right (RR). 	
<ul style="list-style-type: none"> • <u>Non-symmetrical to opposite sides (LR)</u>: two tracks diverge from a common main line, one to the left and the other to the right. 	


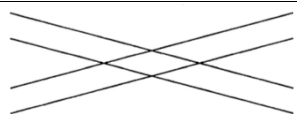
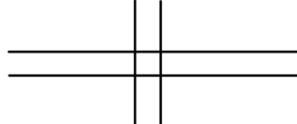
The combination of two or more turnouts is also described in the European Standards [15], where the most common are shown in Table 2.2.

Table 2.2. Turnout combinations [15]

Description	Scheme
<u>Single crossover</u> : Two turnouts placed heel to heel connecting two twin tracks	
<u>Single junction</u> : one track intersects two adjacent tracks which can partially or completely connect them all	
<u>Double junction</u> : two tracks diverge from a double track main line	
<u>Scissors crossover</u> : formed by two intersecting crossovers	
<u>Half-scissors crossover</u> : two opposite turnouts on the same track, facing each other	
<u>Interlaced turnouts</u> : two turnouts laid opposite one another and mutually interlaced. They can be of opposite hands or the same hand	

Depending on the S&C layout, it may end up with the three types of crossing classifications shown in Table 2.3 [15].

Table 2.3. Crossing classification

Description	Scheme
<u>Acute crossing</u> : it ensures the possibility of changing routes	
<u>Diamond crossing (or obtuse crossing)</u> : it allows the continuity of two routes	
<u>Square crossing</u> : two tracks of different gauges cross each other at square angles	

Depending on the way the crossing is machined, they can be defined as:

- Cast centre block: the nose and the throat are made as one block, the leg ends are welded and the wing rails are attached with tension controlled bolts;
- Monobloc: all the components up to the joints to plain line are assembled as one piece;
- Semi-fabricated: the cast-nose piece is welded to manganese steel rail legs and the wing rails are attached with tension controlled bolts.

Depending on how the crossing is mounted and connected to the remaining track, the crossings are classified as [18]:

- Welded: the leg ends terminate with pearlitic rails so that they can be welded to the track with standard techniques;
- Bolted: the leg ends are attached to the track through fish-plated connections.

In short, S&Cs are considerably complex parts of the railway track with discontinuities on the rail and rapidly changes on the contacting areas. The design of S&Cs is performed to minimize the wheel-rail contact forces and damage on the contacting surfaces. The rail is designed to reduce the wheel load transfer moving from one rail to another. All the elements present on this area of the track confer a non-homogeneous support to the vehicle.

2.2.1 Switch panel

Figure 2.4 shows the switch panel of a diverging turnout to the right, where the switch rails and switching machines are visible. If the train is travelling on the through route, the switch blade will be attached to the stock rail on the right, as shown in Figure 2.4, otherwise the switch blade would touch the left rail allowing the train to change line. The switch blade cross-section widens along the way to replace the diverging stock rail, in the direction from the switch toe to the crossing panel. Although the switch blade can resist the lateral forces resulting from wheel guidance, it cannot do the same for the vertical load of the wheel until there is sufficient thickness. That is why the switch toe is lowered relative to the stock rail, making the load transition from the stock to the switch rail less abrupt. This assures the rail head is thick enough to receive the full vertical load from that wheel before it makes contact with the wheel tread.



Figure 2.4 – Overview of switch panel including the switch rails and switching machines.

Figure 2.5 shows different contact conditions along the switch panel, during the load transition occurring from the stock rail to the switch rail. Section (I) represents the wheel on top of the stock rail, section (II) the location of the switch toe, section (III) shows some flange contact on the switch blade and sections (IV) to (VI) show the transition of the normal contact force from the stock rail to the switch rail. These different wheel-rail contact conditions and support stiffness along the switch as well as the crossing panel lead to severe impact loads, producing local damage on the contacting surfaces, transmission of noise, and vibrations to the environment.

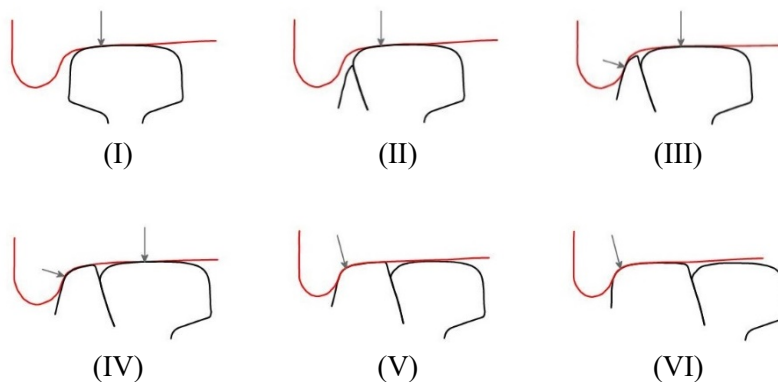


Figure 2.5 – Schematic contact conditions during a switch transition in the diverging route (adapted from [16])

2.2.2 Crossing panel

The railway crossing is the track element that allows the intersection of two different rail and wheel paths. Figure 2.6 shows a front view of a cast monoblock crossing. The rail needs to be discontinuous to allow the flanges of the wheels to pass through. On the crossing panel, two main parts can be found: the check rails and the crossing nose. The check rails are the two side rails (see Figure 2.3) that guarantees that at least one wheel of the wheelset does not lose contact when the other wheel is moving between the crossing nose and the wing rail.



Figure 2.6 – Overview of the crossing panel with a cast monoblock crossing.

The crossing nose is the physical point where the two (or more) trajectories converge. In the horizontal plane, it is characterised by the angle ϕ from the V-shape formed between the rails gauge faces as shown in Figure 2.7 and usually described as 1 in N (or $1:N$). The British Railways uses the Central Line Method (C.L.M.) to calculate the crossing angle, where the crossing rate of inclination N is defined as half the cotangent of half the angle [17].

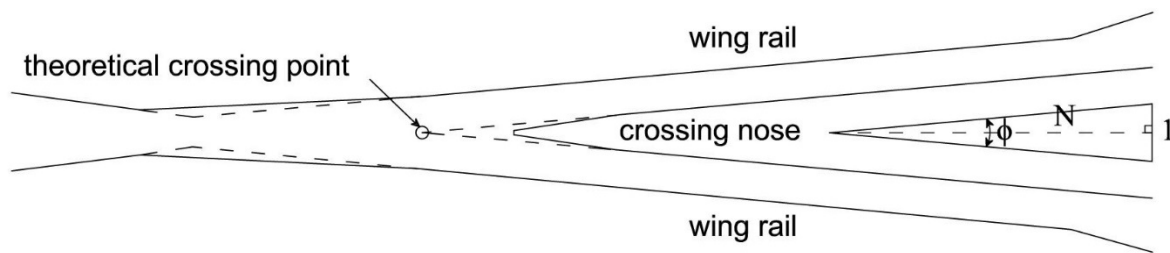


Figure 2.7 – Schematic top view of a crossing (adapted from [18])

The wheel-rail contact conditions vary significantly when negotiating the crossing. Figure 2.8 shows the contact conditions at some positions along the crossing panel, when a wheel passes over the crossing in the facing direction, coming from the switch panel. Section (I) and (II) show two consecutive instants where the wheel is contacting the wing rail. In this case, a single contact is generally observed, which moves towards the field side of the wheel profile, due to the outward deviation of the wing rail. Therefore, the rolling radius decreases and the wheel moves downwards unless the wing rail is elevated. The lateral motion of the wheelset is restrained by the check rail that prevents wheel flange contact with the crossing nose [19].

Section (III) and (IV) show two consecutive instants where the contact between the wheel and the crossing nose occurs. The contact load is rapidly transferred from the wing rail to the crossing nose. During the load transition, two contacts are observed which have a different rolling radius and therefore high creepages are observed at the crossing nose, which leads to wear. In addition, this transition leads to a significant impact force on the crossing nose due to the reversion of the vertical wheel trajectory [19]. The impact forces in this area can be two or three times the load in normal running rail and up to eight times in the crossing nose as shown in the deliverable 3.12 and 3.13 of the European project CAPACITY4RAIL [20, 21]. The smoother these transitions are, the lower the dynamic amplification of the contact forces.

Sections (V) and (VI) show two consecutive instants where the wheel leaves the wing rail, travelling only over the nose rail and on to the through rail.

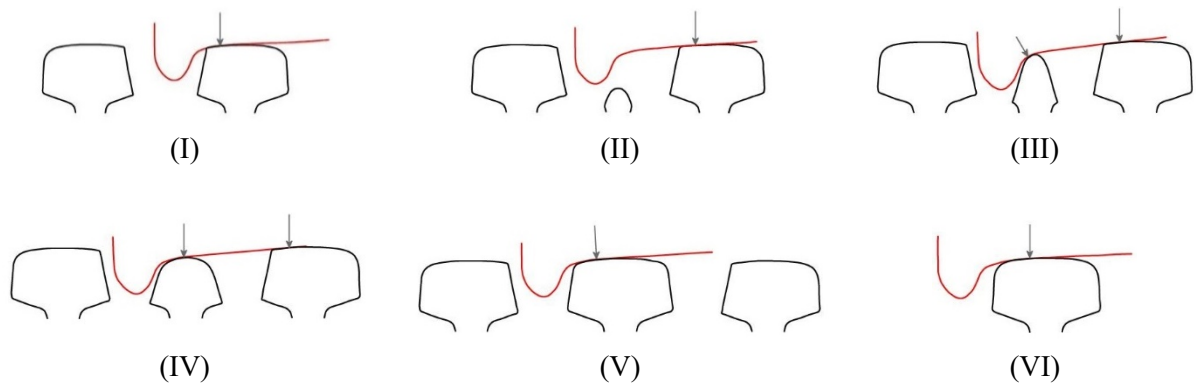


Figure 2.8 – Schematic contact conditions along the crossing (adapted from [18])

2.2.3 Degradation methods at S&Cs

The dynamic effects from trains running over the S&C lead to the degradation of the vehicle and track components and noise emission. Typical degradation methods seen at current S&C in ballasted railway track are:

- **Ballast settlement**: a permanent deformation in the ballast and underlying soil that can create gaps below bearers or, when spread to a considerable area, can affect the track geometry level. This problem results from the repeated traffic loads and can be aggravated where the wheel load transfers from one rail to another;
- **Degradation of bearer connection**: the mechanical component that connects two bearers, which represent a long bearer often found at the crossing panel, are subject to high reaction forces that lead to its degradation and possible failure. There are different designs for the connection between bearers and their choice may affect the behaviour of the long bearer leading to damage on the connection itself or the ballast underneath;
- **Rolling contact fatigue (RCF)**: the most common RCF defects are cracks on rail surface, squats, shelling and rail break, which results from the higher pressure that occurs in the subsurface of the rail;
- **Wear**: loss or displacement of material from the contact surfaces due to the creep forces occurring between the rail and wheel surfaces.

In this work, the numerical models are developed to investigate the degradation mechanisms on S&Cs and associated with the ballast condition and the degradation of bearer

connections. Some work found on the literature about RCF and Wear on S&Cs can be found in Section 2.3.6.

2.3 VEHICLE-TRACK INTERACTION MODELS

A vehicle-track interaction model comprises the vehicle model, the track model and the wheel-rail contact, which represent the forces developed in the wheel-rail interaction. Modelling all these parts in detail is a challenging task from a computational point of view. The chosen approach and modelling assumptions must therefore depend on the aim of the study.

Both track and vehicle can be modelled based on two formulations: the finite element (FE) method and Multibody Systems (MBS) formulation. The FE method is a space discretization method, where the structure is divided into a finite number of continuum elements (the finite elements), for which a set of functions defining the field of displacements is assumed. Nowadays, FE commercial programs such as ANSYS, ABAQUS and Nastran have extensive libraries of elements to model flexible, rigid, and joint components, allowing the user to create complex models. The MBS formulation represents mechanical systems that comprise rigid or flexible bodies that are connected to each other by force elements, such as, springs and dampers, and kinematic joints, such as revolute and cylindrical joints, that constraint degrees of freedom [22]. These rigid bodies are defined by their mass, inertia and location of the centre of gravity and can have a maximum of six degrees of freedom (d.o.f.) (three translational and three rotational). Different software packages based on MBS, either completely dedicated to railways or with specific rail modules are available, such as VI-Rail (previously called ADAMS/Rail), SIMPACK, VAMPIRE, NUCARS or GENSYS. [23] presents a state of the art of MBS in the railway sector.

Mechanical engineers involved in vehicle design tend to use MBS software to study vehicle dynamics, taking advantage of fast wheel-rail contact models calculation and the library of elements available to model the vehicle components. Civil engineers who design railway tracks tend to use FE tools, which allow them to build complex and large models that can represent the different track layers or civil structures and calculate the strains and stresses of the track components.

2.3.1 Finite Element approach

Most earlier studies aimed to obtain simplified analytical solutions. The simplest model to represent a track was proposed by Timoshenko in 1926 and considers the rail as an elastic Euler beam supported on a spring foundation with infinite length (see Figure 2.9). [24-27] presented similar models considering a continuously supported beam. The track can also be modelled as two beams placed one on the top of the other, continuously supported, where the upper one represents the rail and the lower one the sleepers or the slab for a slab track, as presented in [7].

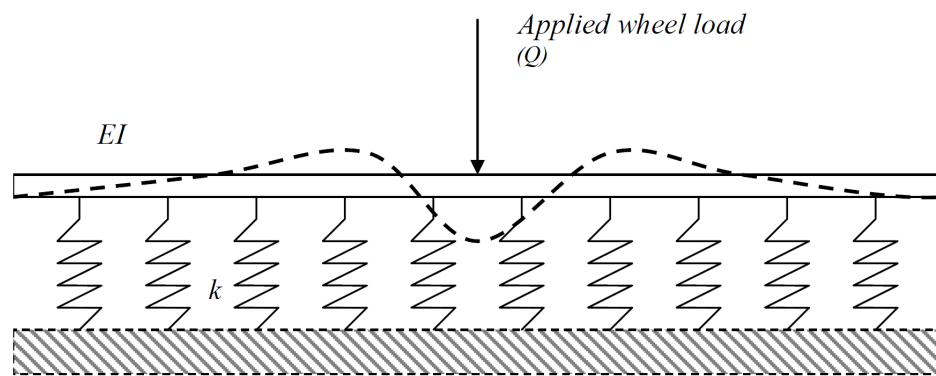


Figure 2.9 –Continuously supported beam on a spring foundation with the rail deformation represented in a dashed line [4]

Continuously supported beam models cannot simulate the whole frequency range of the ballasted track, as shown by [28]. In this work, the vertical and lateral track receptance for a typical ballasted track and the main frequencies are of interest in both directions. They concluded that to obtain the whole frequency range of interest the track should be represented with discrete supports. The simplest model considering the rail discretely supported is the model based in the Winkler foundation with discrete springs spaced by the sleeper spacing [7].

The discrete approach enables modelling more complex structures with different layers of the ballasted track. Thus, the discrete track model can include rails, rail pads, sleepers, ballast, sub-ballast and subgrade, as proposed by [29] (see Figure 2.10). Usually, the discrete track models are modelled with a FE software as it enables modelling the deformation of railway components, for instance, rails and sleepers can be modelled as beam elements [30].

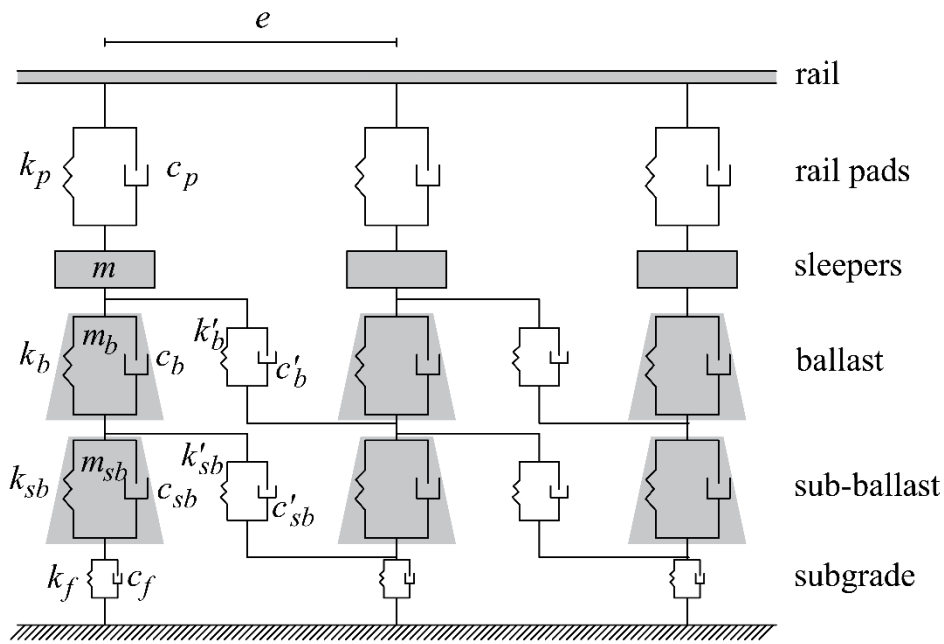


Figure 2.10 – Four layers discretely supported ballasted track (adapted from [31])

Some non-commercial FE programs to take into account the wheel-rail contact can be found in the literature, such as VSI developed by [36] and extended by [37] which account for lateral behaviour, VTI developed by [38] and DIFF that has been developed at CHARMEC [39].

Different vehicle representations have been used to study vehicle and structure dynamics. The type of model used depends on the type of analysis and the results sought. These model representations are: moving loads [32, 33]; moving unsprung masses [34] and moving vehicles where the suspension levels of the vehicle are considered [35].

2.3.2 Multibody Systems approach

Most MBS packages offer a simplistic way to model the track either considering it rigid or with a certain flexibility. A typical flexible track model adopted in many MBS software is the continuous track model, also known as co-running track model. This type of track model is suitable to study low frequency problems (below 20 Hz), such as comfort analysis and curve negotiation, as the track behaves as a very stiff component [28]. The model configuration and the number of degrees of freedom of the model can vary depending on the software used. The default continuous track model implemented in Vampire with 3 d.o.f. for the sleeper and one d.o.f. for each rail as shown in Figure 2.11 a). Another continuous track

model is shown in Figure 2.11 b), which considers three rigid bodies simulating the left and right rail and a third one comprising the mass and inertia parameters of the sleeper and the ballast. The rail masses are connected to the sleeper mass and the sleeper mass to the ground. Each body considers 3 d.o.f., two translational and one rotational.

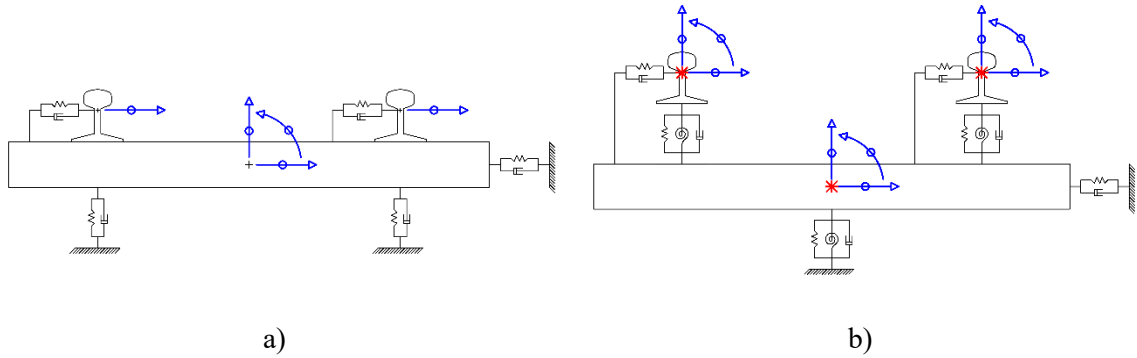


Figure 2.11 – Continuous track model implemented in: a) VAMPIRE and b) VI-Rail.

The continuous track model runs under each axle of the train with the same forward speed. It offers continued support to the train, which means that even being able to reproduce some of the track flexibility, it cannot consider discrete events such as joints or badly supported sleepers. In the case of S&Cs, this type of track model cannot simulate the variation on rail properties or account for longer bearers and the effect of two tracks connected.

[40] compared a simple rigid track model with the continuous track model, and a finite element discrete track model while evaluating their impact on wheel-rail contact forces. The FE discrete track model provides more accuracy, especially for higher frequency vibrations. Both the vehicle critical speed and the dominant frequency of the hunting motion are shown to be highly influenced by the degree of detail of the model. The obtained wheel-rail contact forces are similar for frequencies up to 20 Hz, but showed considerable differences are observed for higher frequencies, especially when the track is considered as rigid. The results obtained with the finite element and the continuous track model show relevant differences.

Some MBS packages offer the possibility to create a flexible track model with the rail discretely supported. This is achieved by implementing FE method within the MBS software. One example is presented by [4] where a FE track model is integrated into the multibody software VI-Rail. In this case, the track model comprises beam elements, available in ADAMS software, that represent the left and right rails and are supported by

sleepers distributed along the track, where bushing elements are used to connect the rails and the sleepers as well the sleepers and the ground.

2.3.3 Coupling FE and MBS

To overcome some of the limitations in FE and MBS software, different approaches were taken. The first one is known as co-simulation and consists of the two packages running simultaneously and changing information between the two as it has been proposed in [41, 42], where the vehicle is modelled with MBS approach and the flexible track modelled with FE method.

Alternatively, dynamic analyses with the MBS software are performed to obtain the forces transmitted to the track and using them as input for a track model created with FE software. Examples of this approach are presented in [2, 42-44]. This type of approach is commonly used when studying stresses on the track components.

A different approach is importing FE data to MBS software as proposed by [45] who created a flexible track model implemented in SIMPACK using the modal superposition method. Elastic bodies (FLEXBODY) were used and represented by a number of natural modes obtained from NASTRAN. A generalized dynamic reduction implemented in NASTRAN was used to reduce the size of mass and stiffness matrices as well the eigenvectors that are imported to the MBS model.

Another example is the one presented in [46], where a discrete and flexible track model built in VI-Rail is proposed. The rail information is imported from NASTRAN using a modal decomposition method. The remaining track is built based on multibody systems with rigid rail elements on top of the sleepers and rigid sleepers. One example of this technique applied to S&Cs is presented in [47]. Rails and sleepers are modelled using beam elements in commercial FE-code ABAQUS and converted into flexible bodies in SIMPACK format using the Craig-Bampton substructuring method. The rail-pads and ballast stiffness are modelled inside SIMPACK using discrete Kelvin bushing elements.

2.3.4 The wheel-rail contact problem

The contact between two bodies can be conforming or non-conforming [48]. If the two bodies have a similar shape and their surfaces fit closely without deformation, the contact is

conforming, otherwise, it is non-conforming. In railways, the wheel and rail profiles are dissimilar and it is usual to consider a non-conforming contact between them [49]. The wheel and rail profiles can contact at a single point, multiple points or along a line [50]. The contact conditions are affected by the degradation of the wheel and rail profiles.

Wheel-rail contact models are developed to predict the normal pressure and tangential distribution across the contact patch. Usually, there are two main approach categories to solve the normal problem, the Hertzian and non-Hertzian contact. The Hertzian contact is based on the contact of two cylinders that leads to an elliptical contact patch. The non-Hertzian contact is based on more realistic contact patch shapes, where the penetration function is used to predict the contact patch [51-53]. For the tangential problem, the main contribution was made by [54], leading to the computer code CONTACT, based on the ‘exact’ theory but slow to implement and FASTSIM, a ‘simplified’ method, faster and most widely used.

The contact routine implemented in VI-Rail, which was used for this thesis, is based on FASTSIM with some modifications concerning the meshing of the contact surface to improve stability at high spin and at the same time decrease calculation time [4]. The normal contact problem is a non-Hertzian contact model. VI-Rail also calculates up to eight points of contact but only outputs three.

2.3.5 Switches & crossing studies

In this section, a brief overview is given to studies related to S&Cs, which includes: the evaluation of the wheel-turnout contact forces, damage in S&Cs, new sections or designs, the track support influence and site measurements done in S&C.

The interaction between the vehicle and the turnout, which occurs through the wheel-rail interaction, is typically characterized by high transient forces due to the wheel load transfer from one rail to another. The wheel-rail contact models should be accurate enough to predict the contact forces and analyse the dynamic response of the turnout components. Thus, numerical simulations of the vehicle negotiating a turnout are important for better designs of turnouts and vehicles. Many parameters may influence the train-turnout interaction, where the geometry and material properties of the wheel, the switch and the crossing play a crucial role [16].

Early studies on the numerical simulation of a train passing through a turnout were mainly focused on the wheel-rail kinematics and the different contact conditions (rail profiles). One of the first to deal with this topic was [55]. They considered the geometry of the turnout and the contact between the flange and the check rail, but they neglected the gap on the crossing nose. The lateral forces of the leading wheelset were used to validate a vehicle-turnout numerical model using ANSYS-DYNA commercial software. Most of the works available in the literature focused on the vehicle motions and ride safety due to the turnout geometry [56, 57]. The turnout flexibility was neglected or simulated by simplified models [58].

Impact loads often observed when the vehicle travels through a switch and a crossing. [59] investigated the wheel-rail impact forces due to a wheel or bogie passing over a railway crossing. Here, a full turnout model in the Finite Element software I-DEAS was used, and the high-frequency of train-turnout interaction has been studied with the software DIFF. The superposition method is used to build the turnout model, with modes of the track up to 1500 Hz and the Hertzian contact spring is used to obtain the wheel-rail interface. The authors concluded that two parameters strongly influence the dynamic impact load, which are the vehicle speed and variation on the rail profiles from the wing rail to the crossing nose. Although this study considers the rail geometry and the turnout flexibility, the simulation only captured the vertical dynamics and therefore only the through route was considered.

The work from [60, 61] proved that high impact loads may arise on the crossing, leading to damage, fracture or wear on both the crossing and the wheels. [61] compared four different methods to model the wheel-rail rolling contact forces, namely, the Hertz method, the Kalker rolling contact theory, with the software CONTACT, the elastic FE model and elastic-plastic FE model. [3, 62] considered the turnout flexibility with spatial variation of track stiffness and inertia properties for the train-turnout interaction. [3] compared simulations using GENSYS and DIFF3D (a MBS and FE software) considering the track as rigid. [62] studied the plastic deformation of a switch rail on GENSYS, considering the train switching into the turnout in facing direction. The turnout deformability was based on a co-following mass-spring-damper system with a few degrees of freedom, coupled to each wheelset and running at the same velocity (co-running track model).

More recently, some authors have been showing that the supporting stiffness influences significantly the train-turnout interaction and should not be neglected [63]. The vertical support stiffness changes longitudinally along the switch and crossing panels due to

variations on the sleeper support as well the rail geometry. The variation of the track support stiffness along the turnout was not considered in previous works found in the literature. [64] proposed a methodology to optimize the support stiffness of a switch, varying the rail pad properties and applying USPs. The track model considered was the co-running track model of the SIMPACK software and the track model parameters were varied along the turnout, namely, the inertia properties and spring-dampers. Nevertheless, dynamic effects that are obtained typically with the track discretely supported, such as, the sleeper passage, are not captured.

[63] analysed the influence of the stiffness and damping of the rail pads, and the sleeper weight, on the vertical dynamic forces that occur on the crossing component. USPs were also considered to help reducing the impact loads. The model was built in DARTS_NL that enabled capturing the vertical and longitudinal dynamics.

[65] compared two different fastening types, direct and indirect, in terms of equivalent stiffness variation and track frequency response and where USPs were also included in the numerical models. The track model was built in MATLAB and considers the track discretely supported including the rail pad and support layers. The rail was modelled by Timoshenko beams with four elements per sleeper-spacing and the wheel-rail contact algorithm is based on Hertzian theory and Kalker linear creep law. The sleeper flexibility was neglected. Only the vertical behaviour is analysed and the crossing is implemented as a vertical irregularity with the wheel trajectory, instead of using the exact rail profiles.

[66] proposed a finite element model of a high-speed railway turnout to analyse the distribution of track stiffness. Different types of rails, shared iron base plates, sleepers of different lengths and spacer blocks were considered. The dynamic response of the train passing the turnout is calculated by the commercial software SIMPACK without considering the variations in track stiffness. Those forces are then applied to the complete FE model to optimise the pad stiffness under shared iron base plates.

2.3.6 Complementary literature on S&C

The following studies are not exactly the focus of this work and represent other areas of study in the thematic S&C.

The design of the crossing component geometry aims to minimize the impact force due to the load from the wing rail to the crossing nose. An important design constraint is that the crossing nose is robust enough from the structural point of view where the wheel contact first occurs. In addition, the wing rail should enable the wheel to contact with the crossing nose in such a way that the transient forces during the wheel transfer are low. It has been demonstrated that slight changes in the geometry could lead to great improvements, reducing the degradation of both wheel and crossing [19, 67].

Since the process of a train running on the switch panel is a transition event, the rolling radius may vary through the switch due to its design. [68] developed an optimisation process of the switch rail profile geometry, using objective functions based on the contact pressure and energy dissipation in the wheel-rail contact. The solutions obtained lead to small variations in design and preference was given to increase profile height and shoulder. These changes make the contact load to be transferred earlier with increased vertical loading at a thinner rail cross-section.

The track gauge in turnouts has been also studied in optimisation studies that aimed at reducing the wear of the flange and switch rails. In other words, these studies proposed solutions to minimize the flange contact with the switch rail during the wheel transition from stock rail to switch rail. Some examples are [69-71].

Wear, accumulated plastic deformation and rolling contact fatigue are common damage mechanisms in switches and crossings [72]. The key to understand and predict wear and rolling contact fatigue problems is based on stress and strain analyses. Simulation methodologies to predict rail profile degradation due to plastic deformation and wear are presented in [2, 64, 73]. [74] studied the traffic parameters that should be considered, for example, for damage on the switch rail when the train travels the divergent route. The parameters were axle load, wheel-rail friction coefficient and wheel and rail profiles. [75] investigated the cyclic deformation of a crossing nose during several passages for two different materials. The material properties of the switch and crossing play an important role in the amount of wear and rolling contact fatigue of the wheel and rail. For example, [76] studied three different materials for the crossing nose using a multi-scale FE model and compared the crack development and growth on all of them.

Field measurements are important to build and calibrate the S&C numerical models. They allow to better predict the contact forces and consequently the damage that a S&C is

subjected to. [77], for example, used a laser-based device called Calipri to measure the geometry of a crossing that was further used in a 3D Finite Element model to simulate the dynamic response of a wheelset passing over the crossing. Using a measurement device and two sensors on the crossing nose and on the rail respectively, the magnitude and location of the maximum accelerations for each passing wheel was determined.

[78] quantify experimentally the high-frequency content in the wheel-rail contact forces in S&C. The authors used an instrumented wheelset and low-pass filtered with different cut-off frequencies. A considerable contribution of the high frequency content has been found to the maximum vertical contact force on the crossing but not so significant for the maximum lateral contact force in the switch panel.

[58] compared two alternative approaches to simulate the train-turnout interaction and calibrated them with site measurements. One of the approaches is based on a multi-body model of the vehicle, a detailed model of the contact, and a finite element model of the turnout using beam elements and the second approach is a detailed 3D Finite element model of the turnout taking into account the soil-foundation interaction but with simplified contact model. Three turnout layouts were considered. On the track were registered vertical and lateral accelerations in the centre of the crossing panel as well vertical and lateral track inertances. On the train were measured vertical axle box, bogie frame and car body accelerations. Both numerical models have shown a good agreement with the measurements.

2.3.7 Summary

The majority of the work found in the literature lacks in considering the track support stiffness variability and the rail discretely supported using MBS software. Some authors consider the track support variability but use software created in-house, usually based on finite element methods, and do not have reliable wheel-rail contact routines like commercial MBS software. The model should include all the rails on both switch and crossing panels, the correct positioning and length of the bearers and their connection when existent and a variation of the trackbed stiffness along the S&C. Therefore, the main novelty sought in this work is the development of a full detailed model of a S&C with all the complexities above mentioned that are relevant to assess its performance and condition.

Several areas of work about S&C have been identified in the literature throughout this chapter. This work will focus only on the non-homogeneous stiffness along the turnout and

degradation methods observed in S&Cs, namely voided bearers and faulty connections between bearers.

3 DEVELOPMENT OF FLEXIBLE TRACK MODELS USING MULTIBODY FORMULATION

In this chapter, four track models are presented and compared to understand their advantages and choose the most suitable to build a full railway crossover. As mentioned in the previous chapter, Multibody Systems (MBS) software always had their focus on the vehicle with simpler track models, but they also have quite robust wheel-rail contact algorithms for vehicle-track interaction simulations and a library of validated railway vehicles available. For these reasons, the MBS environment has been chosen over the FE environment. It was also showed that a gap exists in the literature for track models built within MBS software that considers the stiffness variation on the support and the rail discretely supported and with variable properties. To select the best model to build a complex S&C layout, the models available in the literature need to be compared.

Within MBS software, three types of flexible track models were identified in section 2.3.2, the continuous supported track model and two discretely supported track models, one built entirely inside the MBS software and the second one using an external FE software to get modal information from the track. These three track models are compared with a bidimensional vehicle-track model built *in-house* on MATLAB. The main objective of this work is to model a full railway S&C and study the behaviour of its components, so it is important to select a track model capable to give information about the different elements of the track. A benchmark study that considers simulations of a wheelset and a vehicle negotiating a plain line track under the excitation given by a vertical track irregularity is used here to compare the different track models. Wheel-rail contact forces, sleeper displacements and rail motion are compared between all models and the best model to represent S&Cs is selected for the rest of the thesis.

3.1 TRACK MODELS DESCRIPTION

3.1.1 Model a: Continuous supported track model

The continuous track model comprises one lumped parameter model independently built per each axle of the vehicle, as shown in Figure 3.1. This track model can show different

configurations, depending on the MBS software. In VI-Rail, the track lumped parameter model consists of a rigid body element for each rail and other body element incorporating the sleeper and part of the ballast mass. All three rigid bodies are designated in VI-Rail as “parts” and have three Degrees of Freedom (DOF), which are the vertical, transversal, and roll motions, as shown in Figure 3.1. The base part is connected to the rails and to the ground through bushing elements with linear stiffness and damping in the three active directions. Note that a bushing element is a force element with stiffness and damping that resists all DOFs. Each independent track model runs underneath each axle of the vehicle at the same forward speed [4].

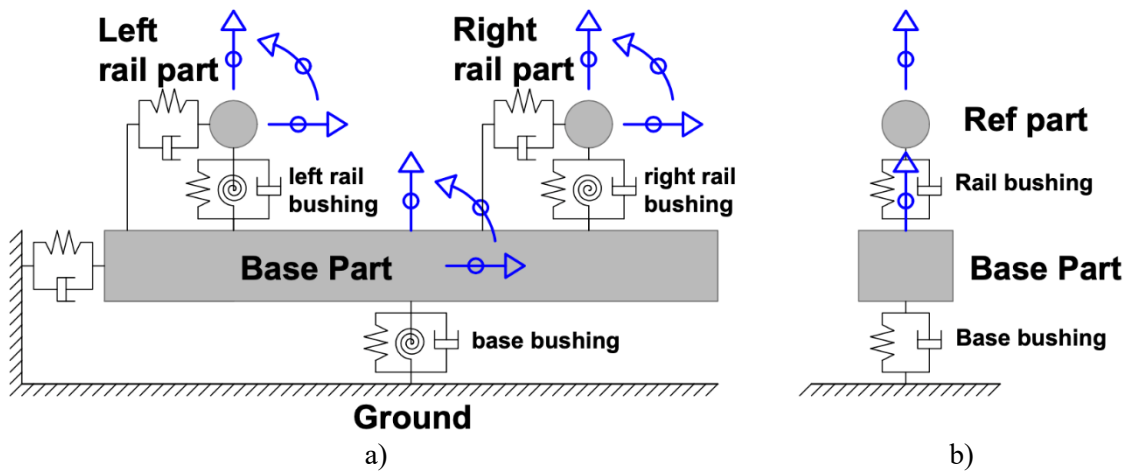


Figure 3.1. Cross-section of the continuous track model used in VI-Rail: a) front view; b) side view (adapted from [4]).

The continuous track model available in VI-Rail benefits from a simple formulation that enables faster simulations. In turn, the model has the following limitations:

- Inability to directly model non-linearities along the track or discrete events, such as missing or faulty pads, unsupported sleepers or variable rail properties along the track. Therefore, the model parameters are usually made constant along the track.
- The influence between axles through the track is not captured as each axle is supported by its own lumped parameter model independently reacting from one another.

Other software like SIMPACK allows changing the layout of the continuous track model, letting the user add or remove more elements. In the case of VI-Rail, it requires a deeper

understanding of VI-Rail and Adams language and the macros with the code to build the track model had to be changed.

[79] presented 2 DOF equivalent track model, which assumes the track symmetric along the longitudinal axis. It corresponds to a mass-spring system able to represent half of the track (one rail and half sleeper) and represent track frequencies up to 1 kHz. This model is very similar to the continuous track model which does not consider the bending properties of the rail or the discrete nature of the support (sleeper spacing). To consider the rail bending properties, the authors proposed a scale factor to affect the track parameter, in order to match the low frequency of the 2 DOF track model with the static track stiffness from the analytical solution, i.e. a beam on elastic foundation. The static stiffness K_{st} of a single layer continuously supported track, when a force is locally applied, is given by [80]:

$$K_{st} = 2\sqrt{2}(EI_r)^{1/4}k_s^{3/4} \quad (3.1)$$

where E and I_r refer to the Young modulus and second moment of area of the rail beam, respectively, and k_s represents the stiffness per unit of length of a two-layer continuous track support, given by [79]:

$$k_s = \frac{k_p k_b}{k_p + k_b} \quad (3.2)$$

where k_p and k_b represent the rail-pad and ballast stiffness, respectively. The equivalent track length that contributes to the response of the beam due to a point load is obtained by [79]:

$$L_{eq} = \frac{K_{st}}{k_s} \quad (3.3)$$

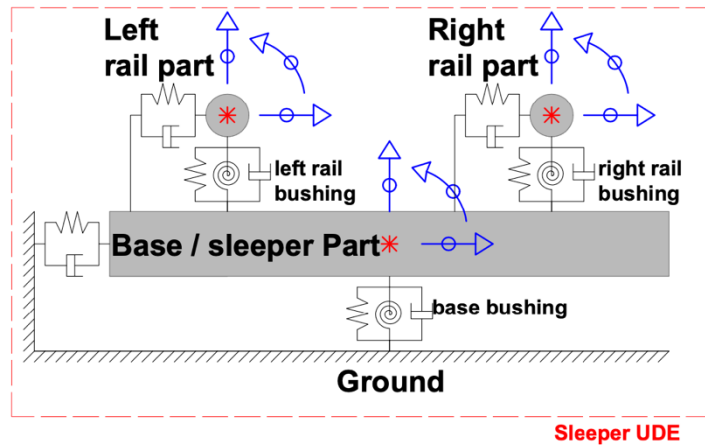
Mass and stiffness values per unit length of track can be affected by L_{eq} to get discrete mass and stiffness values. [79] shows that using these corrected track parameters gives a good approximation of this model up to 1 kHz compared with the beam on elastic foundation, with the resonances and anti-resonances frequencies well preserved under that interval.

3.1.2 Model b: Discretely supported track model - beam element

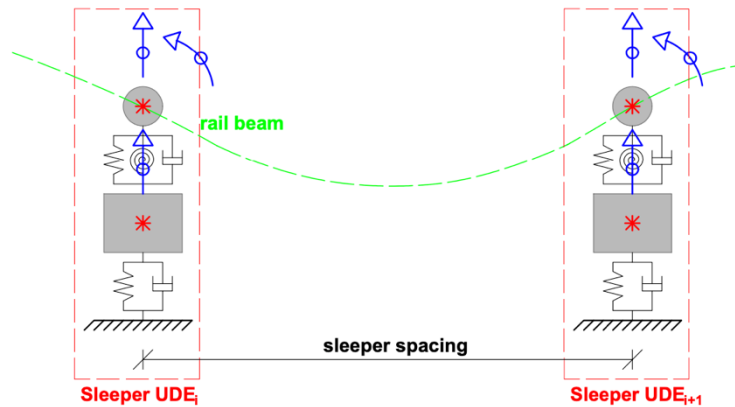
Two discrete track models using MBS approach were discussed in section 2.3.2, where the first one is entirely built inside MBS software. VI-Rail allows building a discretely supported track model automatically, using the same track parameters and sharing the same structure as the continuous track model, presented in Figure 3.1 [4]. The two rails and base parts and all bushings connecting the rail to the sleeper and the sleeper to the ground are grouped in elements called sleeper User Defined Elements (UDE) as shown in Figure 3.2 a). UDE are essentially macros built by the user to build repetitive parts of the model, avoiding creating every single element individually. The track model comprises as many Sleeper UDE as the user specifies and they are equally spaced and positioned according to the track layout.

The rail bodies are connected by beam elements available in ADAMS, as shown in Figure 3.2 b). The ADAMS beam element is a three linear translational and three rotational force element between two locations, which has no mass and transfers from one point to the other axial forces, bending moments about the vertical and lateral axis, torsional moments about the longitudinal axis and shear forces. Linear Timoshenko beam theory is used to define the forces and moments.

Both rails and sleeper parts have three DOFs by default, vertical and lateral translations and roll rotation, whereas the pitch and yaw rotation of the rails can be turned on or off. VI-Rail Flextrack plugin is required to build this type of model.



a)



b)

Figure 3.2. Sleeper UDE: a) front view; b) side view (adapted from [4]).

Although the VI-Rail Flextrack tool builds discretely supported track models automatically, using the same inputs required to build the continuous track model, this automated model generation leads to the following limitations:

- Sleeper spacing is kept constant through the entire track length, which might not be exact to model an existing turnout;
- Each sleeper UDE has the same configuration and constant parameters;
- Only one single track is generated.

Since the purpose of this thesis is to study S&Cs, the discretely supported track is built manually using ADAMS and VI-Rail programming language, which allows building a complex model with more than one track. A more detailed explanation of the steps required to build this type of model is presented in chapter 4.

In this chapter, a plain line track model similar to the model shown in Figure 3.2 is used as an example to compare the different type of models. The model is composed of the same two rigid bodies representing rail mass and inertia for the section of rail above each sleeper and one rigid body representing the sleeper mass and inertia. The same two bushing elements with linear properties are used to model the rail-pads, but now with two bushings instead of only one to represent the trackbed support below the two rails. The rails have all the 6 DOFs, i.e. the longitudinal translation is also allowed compared to Figure 3.2, and the flexible part of the track has two rails to connect to the rigid parts at each extreme. The sleepers have 3 DOFs, which are the vertical and lateral translations and roll motion.

As mentioned above, the rails are decomposed into discrete rigid bodies with mass concentrated above the sleepers and connected by Timoshenko beams elements [81]. This means that the mass of the rail is not distributed along the beam. The beam element creates forces and torques for all 6 DOFs of the two consecutive rigid bodies, as shown in Figure 3.3. The beam is connected through markers created on the centre of mass of each body, namely marker j and marker i . Markers can store both position and orientation of any part of the model and can be used to apply forces or constraints or get kinematic positions, velocities, or accelerations. Both rail parts, forces and torques generated from the beam element are illustrated in Figure 3.3.

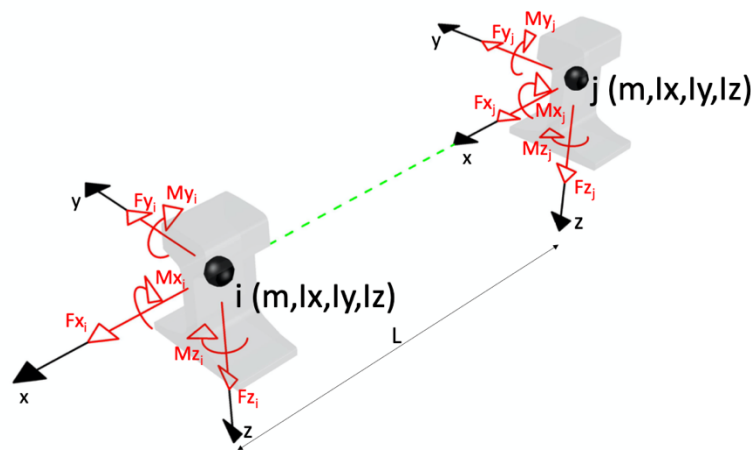


Figure 3.3. ADAMS beam element used to connect two rigid bodies.

The vector $\{F\}$ containing the forces and moments is calculated at marker i by:

$$\{F\} = [K] \cdot \{u\} - [C] \cdot \{\dot{u}\} \quad (3.4)$$

where $\{u\}$ and $\{\dot{u}\}$ contain respectively the displacements/angles and translational/angular velocities of marker i relative to marker j . The damping matrix $[C]$ is obtained as function of the damping factor η as:

$$[C] = [K] \cdot \eta \quad (3.5)$$

where $[K]$ is the stiffness matrix given by [4]:

$$[K] = \begin{bmatrix} \frac{EA}{L} & 0 & 0 & 0 & 0 & 0 \\ 0 & \frac{12EI_z}{L^3(1+P_y)} & 0 & 0 & 0 & \frac{-6EI_z}{L^2(1+P_y)} \\ 0 & 0 & \frac{12EI_y}{L^3(1+P_z)} & 0 & \frac{6EI_y}{L^2(1+P_z)} & 0 \\ 0 & 0 & 0 & \frac{GI_x}{L} & 0 & 0 \\ 0 & 0 & \frac{6EI_y}{L^2(1+P_z)} & 0 & \frac{(4+P_z)EI_y}{L(1+P_z)} & 0 \\ 0 & \frac{-6EI_z}{L^2(1+P_y)} & 0 & 0 & 0 & \frac{(4+P_y)EI_z}{L(1+P_y)} \end{bmatrix} \quad (3.6)$$

where:

$$P_y = \frac{12EI_z \cdot k_y}{GAL^2} \quad (3.7)$$

$$P_z = \frac{12EI_y \cdot k_z}{GAL^2} \quad (3.8)$$

in which k_y and k_z define the shear area ratio for shear deflection in the lateral and vertical directions, respectively.

The wheel-rail contact algorithm determines forces transmitted in the wheel-rail interaction. The contact forces are applied on the track model through the rail rigid bodies. GFORCE elements are created at every rail mass to receive these forces. GFORCE element stands for ‘‘General Force’’ and allows defining forces and torques in all directions for the two markers i and j . These elements have no properties assigned and are used only in the internal sub-routine for the contact in VI-Rail.

The deformed shape of the rail at any position of the beam is obtained using a shape function that relates the position and angle of the two rail parts. The deformed shape of the rail is used to update the track curvature during the simulation. Once all the rail markers assume the deformed equilibrium position, a spline equation is recalculated to fit through all markers. Figure 3.4 shows a diagram explaining the terms that will be used in shape functions.

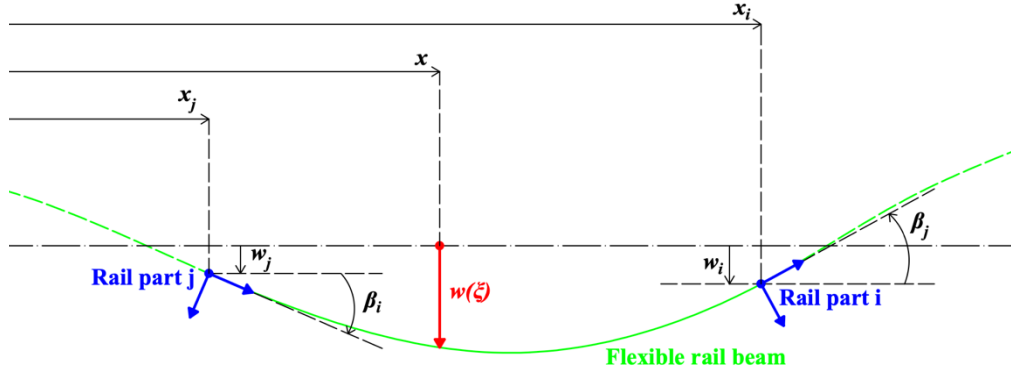


Figure 3.4. Deformed rail beam calculation (adapted from [4]).

As shown in Figure 3.4, x is a point of the rail element between points x_j and x_i that identifies the two adjacent rail masses. The displacements of the adjacent rails are w_j and w_i , whereas the rotations are β_j and β_i . Through the shape functions, the displacement $w(\xi)$ of the point x is obtained as:

$$w(\xi) = \begin{bmatrix} 1 - \xi^2(3 - 2\xi) \\ \xi^2(3 - 2\xi) \end{bmatrix} w_j + \begin{bmatrix} (x_i - x_j)\xi(1 - 2\xi + \xi^2) \\ (x_i - x_j)\xi(-\xi + \xi^2) \end{bmatrix} \begin{bmatrix} \beta_j \\ \beta_i \end{bmatrix} + w_i \quad (3.9)$$

where:

$$\xi = \frac{x - x_j}{x_i - x_j} \quad (3.10)$$

so that $0 \leq \xi \leq 1$

The forces and torques obtained with the wheel-rail contact model are distributed between the two adjacent rail parts. Shape functions are used to calculate the proportions to be applied in each rail part. Considering again the rail parts j and i as two parts connected by a beam, F_j and F_i are the forces applied in each part respectively and $T_{x(j)}$ and $T_{x(i)}$ the torques associated with rail roll. P is the total force, which has to be equal to the force coming from the contact routine. The moment about the longitudinal axis, M_x is obtained from the distance

between the top head of the rail and the centre of mass where the beam is applied and the distance from the centre of mass and the rail foot where the bushing for the rail-pad is connected. The values of force and torque to apply in each rail part is presented in Equation 3.11. Figure 3.5 has a representation of the force and torque distribution as function of the location in between parts j and i .

$$\begin{cases} F_j = [1 - \xi^2(3 - 2\xi)]P \\ F_i = [\xi^2(3 - 2\xi)]P \\ T_{x(j)} = [1 - \xi^2(3 - 2\xi)]M_x \\ T_{x(i)} = [\xi^2(3 - 2\xi)]M_x \end{cases} \quad (3.11)$$

where $\xi = \frac{x-x_j}{x_i-x_j}$, so that $0 \leq \xi \leq 1$

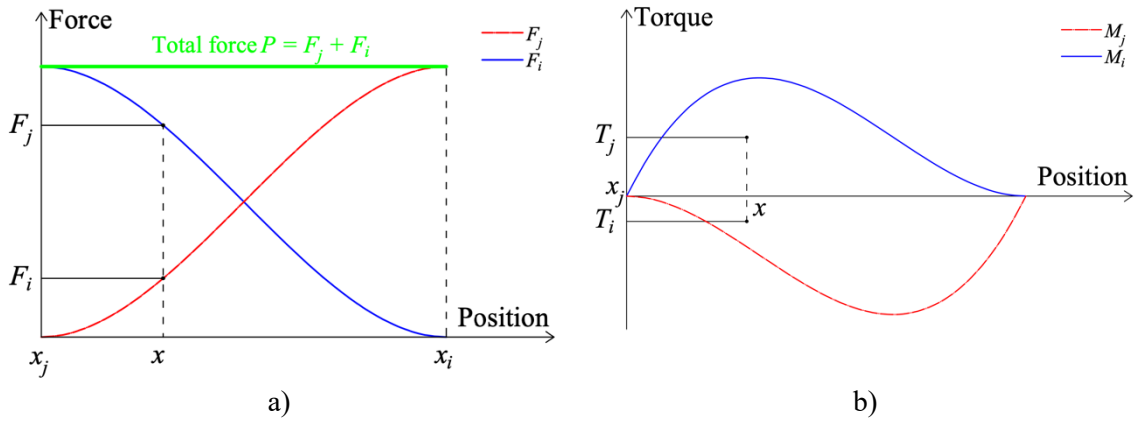


Figure 3.5. Shape functions to: a) force distribution; b) torque distribution.

3.1.3 Model c: Discretely supported track model - modal decomposition method

An alternative discrete track model can be built based on the modal information of the rails, that is, the natural frequencies and mode shapes which can be obtained with a Finite Element software. The remaining track is identical to the previous track model that uses ADAMS beams (see Figure 3.2). The track model is then defined in VI-Rail with a Modal Neutral File (MNF). Here, ANSYS is used to model the rails, where more than one element per sleeper spacing and variable rail cross-section can be considered, which is an advantage when compared with the ADAMS beam that assumes only one beam element with constant properties between two rail parts.

In ANSYS, the following points have to be considered in order to export the modal information to ADAMS [82]:

6. Build the finite element model in Mechanical APDL that will be exported to ADAMS. Only linear behaviour is allowed and damping is ignored when the modal analysis is performed and the MNF is generated. ADAMS program requires a lumped mass approach which may lead to inertia errors if a refined mesh size is not used in ANSYS model. To confirm if the mesh size is acceptable, performing the modal analysis with and without the command LUMPM,ON and compare the frequencies.
7. Attention is given to the interface points that are used in ADAMS to connect to the remaining structure. These points are also the only points of the structure where can be applied forces in ADAMS. In ANSYS, these points correspond to nodes of the model that must have six degrees of freedom, i.e. no constraints can be applied to these nodes. Forces should also be applied in areas of the model rather than individual nodes.
8. Once the model is built in Mechanical APDL, a macro called ADAMS.MAC is invoked to create the MNF. Using APDL language instead of the Graphical User Interface, the user must select the interface nodes first, using NSEL command, use command SAVE for possible resume from this point and finally run ADAMS command to save MNF file. The command ADAMS should be followed by a comma and the number of modes to be exported (ADAMS,NMODES). The modes selected to export are the eigenmodes of the component with all degrees of freedom of all interface points fixed.

A modal reduction technique called Component Mode Synthesis (CMS) and also known as dynamic substructuring is used. A slightly modified Craig-Bampton (C-B) method [83] is applied in ADAMS to achieve CMS. According to this theory, the motion of a flexible component with interface points can be described by its component modes that are the sum of the interface constraint modes and the interface normal modes. To obtain the constraint modes, a unit displacement is applied to each of the 6 DOFs of each interface node to get the static mode shape for that unit of movement. The normal modes are obtained by fixing all DOFs of the interface points and perform an eigensolution. The principle of linear

superposition is used to combine all mode shapes at each time step to reproduce the total deformation of the flexible body. All C-B formulation can be found in [4, 83, 84].

The MNF contains the information about the modal reduction of the FE model, which includes the following information:

- header containing the date that was generated, ANSYS version, title, MNF version and units;
- body properties, such as mass, moments of inertia and centre of mass;
- reduced stiffness and mass matrices in terms of the interface points;
- interface normal modes that are requested by the user when using ADAMS command;
- interface constraint modes.

Since the interface points correspond to the rail position on top of the sleepers, the boundary conditions to get the mode shapes coincide with rail support locations. As above mentioned, two types of modes are generated, the constraint and the normal modes.

Once the rail flexible body is imported into VI-Rail, its vibration modes can be reviewed, animated or even disabled their contribution for the dynamic analysis. Figure 3.6 shows the first five vertical bending mode shapes of a rail beam imported from ANSYS to VI-Rail. The first 6 modes of the flexible body are unwanted rigid body modes from the C-B analysis and must be disabled. Accessing the list of flexible body modes and their frequencies is done through the VI-Rail GUI, going to rigid body attributes and Modal ICs.

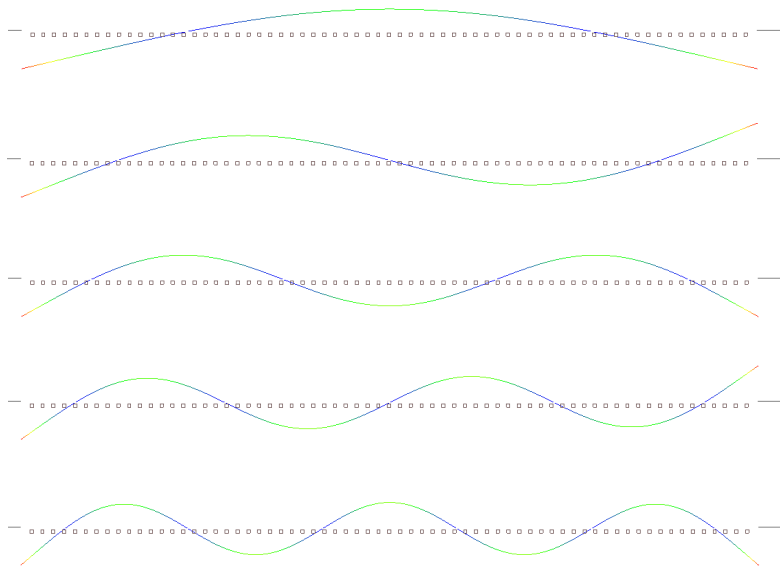


Figure 3.6. Flexible body animation tool – first 5 vertical bending modes of the rail beam.

The flexible bodies should be stored in the “flex_bodys” folder on VI-Rail database. When creating these flexible bodies, a percentage contribution of the total mass from the part can be applied to the sprung mass. Since flexible bodies cannot include floating markers, elements like GFORCE cannot be attached and they cannot be used as J part (reference one). In order to connect the flexible bodies to the remaining model and to apply GFORCES, such as the ones used for the contact routine, optional dummy parts, called Interface parts have to be created. The interface part is created and linked to the interface point position and requires the node number from the FE model. In this case, the interface points are on the rail centre of mass and on top of the sleepers. These dummy parts allow creating markers on the rail head position used for contact and on the rail foot position for rail-pad attachment.

3.1.4 Model d: In-house vehicle-track interaction model built in MATLAB

A 2D vehicle-track interaction (VTI) model built in MATLAB and based on FE theory is used for the comparison [65]. Each rail node has two DOFs, which are vertical displacement, and pitch rotation. Four Timoshenko beam elements are considered between sleepers to represent the rail. The sleepers are modelled as rigid with only one DOF, namely, the vertical displacements. The rail-pad and ballast resilient layers are represented using linear spring-damper elements distanced by the sleeper spacing, as shown in Figure 3.7. The track symmetry is used to consider only one side of the track where only vertical forces are

transmitted between the vehicle and the track. Here, the Hertzian spring model [85] is used to represent the wheel-rail contact forces. Since it is a 2D model, only half of the vehicle is considered. The vehicle used in the case study later in this chapter comprises two wheelsets, one bogie frame and a half of the carbody, as shown in Figure 3.7. The vehicle model includes a primary suspension to link the wheelsets and the bogie frame and secondary suspension to link the bogie frame and the carbody. The two wheelsets masses and profiles are assumed equal. The dynamic analysis uses an iterative scheme to solve the vehicle-track coupling, that is, the track deformation due to the wheel-rail contact forces and the wheel-rail contact forces due to the track deformation are determined sequentially until a good match is achieved [86].

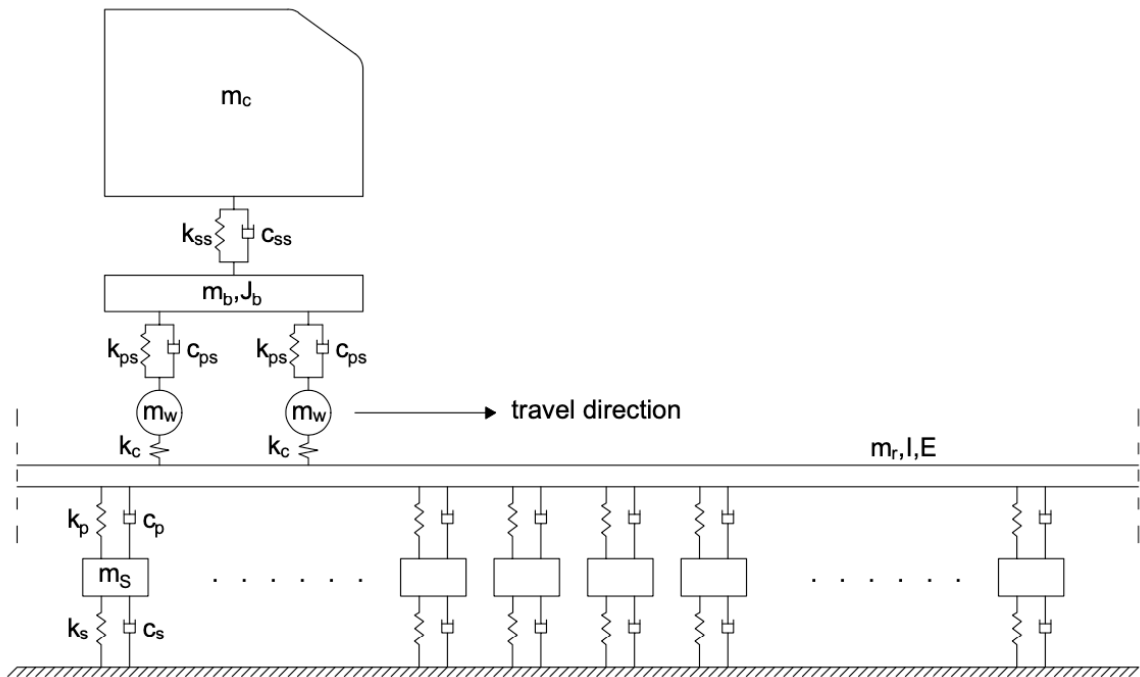


Figure 3.7. FE model built in MATLAB (adapted from [38])

3.2 SELECTION OF THE TRACK MODEL TO STUDY S&C

3.2.1 Case study

The main focus of this thesis is to study S&C behaviour and it is important to select an appropriate track model to study all the particular aspects of a railway crossover and its elements. Four track models were presented, three built inside VI-Rail and one built in-house

on MATLAB. It is important to compare all models and identify the advantages and disadvantages of each.

A plain track case with a total length of 70 m with sleepers spaced by 0.65 m is considered. For the discretely supported track models in VI-Rail, an initial and final section of rigid track have to be considered, meaning that the rails do not move in those sections. For these tracks, the first 23.4 m and the last 6.5 m are rigid, whereas the middle part, which comprises 61 sleepers is flexible.

Three different track irregularities are considered and depicted in Figure 3.8. These irregularities are a short wavelength irregularity, a medium wavelength irregularity and the total irregularity, which combines the previous two irregularities. The medium wavelength irregularity selected intends to simulate a weld [87]. The short wavelength irregularity leads to a high frequency impact load, similar to the wheel passage through a crossing nose. The irregularity is applied equally in both rails, keeping the symmetry of the track along the longitudinal axis. The irregularity is placed such that its maximum is on top of the sleeper in the middle of the flexible track, that is, at 42.90m.

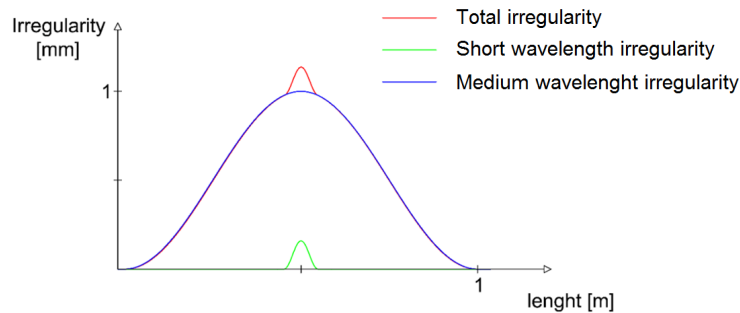


Figure 3.8. Schematic representation of the vertical irregularity.

The sleeper is considered rigid and the rail gauge is 1.435 m. The rail-pads and ballast parameters are obtained based on the EUROBALT report [88]. Table 3.1 lists all track input parameters assuming the scheme shown in Figure 3.10. Models b, c and d directly use the track parameters shown in Table 3.1, while for model a, the parameters are affected by the equivalent track length, calculated from equation 3.3. The value obtained for the equivalent length (L_{eq}) is 1.53804 m, meaning that the track parameters for model a are increased by this factor.

Two vehicle models are considered in this work. The first is the Manchester passenger vehicle [89] and the second a single wheelset, which is the same wheelsets as the Manchester

passenger vehicle. For both models, a speed of 80 km/h is considered, and the time step is 0.05 milliseconds. For the wheelset case, a vertical force of 91.307 kN is applied on the wheelset centre of mass to represent the full axle load of the vehicle. Although the running speed is above the critical speed of the single wheelset, the lateral instability is not observed as there are no lateral excitations in these simulations. Moreover, the advantage of considering the single wheelset model is to provide a simpler model that is easier to replicate, whereas the vehicle model serves to provide more realistic results.

For the track model using MNF, a different ANSYS model is required for each rail of the track (left or right). The BEAM188 elements are used to model the rails, which are based on Timoshenko theory that includes shear deformation effects [82]. The cross-section of the rail is kept constant leading to a constant transverse-shear strain and linear shape functions are considered. No constraints need to be applied as explained in section 3.1.3. Each rail has 63 nodes with all 6 DOFs and 62 beam elements connecting them. These nodes are called interface nodes, since they are used in MBS software to connect to the remaining track model, i.e. to connect to the sleepers through the bushing simulating the rail-pads. When running the ADAMS command in ANSYS, it performs the modal analyses necessary and the constraints for each mode type (normal or constrain). The constrain modes are obtained from a unit displacement applied to each of 6 DOFs from each node, leading to 378 constraint modes (given by 63 interface nodes multiplied by 6 DOFs). Additionally, ANSYS constraints all interface nodes and performs a modal analysis, from which are extracted 100 normal modes (selected by the user), making a total number of 478 modes imported to VI-Rail. Not all of these modes are required for the analysis in VI-Rail. From these 478 modes with frequencies varying between 0.29 Hz and 164,197 Hz, the first 6 modes with frequency around zero are disabled since they are rigid body modes of the track and do not represent the flexible body. Modes above a certain frequency should also be disabled to make the analysis faster. The VI-Rail default damping ratios of the natural modes of the rail are used, which are 1 % for modes under 100 Hz, 10 % for modes under 1000 Hz and 100 % for modes above 1000 Hz.

The discretely supported track models that use the ADAMS beam and the MNF are shown in Figure 3.9 a) and b), respectively. These two models use only one rail beam element between sleepers. Later in this chapter, an increasing number of rail beam elements is studied.

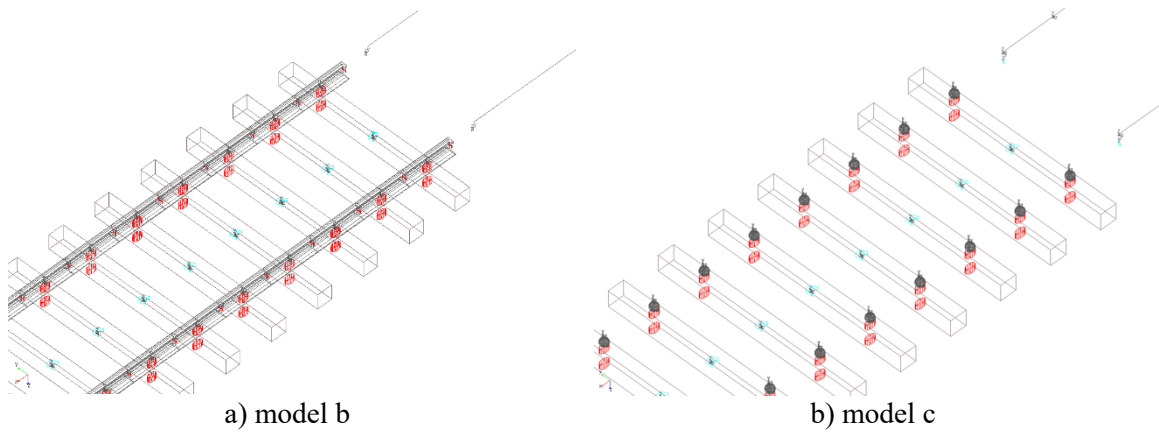


Figure 3.9. VI-Rail discretely supported track model: a) ADAMS beam; b) MNF.

Table 3.1. Track input parameters

Parameter	Value	Unit
Rail profile	60E1	
Steel Young's modulus	210	GPa
Steel density	7850	kg/m ³
Sleeper mass (m_S)	325.0	kg
Rail-pad vertical stiffness (k_{PV})	270.0	kN/mm
Rail-pad lateral stiffness (k_{PL})	400.0	kN/mm
Rail-pad roll stiffness (k_{PR})	470.0	kNm/rad
Rail-pad vertical damping (c_{PV})	1.408	kNs/mm
Rail-pad lateral damping (c_{PL})	1.714	kNs/mm
Trackbed vertical stiffness per sleeper end (k_{BV})	100.0	kN/mm
Trackbed lateral stiffness per sleeper end (k_{BL})	50.0	kN/mm
Ballast vertical damping (c_{BV})	1.451	kNs/mm
Ballast lateral damping (c_{BL})	1.026	kNs/mm

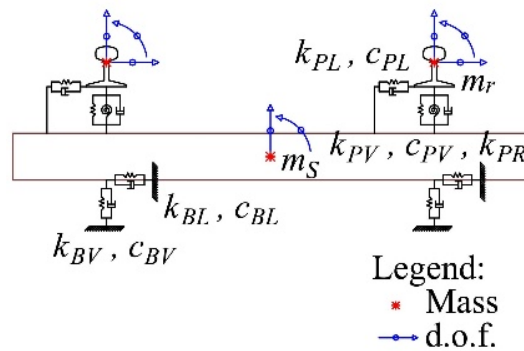


Figure 3.10. Track model scheme.

3.2.2 Results for single wheelset

Before the dynamic analysis, VI-Rail performs a ‘static analysis’ that adjusts the height of the vehicle model to balance the vertical wheel-rail contact forces and the vehicle weight, which eliminates possible initial transient loads from the vehicle model not placed correctly. For the case of a single wheelset, since the static analysis does not find the initial position within the 50 iterations, high frequency on the vertical contact forces is observed in the cases where the wheelset model negotiates rigid track segments, which are the cases of model b and c. This consists of a numerical issue that happens when no suspension is considered and when the normal contact force does not capture properly the restitution effect in the wheel-rail contact [51, 90]. VI-Rail allows the introduction of damping on the normal contact which can reduce the noise observed in the vertical force. Figure 3.11 shows the contact forces for three values of damping ratio. By default, the software considers a value of damping ratio of 0.1 %, which still shows high frequency before reaching the flexible part of the track. For the case where 1 % and 5 % damping ratios are used, it is observed that the numerical noise reduces before reaching the flexible part of the track, which starts at 23.4 m. When comparing the results from the irregularity, no influence from the three damping values was observed. Therefore, it is expected that increasing the damping ratio of the normal contact force up to 1 % leads to better results on the particular case of the wheelset. For the range of values considered, the damping ratio shows no effect when considering the railway vehicle with all the suspensions modelled and it is kept as the default value for the rest of the work.

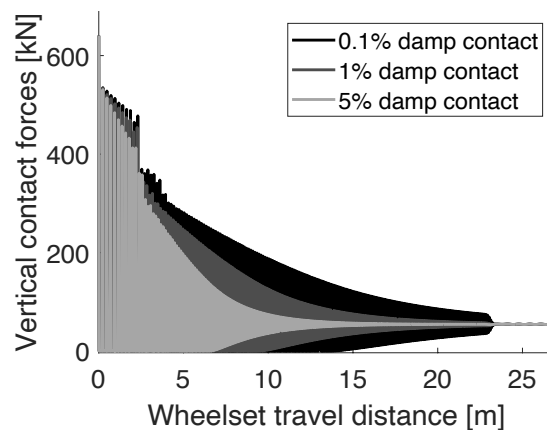


Figure 3.11. Effect of VI-Rail damping ratio in the contact algorithm using the discretely supported track model.

The impact of the number of modes considered for the MNF track model on the dynamic analysis is analysed. Figure 3.12 shows the vertical contact forces for the total irregularity when considering modes from up to 500 Hz to up to 164 kHz. The results obtained show high frequency content in the contact forces when a limited range of modes up to a given limit upper frequency is considered. The most logical reason for such a number of modes being required is the use of linear shape functions for beams in ANSYS. This completely abolishes the main advantage expected from the modal superposition method, which is speeding up the dynamic analysis by replacing the structure with a certain number of mode shapes. Using modes up to a very high frequency removes the benefit of using this method. This track model will still be used considering modes up to 3000 Hz, which leads to a decreasing of the computational time by 29% when compared to the case that includes all modes. The analysis time for this track model will no longer be that relevant when compared to the other track models in VI-Rail.

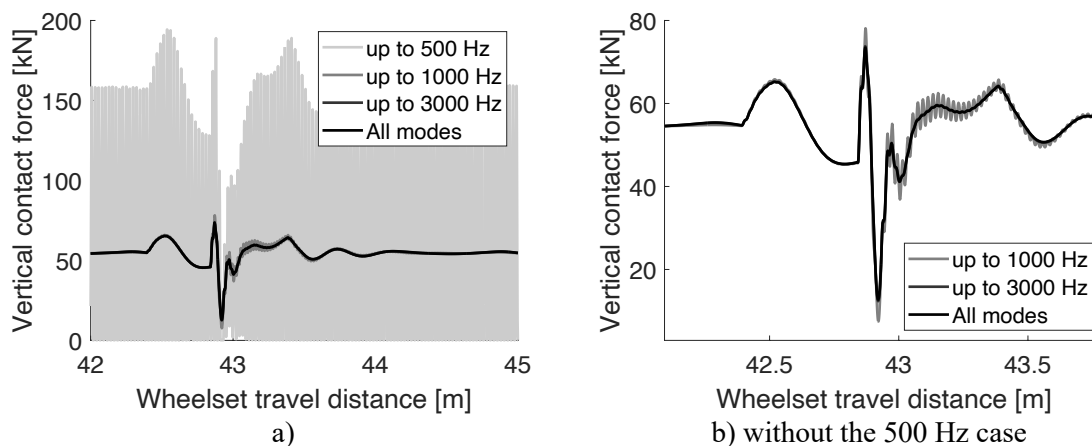


Figure 3.12. Contact forces of VI-Rail track model using MNF.

With all the model assumptions defined, Figure 3.13 shows the vertical contact forces obtained with the four track models for the total wavelength irregularity and the single wheelset. The results show a good agreement between the four models. A good agreement with the other track models for this single plain track geometry is achieved by model a with the parameters affected by the equivalent length. This makes the model a good choice and quick tool to evaluate vehicle dynamics. All three models in VI-Rail (models a to c) show some higher frequency content, which may suggest that the VTI has it filtered. All the discrete track models can capture the sleeper passing frequency, but model d shows small

oscillations within one sleeper spacing that comes from the four beam elements per sleeper spacing.

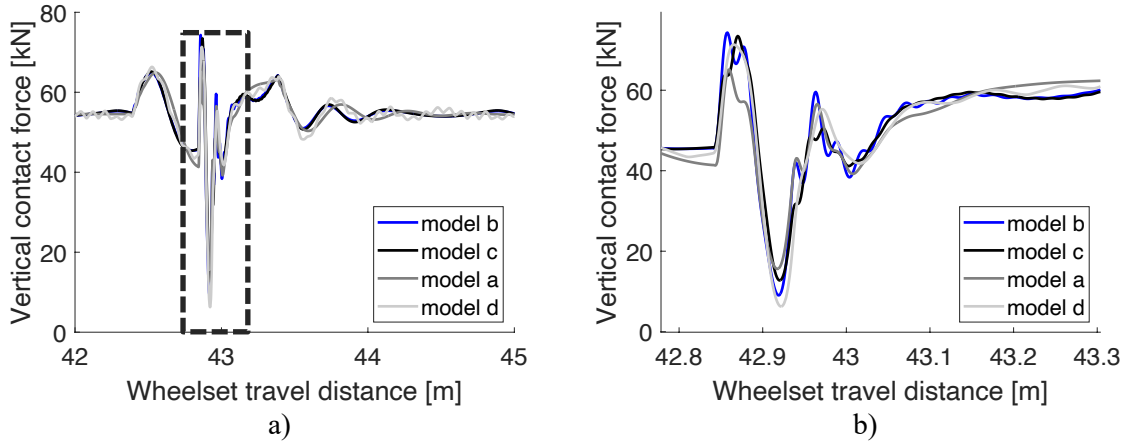


Figure 3.13. Vertical contact force of single wheelset for total irregularity.

When comparing the simulation time for all the VI-Rail models, model a is the fastest model, taking around 53 s to run. Model b takes 21 min and 10 s, which is 23 times more than model a. Model c takes 7h 31 min and 29 s, when considering modes up to 3000 Hz, which is 510 times more than model a and 20 times more than model b. For model c to be competitive, it should use a lower number of modes. Model d takes 65 s to run, which is just 23 % slower than model a. Although it is faster than the other discrete track models, VTI is a 2D model while the others are 3D. The machine used in this work is a 6th generation i7 with 4 cores and 8 threads running at base clock of 3.40 GHz and 32GB of memory RAM.

Figure 3.14 a) and b) show the vertical contact forces for the medium and short wavelength irregularity, respectively. All models capture well the wheelset running over the medium wavelength irregularity. After the irregularity, both discrete track models on VI-Rail show a quicker attenuation on the contact forces which may indicate the models have more damping. Model a shows less damping and cannot capture the sleeper passing frequency, unlike the other models. A good agreement between the four models is also observed for the short wavelength irregularity. Model a presents the highest peak difference compared to model d.

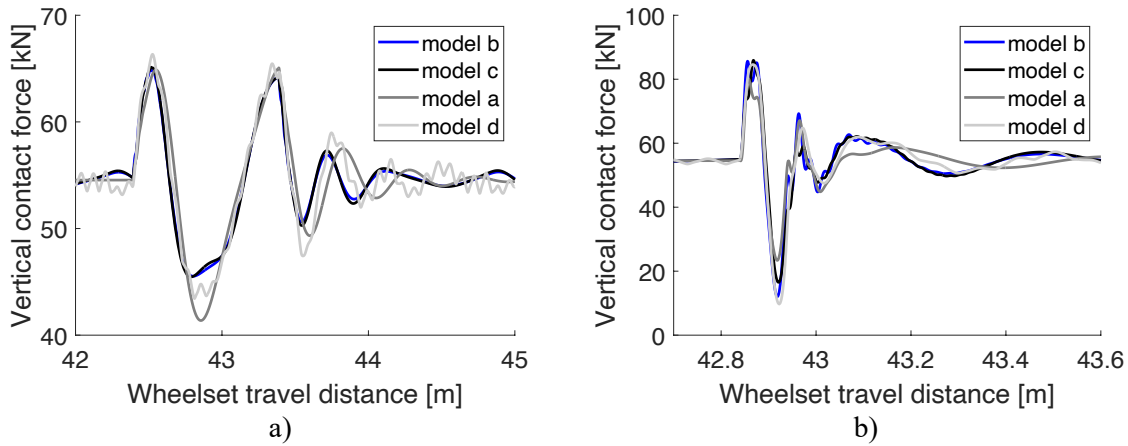


Figure 3.14. Vertical contact forces of single wheelset for: a) medium wavelength irregularity; b) short wavelength irregularity.

Figure 3.15 shows the vertical displacements of the wheelset for the total irregularity. A good match is obtained between all four models around the peak displacement. Both discrete track models in VI-Rail (models b and c) show very similar results and a peak displacement slightly lower than the model d (4 % smaller), and model a shows the highest peak displacement (2 % higher than model d), which may be related to the inability to simulate the rail bending. Looking at the two types of irregularity individually can give a better understanding of the differences.

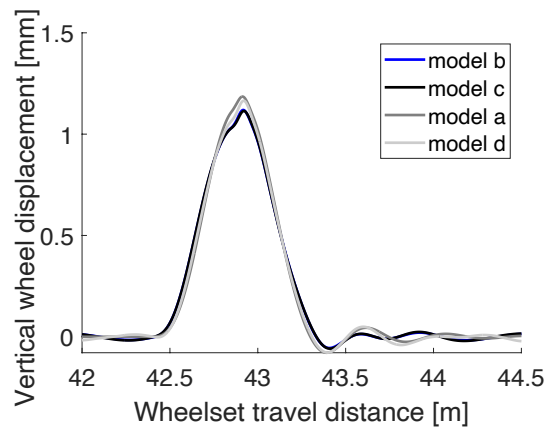


Figure 3.15. Vertical wheel displacements of single wheelset for total irregularity.

Figure 3.16 a) and b) show the wheelset displacements for the medium and short wavelength irregularities, respectively. For the medium wavelength irregularity, the conclusions are very similar to the previous case of the total irregularity. Both discrete tracks in VI-Rail behave similarly with slightly lower peak displacement than model d (4 %

smaller) and model a 1 % higher displacements. For the short wavelength irregularity, a good agreement is observed between all models. Note that the scale of displacements is smaller than the ones observed in Figure 3.16 a), making the differences more noticeable than the previous cases. Here also a good agreement is observed regarding the peak displacement. A better agreement is observed between models b and d, with higher differences after the peak due to VI-Rail being more damped. Figure A.1 in Appendix A shows the receptance curves for three discrete track models compared in [4]. These models are equivalent to the two discrete track models built in VI-Rail and the MATLAB model VTI. From comparing the receptance curves, [4] concluded that both models in VI-Rail show a good agreement for frequencies up to 500 Hz. The pin-pin bending mode from the rail seems to differ with the type of model, leading to higher differences between the four models for events associated with high frequencies, such as the short wavelength irregularity. It is worth mentioning that VI-Rail uses a variable time-step, which can be reduced during the simulation to deal with these higher frequency events, as opposed to the fixed time-step used in VTI. Therefore, the differences between all modes are in the order of hundredth of millimetres.

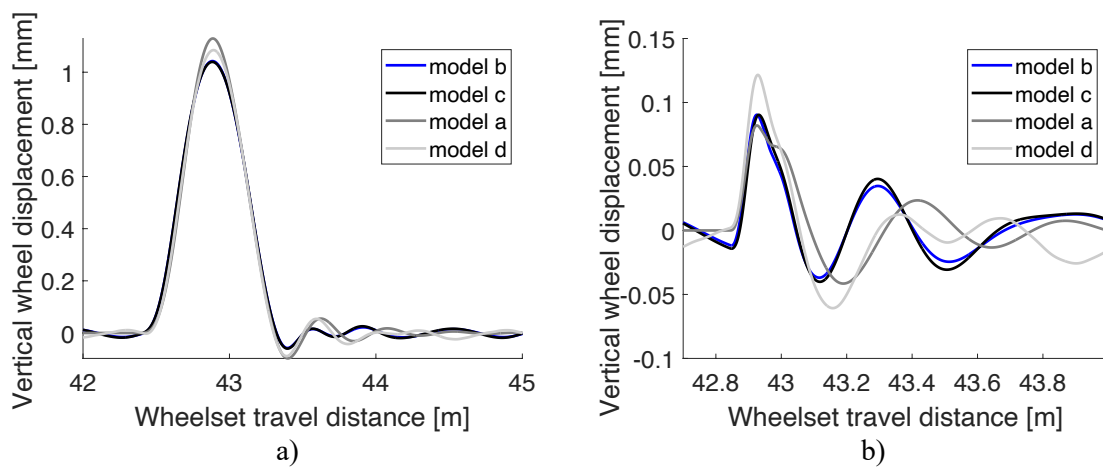


Figure 3.16. Vertical wheel displacements of single wheelset for: a) medium wavelength irregularity; b) short wavelength irregularity

Figure 3.17 shows the vertical displacements of the sleeper placed under the centre of the three irregularities. Here, the continuous track model (model a) is not included as it is unable to consider the sleeper spacing and by consequence the displacements from a particular sleeper. Model b shows smaller displacements, whereas model d shows the highest displacements. Nonetheless, the behaviour of the three models is similar. Since the only difference between the two models in VI-Rail is the type of rail considered, this should be

responsible for the differences observed. These differences are lower than 14 % between models b and c. The same comments are valid for the results shown in Figure 3.17 c) and e). The peak differences between models b and d are 14, 16 and 21 % for the total, medium and short irregularities, respectively. The peak differences between models c and d are 4, 7 and 10 % for the total, medium and short irregularities, respectively.

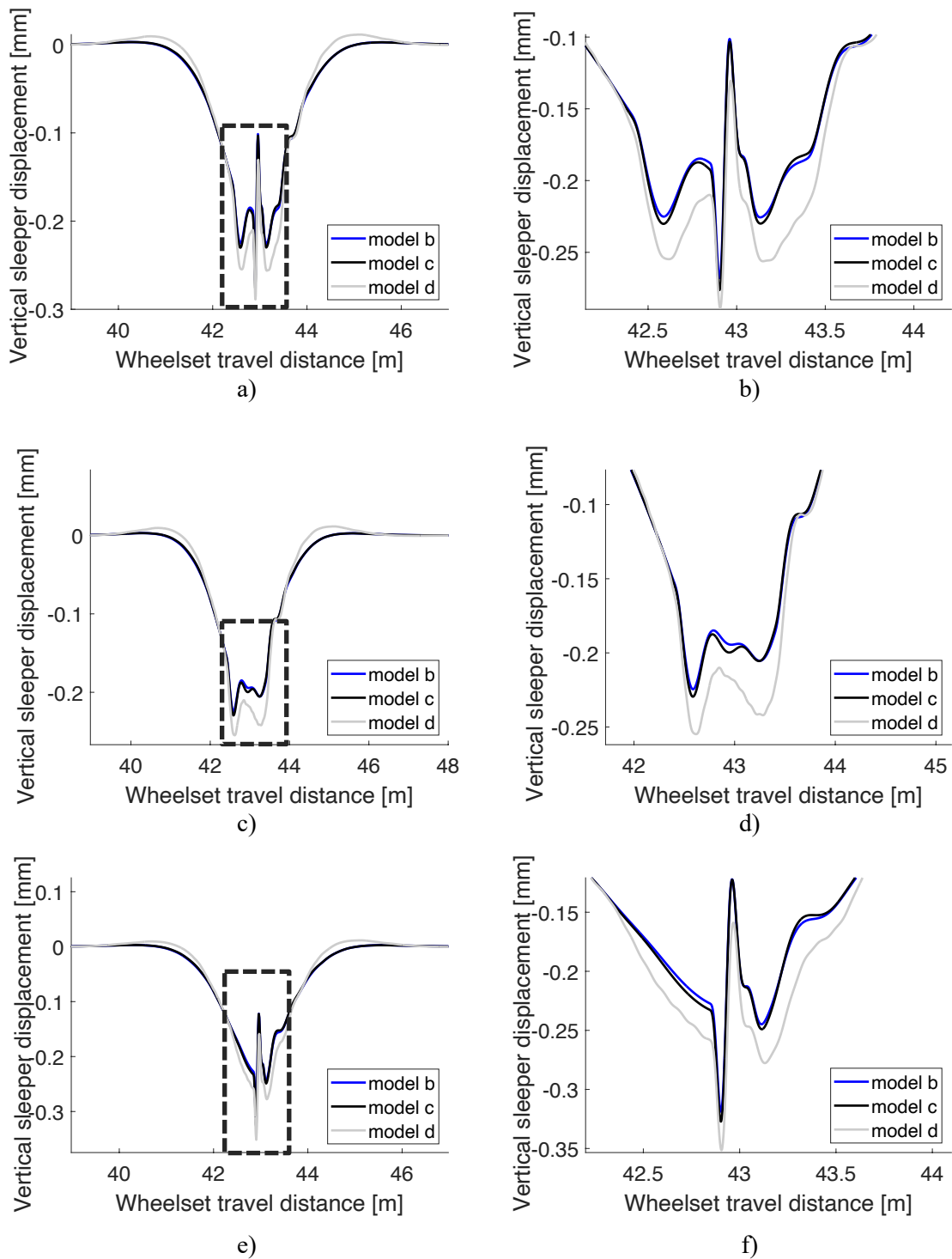


Figure 3.17. Vertical sleeper displacements for: a) and b) total irregularity; c) and d) medium wavelength irregularity; e) and f) short wavelength irregularity.

VTI uses four rail beam elements per sleeper spacing while the discretely track models built in VI-Rail considers only one beam element. Although shape functions are used to distribute the normal contact force to the adjacent rail elements on top of the sleepers, as

explained in 3.1.2, adding rail elements between sleepers is possible. For the case of the ADAMS beam, additional rail parts between sleepers have to be created, since the beam elements need to be attached and connected through rigid bodies. The mass of the rail can be distributed through all that parts instead of being concentrated above each sleeper. The forces and torques coming from the wheel-rail contact algorithm can only be applied to the rail parts above the sleepers and not the middle ones because it leads to a wrong distribution of the contact forces. Figure 3.18 shows the contact forces for the discretely supported track when using up to 4 elements per sleeper spacing. The rail model in ANSYS used to generate the MNF file is also refined, although only the points on top of the sleepers are used as interface nodes when importing the model into VI-Rail, to be attached to the ground and receive the contact forces/torques.

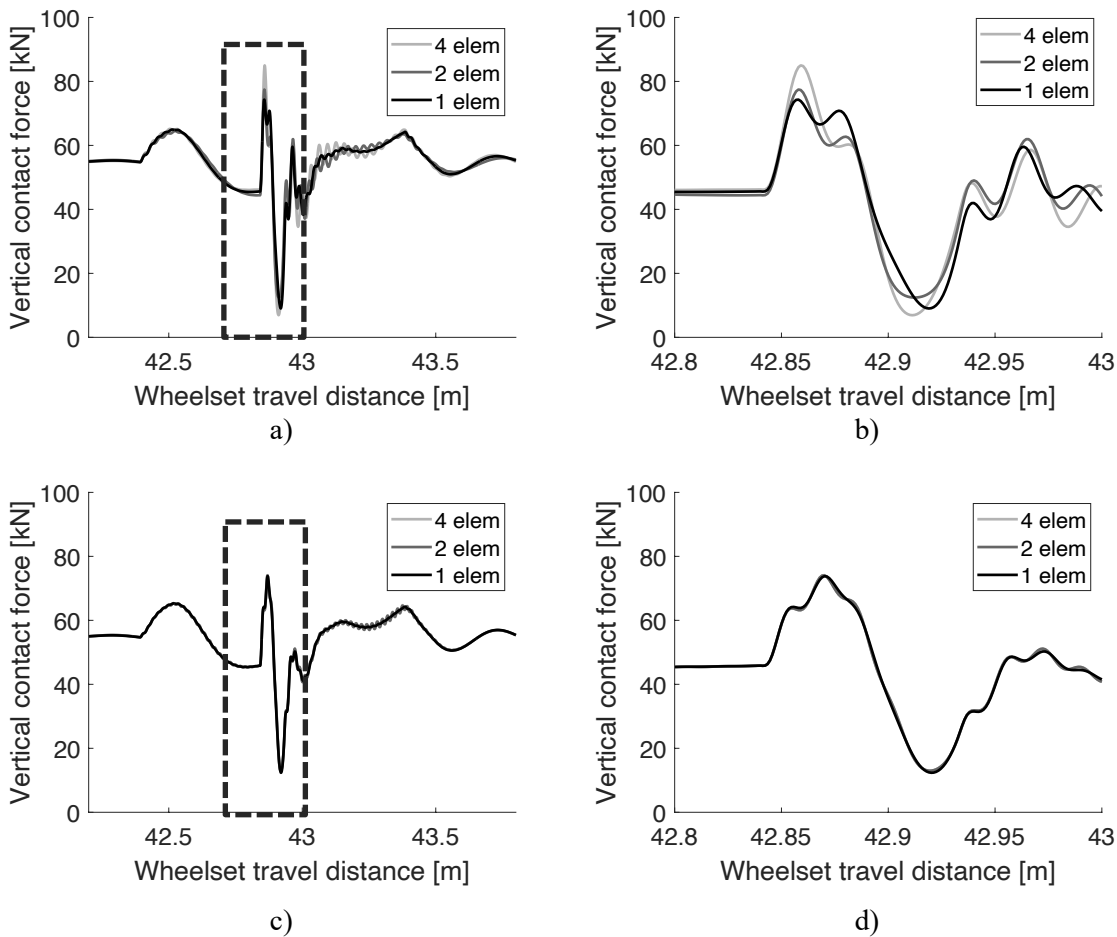


Figure 3.18. Vertical contact forces for up to four beam elements: a) and b) discretely supported track using ADAMS beam; c) and d) discretely supported track using MNF.

The results from Figure 3.18 show high frequency content and higher amplitudes on the contact forces with a finer mesh. Note that, to make the model faster to run, a finer mesh was only considered around the area of the irregularity, i.e. the 10 rails of each side from the peak irregularity. In terms of computational time, the MNF using 2 and 4 beam elements instead of 1 beam element per sleeper spacing leads to an increase of 1.3 and 4.5 %, respectively. For the ADAMS beam, 2 elements lead to an increase of 18% and 4 elements an increase of 34%, when compared to 1 element. For the differences observed in the results, the time increment is not justifiable.

3.2.3 Results for Manchester passenger vehicle

The Manchester passenger vehicle [89] is also used to run the same irregularities simulations cases as considered previously. In VI-Rail the full 3D model is available to use in the VI-Rail library of vehicles. In VTI, the model is simplified considering only two axles, isolated from each other with the corresponding mass of a quarter of the car body and half of the bogie bouncing on top of them. No pitch mode from either bogies or car body is considered. There is effectively no interaction between axles.

Figure 3.19 shows the contact forces and Figure 3.20 the sleeper displacements for all three irregularities. The full vehicle did not require an increase of damping ratio in the contact parameters like it was necessary for the single wheelset shown in Figure 3.11. Since the full vehicle has suspension elements, the contact forces do not show high frequency as dampers in the primary suspension mitigate this numerical problem as discussed in [51].

The contact forces shown in Figure 3.19 show a good agreement between the four models and similar conclusions from the single wheelset case. Overall, all discrete models show similar peak forces while model a has the lowest peak force, 9 % lower for the total irregularity, 2 % lower for the medium and 5 % lower for the short wavelength irregularity. For the medium wavelength irregularity, when the train leaves the irregularity, both models b and c match the model d contact forces, meaning that the damping in all three models is comparable. Model a shows good results compared to the other models, reinforcing the idea that using the corrected track parameters, this type of track model offers a quick option to study the vehicle behaviour on a plain line track.

Figure 3.20 shows the sleeper displacements to all models except model a which cannot study discrete events such as an isolate sleeper movement. Both VI-Rail track models show

closer results to each other, with model b having the lowest peak displacement. Both models show fewer displacements than model d. The case of the medium wavelength irregularity shows the highest differences between the three models, with models b and c giving 12 % and 10 % smaller peak displacements than model d, respectively. In Figure 3.20, the highest differences are seen right after the peak sleeper displacement. This is a result of the load distribution onto the adjacent rail elements in VI-Rail that is simplified in comparison to VTI when the axle is between sleepers. This affects both models b and c and it is the reason for the higher differences when the vehicle passes the top of the irregularity, placed around 20.5 m. Although, those differences are visible in the plot of Figure 20, only the peak values were reported in the summary Table 3.2. It is important to refer the disparities in the results are not only coming from the type of track modelling but also the differences coming from the vehicle modelling.

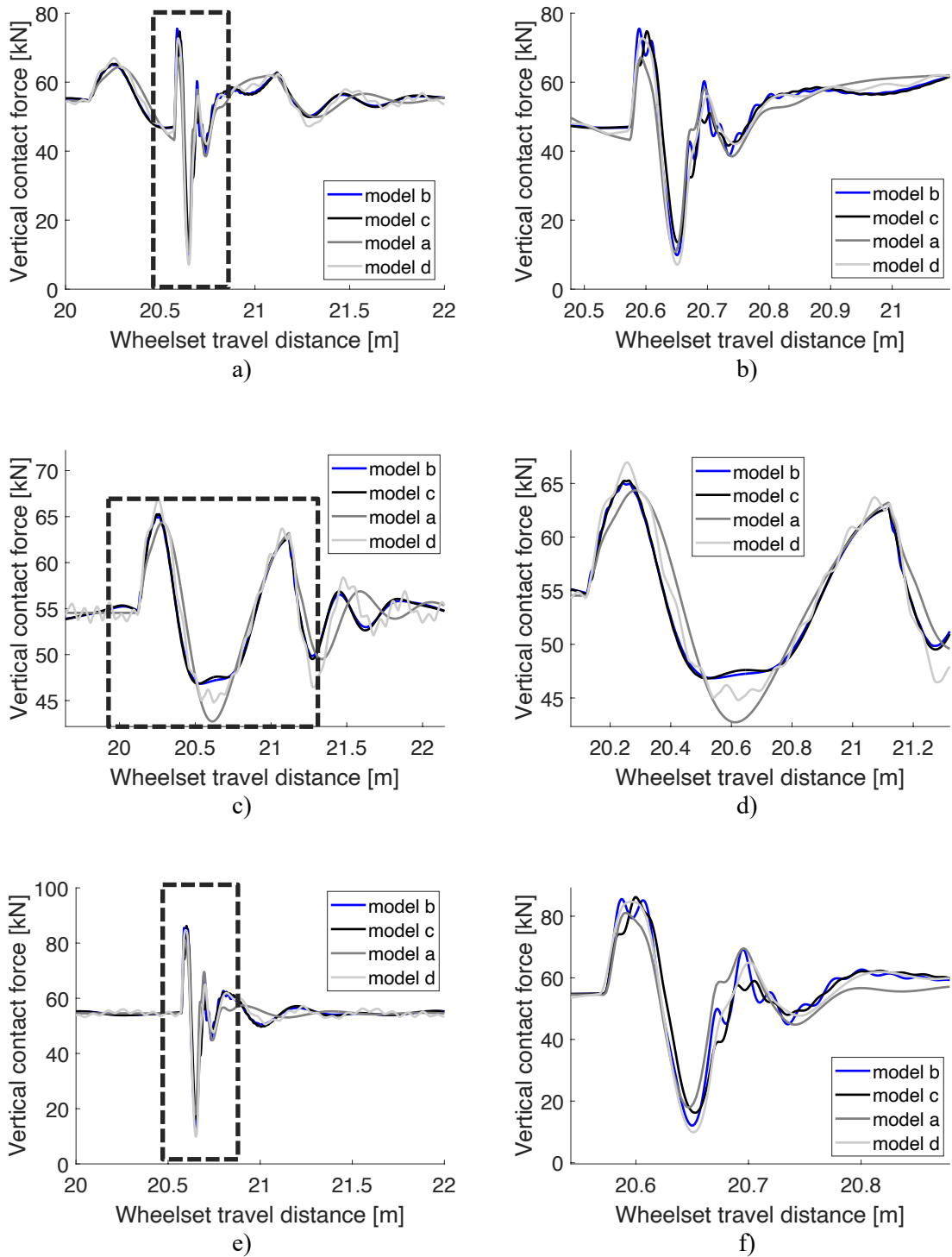


Figure 3.19. Vertical contact forces of Manchester Passenger vehicle for: a) and b) total irregularity; c) and d) medium wavelength irregularity; e) and f) short wavelength irregularity.

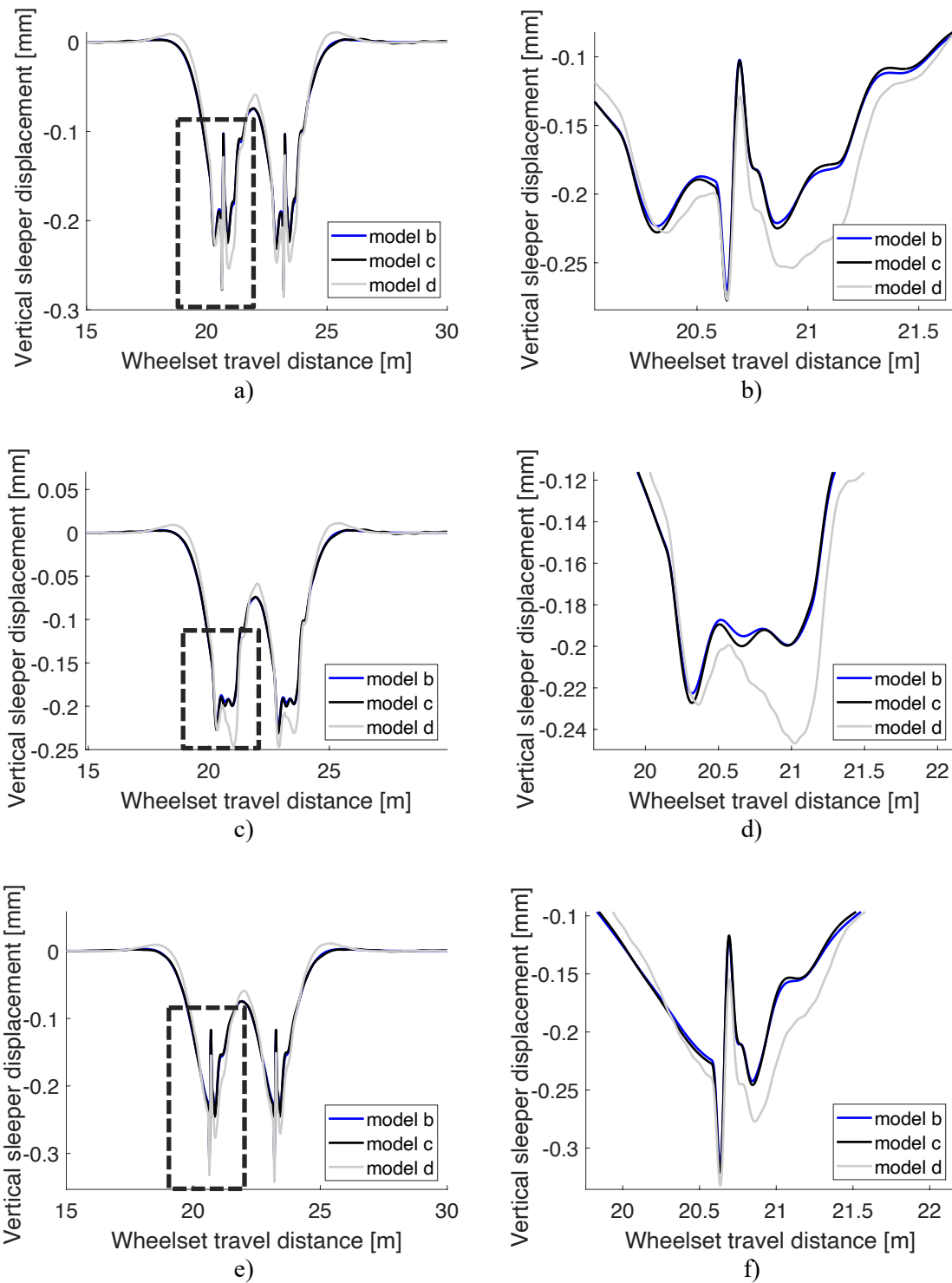


Figure 3.20. Vertical sleeper displacements for Manchester Passenger vehicle for: a) and b) total irregularity; c) and d) medium wavelength irregularity; e) and f) short wavelength irregularity.

3.2.4 Summary of results

Table 3.2 shows a summary of the peak results and the difference when compared to the values obtained from model d (VTI). This model was used as reference here since it has four

rail beam elements between sleepers and the force is directly applied to the beam, rather than distributed between the adjacent rail elements like on both discrete tracks on VI-Rail. “CF” stands for vertical Contact Forces, which are in kN and all displacement values are in mm. With the exception of the wheel displacements for the short wavelength irregularity, all the remaining models have a maximum peak difference of 12 %, which shows a good agreement between all models. For the particular case of the short wavelength irregularity, the bigger differences may be due to the fact VTI uses four rail beam elements per sleeper spacing which leads to a better definition of the rail deformation.

Table 3.2. Summary of peak results

	model a		model b		model c		model d (ref)
	Peak	Diff	Peak	Diff	Peak	Diff	Peak
Single Wheelset							
CF total irregularity	65.11	-9%	74.31	4%	73.47	3%	71.34
CF medium irregularity	64.88	-2%	64.91	-2%	65.13	-2%	66.34
CF short irregularity	80.18	-5%	85.65	1%	85.94	2%	84.58
Sleeper displ total irreg	-	-	0.2678	-7%	0.2763	-4%	0.2888
Sleeper displ medium irreg	-	-	0.2245	-12%	0.2295	-10%	0.2548
Sleeper displ short irreg	-	-	0.3188	-9%	0.3272	-7%	0.3515
Wheel displ total irreg	1.185	2%	1.119	-4%	1.114	-4%	1.165
Wheel displ medium irreg	1.129	4%	1.043	-4%	1.039	-4%	1.085
Wheel displ short irreg	0.082	-33%	0.09	-26%	0.09	-26%	0.1215
Manchester Pass Vehicle							
CF total irregularity	67.16	-8%	75.52	4%	74.69	3%	72.71
CF medium irregularity	64.35	-4%	64.96	-3%	65.26	-3%	66.95
CF short irregularity	81.12	-4%	85.54	1%	86.22	2%	84.65
Sleeper displ total irreg	-	-	0.2698	-3%	0.2775	0%	0.2769
Sleeper displ medium irreg	-	-	0.2227	-10%	0.2273	-8%	0.2467
Sleeper displ short irreg	-	-	0.3157	-5%	0.3212	-3%	0.3321

3.3 CONCLUSIONS

In this chapter, four track models are described and compared through numerical simulations with focus on the vehicle-track interaction and the aim of identifying the advantages and drawbacks of each model. The track models considered are the continuous supported track model and three discretely supported track models, two built in VI-Rail and another built *in-house* using MATLAB and named VTI. Two distinct methodologies are adopted to build the discrete track in VI-Rail, the first directly modelled inside VI-Rail using

ADAMS beam element, which is a Timoshenko based model, and a second approach where the rail is modelled from modal data obtained from the FE software ANSYS. A plain line case with a short and medium wavelength irregularity was used to compare all four models.

The following conclusions are drawn:

- The continuous track model main advantage is its small simulation times compared with the other options. It is a commonly used tool to study vehicle dynamics. However, this track model has limitations, such as: limited information from the track behaviour and its components and discrete events like unsupported sleepers or rail properties changing abruptly (S&C) cannot be modelled.
- The modal reduction technique allows to build complex rail geometry variations along the track with very detailed mesh in a FE software and import the modal data to MBS software using Modal Neutral Files (MNSs) A careful selection of the frequencies of interest and modes considered is required for this technique which will affect both the results and the simulation times. In this work, the track model has shown some errors when considering fewer modes and only gave good results using modes up to 3kHz. This led to very long simulations and therefore is not deemed appropriate for the follow-up studies. It is however recognised that if simulation time is not an issue and if a reduced, but enough number of modes are selected, this type of model can be a good option.
- The discretely supported track model built entirely inside a MBS software has the advantage of not requiring additional FE software to build any part of the track and still consider the rail discretely supported. It allows to study localised event such as badly supported sleepers or defective rail-pads and consider variable sleeper spacing as well variable support conditions, with different values below each sleeper and from left and right side. In comparison with the continuously supported track model, it allows studying all the track structure below the rails, such as: rail-pads, sleepers and ballast. It is possible to model the full layout of a crossover and can be used to study particular elements of the track, such as long bearer connections or platform connections. It can be updated to consider the sleeper flexibility as well replace the linear spring-dashpot elements used for both rail-pad and ballast with the non-linear ones. In comparison with the in-house VTI model, building a model inside a MBS software allows to use robust and validated

wheel-rail contact algorithms as well as a library of highly detailed and validated vehicles models. This seems to be the most versatile approach to study S&Cs.

- The number of rail beam elements considered per sleeper spacing was also studied in this chapter. No difference was observed on the contact forces for the plain line case and should have been studied as an example of a crossing or switch element.

Thus, the discretely supported track model using ADAMS beam (model b) is used in the next chapter where a full railway crossover is modelled.

4 NUMERICAL MODELLING OF A RAILWAY CROSSOVER

This chapter presents the detailed numerical model of a railway crossover, using the discretely supported track model and built in VI-Rail. The selected study site is one of the few sites in the UK with Under Sleeper Pads (USPs) installed and to have site measurements available at the time this work started. The geometry of the full crossover is developed in AutoCAD and exported afterwards to VI-Rail. A detailed description of all the modelling phases and all the parameters adopted is given.

Later in the chapter, a modelling approach is introduced to take into consideration the bearers flexibility in VI-Rail. This model is then compared with a FE model built in ANSYS. The approach suggested showed a good match with the FE results, both in terms of modal analysis and bearer displacements when the rails are loaded.

4.1 GENERAL DESCRIPTION

The railway crossover considered in this work joins two mainlines, identified as Up and Down as shown in Figure 4.1, left-hand side, which includes two crossing panels. The complete site is approximately 250 m long with a maximum operating speed of 177 km/h (110 miles/h). Traffic runs on both mainlines, but is rarely used in the turnout direction (service vehicle and emergency).

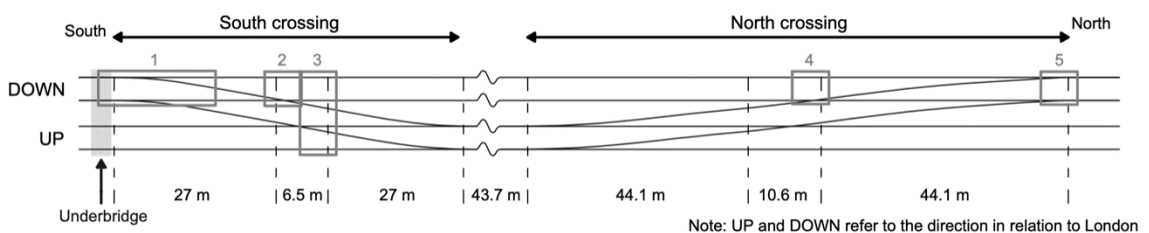


Figure 4.1. Schematic plan of the study site (adapter from [91]).

The work presented here focuses on the south crossing spanning about 60 m, with trains running on the Down line through direction only. The S&C starts right after a concrete-reinforced masonry underbridge marked in Figure 4.1 and it is a right-hand side turnout, where the switch stock rail wheel transfer occurs on the right-hand side, labelled “6ft”.

Figure 4.2 a) shows the switch panel, and Figure 4.2 b) the crossing panels. The crossing has a 1 in 13 crossing angle and 245 m turnout radius. Check rails and long bearers are present on the crossing panel (see Figure 4.2 b). The long bearers are connected by a bolted steel collar, visible in Figure 4.2 b), thus spanning the entire width of the Up and Down tracks. This type of connection is an approved design from Network Rail (UK) that restricts relative movement and rotation. The crossing is made of one cast manganese piece with higher cross-section properties than plain line rail.



a)



b)

Figure 4.2. a) The switch panel and b) the two southern crossings. Both photos were taken pointing north [5].

The track section studied in this work was subject to a renewal in December 2012. In this intervention, the replacement of the rails, sleepers and bearers, ballast up to 300 mm depth and other track components have been performed. Two types of USPs were installed during the renewal (Figure 4.3), intended to promote a smoother transition in trackbed stiffness from the switch panel to the crossing panel. All long bearers were fitted with soft USPs, except the four bearers on either side of the crossing, which are fitted with medium stiffness USPs. A total of 29 bearers before the connected ones were fitted with medium stiffness USPs depending on the traffic direction. While the choice of USP modulus was calculated and defined by the supplier Getzner (values in Table 2.1), it was not clear to the Network Rail whether the choice of having two different modulus was the best choice or if the modulus itself was the best one to use at the site. Therefore, it would be important to study these design choices in this work.

Figure 4.3 shows the naming convention used in this document that identifies the different areas of the track. 4 foot (4 ft) refers to the area between rails of the same line, 6 foot (6 ft) refers to the area between lines and the Up cess and Down cess to the outer area of each line.

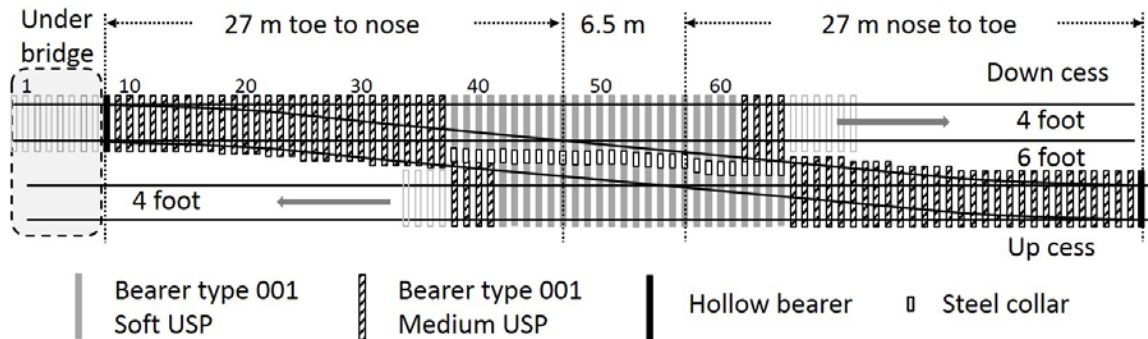


Figure 4.3. Site overview. The numbered bearers identify monitored locations [92].

4.2 NUMERICAL MODEL AND MECHANICAL PROPERTIES

From the three VI-Rail models analysed in the previous chapter, the discretely supported track model using the beam available directly in ADAMS was selected, without requiring an FE software. To build the full crossover model, the technical drawing for the renewal of the site was used to define the S&C geometry in AutoCAD. Rail and sleeper/bearer coordinates are exported from AutoCAD, stored and manipulated in spreadsheets to use later as an input to create the model in VI-Rail. All the three routes are modelled, namely, the Up and Down through routes and the Down diverging route. In EXCEL, a 4th-degree polynomial

that fits the rail positions of the diverging route is created in order to get the rail orientation, obtained from the polynomial derivative. As mentioned in the previous chapter, the track model in VI-Rail is entirely built by a script using Adams / VI-Rail language (.cmd).

VI-Rail help document [93] contains an example with code to create a single-track model. The model initiation starts with a code to check if a model with the same name exists and if it does not, it creates one with the given name. It is normal practice to create an initial point as a reference, usually with coordinates (0,0,0).

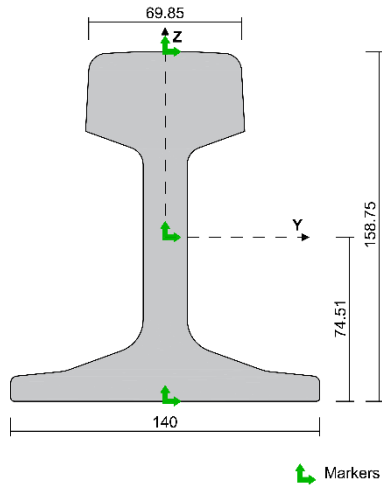
Points with coordinates and orientations are built along the track centrelines to use as a reference to build most of the model. In VI-Rail, *construction frame* elements are used for this task. Their longitudinal position matches the rail and sleeper locations and takes into consideration not only the flexible part of the track but two rigid sections, before and after each line. These two sections of rigid track, the first with approximately 22 m long and the second 7 m long, are considered in order to calculate the initial static position of the vehicle and also allow the vehicle to traverse the flexible part of the track fully. Fixed markers are used to represent the rigid sections of the track, and some graphics (additional) can be added. Markers are modelling elements identifying a location but also an orientation. These markers are stored in a list used to create later the generic force elements that receive the forces from the wheel-rail contact routine.

4.2.1 The rails

The rails are CEN56E1 and CEN56E1A1 [15] after the twist rails transition, which happens between bearers 3 and 4, moving from 1 in 20 inclination to vertical rails. Table 4.1 shows the properties of this rail type used in the numerical model. The track gauge is 1435 mm, except for the crossover where it reduces to 1432 mm. In VI-Rail, rails are modelled as *general parts* and connected with beam force elements. A *general part* is a generic rigid body defined by its location, orientation, mass, inertia and centre of mass offset from location. The rails mass is concentrated in the rail parts and not distributed along the beam. In VI-Rail, several markers are created to connect the rails rigid bodies to the rest of the track and are represented by green reference frames in Figure 4.4. These markers are: a marker on top of the rail to use as a reference for the contact algorithm, a marker used to create the rail pad connecting the rail and the sleeper, a marker used as a reference to create rail graphics

(which in this case coincides with the top marker for contact) and a marker to connect the beams to adjacent rail elements. The rails rigid body elements have all 6 DOFs.

Table 4.1. Stock rail properties



Parameter	Value and Unit
Linear mass	56.3 kg / m
Ixx	1.960E-006 m ⁴
Iyy	2.321E-005 m ⁴
Izz	4.210E-006 m ⁴
Area	7.169E-003 m ²
Young modulus	2.1E+011 Pa
Shear modulus	$E / (2 \times (1 + 0.288))$ Pa
Shear area ratio Y	0.4
Shear area ratio Z	0.55
Damping ratio	1.0E-004

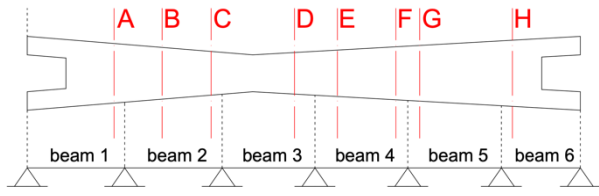
Figure 4.4. Rail CEN56E1 (mm)

The beams connecting the rail parts are massless beams based on the Timoshenko theory. Each beam is defined by three moments of inertia, area of the cross-section, beam length, Young's and shear modulus, the shear ratio of area around Y and Z axis, damping ratio and two markers from the two bodies to be connected. The beam cross-section is kept constant. To avoid having rigid bodies and beams with very small mass and area, respectively, the rails from the diverging route are only considered when the switch rail reaches its full rail head width, i.e. the distance between the rail top centre of switch and the stock rail are bigger than the rail head width. From the switch toe up to this position, only one rail beam is considered with properties equal to the sum of properties of the two independent rails being connected. With this assumption, no relative movement between the switch and stock rails is considered. After that point, two separate rails are considered (see Figure 4.9 a)). Since only the Down through route was studied, the switch blade leans on the right stock rail.

In the crossing panel, the same modelling approach is used, and the increased crossing properties are considered by including a few factors affecting the area, mass, yaw and roll inertia of the rail parts. These factors are stored in the input tables used to build the model and are kept equal to one for the plain line stock rail and higher when in the crossing panel. Cross-sections A to H, as shown in Figure 4.5, have been created in AutoCAD, from which

their mass and inertia properties are obtained. The properties of the six beams composing the crossing element, which are shown in Table 4.2. where obtained through linear interpolation between the properties from the cross-sections shown in Figure 4.5. The values presented are factors relative to the stock rail. For example, a value of two would mean two times bigger than the stock rail. Between sleepers, the beam properties are kept constant.

Table 4.2. Crossing element properties relative to stock rail



beam 1	A	1.94093
	I_{roll}	7.127078
	I_{yaw}	2.585954
beam 2	A	2.977715
	I_{roll}	12.06176
	I_{yaw}	4.504093
beam 3	A	2.972866
	I_{roll}	11.11876
	I_{yaw}	4.348988
beam 4	A	2.554282
	I_{roll}	8.307601
	I_{yaw}	4.334769
beam 5	A	2.259729
	I_{roll}	8.448931
	I_{yaw}	3.895735
beam 6	A	1.616944
	I_{roll}	5.997625
	I_{yaw}	2.132917

Figure 4.5. Cross-sections locations from the crossing

4.2.2 Sleepers and bearers

The site uses pre-stressed concrete sleepers type G44 on the plain line and bearers type 001 on the crossover length. These types of sleepers/bearers are commonly used in UK railway network. The sleeper type G44 measures a nominal length of 2.6 m, as shown in Figure 4.6, and weights 312 kg, including the fastening components. For the areas in the 2012 renewal plan with no sleepers identified, it was assumed to be G44 sleepers with a constant sleeper spacing of 0.65 m. For all the bearers on the S&C, a variable sleeper spacing is considered, according to their locations on the renewal plan.

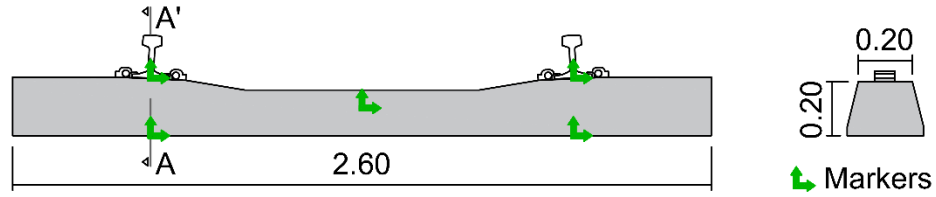


Figure 4.6. Scheme of concrete sleeper type G44 (m).

Along the crossing panel, increasing length bearers of type 001 are used to prevent lateral movement of the two tracks. The mass of each bearer is calculated as a linear increase of the mass from the sleeper G44 equal to the increase in length. The bearers around the crossing panel, between bearer 38 and 65, are joined with steel collars and bolts (see Figure 4.2 b)) an approved design by Network Rail, which intends to act as a rigid connection. The total length from each pair of bearers connected is around six meters. In this particular site, the connection is located always between the rails of the diverging route, as shown in Figure 4.2 b).

In VI-Rail the sleepers and bearers are modelled as rigid bodies with mass proportional to their length compared with the nominal sleeper G44 length. Their moments of inertia are obtained by:

$$I_h = \frac{1}{12} m (w^2 + d^2) \quad (4.1)$$

$$I_w = \frac{1}{12} m (d^2 + h^2) \quad (4.2)$$

$$I_d = \frac{1}{12} m (w^2 + h^2) \quad (4.3)$$

where m is the mass, h and w are the height and width, respectively, and considered equal to 0.2 m, and d is the sleeper length (depth).

Same as for the rails, markers are created for each sleeper body to connect them to the remaining structure: markers to create the rail-pad (attach sleeper to the rail), markers to create the sleeper support (attach to the ground) and markers to constrain some sleeper motions. Figure 4.6 shows the markers used to define a sleeper by the reference frames highlighted in green. Each sleeper element has 3 DOFs, vertical and lateral translation and roll rotation. The remaining movements are constrained using motion constraint elements.

On the crossing panel, the vertical and lateral motions and roll rotation between bearers of the two tracks are constrained on the position of the steel collar.

4.2.3 Fastening and trackbed support

Elastic clip type fasteners are used on this site to fix the rails to the sleepers or bearers, which is one of three commonly used types of fasteners for concrete bearers. Baseplates installed around the switch panel allow the switch blades and switch rails to change the turnout configuration between through route or diverging route. A linear bushing element is used in VI-Rail to consider the rail-pad flexibility between rails and sleepers. The bushing element resists all relative motions through reaction forces that are proportional to relative linear and angular displacement and velocity, and therefore stiffness and damping values are defined for the three directions and three rotations. The bushing elements parameters require identification as they are not directly known. Since the site was renewed not a long time ago and as a common practice, a relatively soft pad was assumed of value 120 kN/mm. The parameters adopted are shown in Table 2.1. These values were an approximation and were assumed constant through all the site length as no further information is available at the time of this study.

Two USP types were fitted underneath the bearers along the site. Soft and medium pads with stiffnesses of 53.5 and 78.5 kN/mm per sleeper end, respectively. These values are obtained from the static modulus of the pad and the bearer bottom area [91]. The trackbed stiffness, including ballast and all layers below, without USP installed, were considered equal to 40 kN/mm per sleeper end [64]. To get the equivalent trackbed stiffness with USP, two springs in series are considered, combining the USP and the support below as defined by:

$$\frac{1}{K_{eq}} = \frac{1}{K_{USP}} + \frac{1}{K_{support}} \quad (4.4)$$

Lateral stiffness was assumed as 50% of the rail-pad vertical stiffness and 25% of the trackbed stiffness, for the rail pad and ballast respectively. The damping is calculated as a function of the stiffness using the equation below:

$$C = \eta \times K \frac{1}{2\pi f} \quad (4.5)$$

where η is the loss factor, K the stiffness (vertical or lateral) and f is the frequency from the mode shape of the rail vibrating on the pads, considered as 250 Hz [94]. The loss factor is assumed 0.6 for the rail-pad and 1.0 for the trackbed. The linear bushing elements representing the trackbed stiffness and damping are applied below the bearers from Up and Down through routes, as shown in Figure 4.11 a).

Table 2.1 summarises the model parameters pad and ballast stiffness and damping parameters. The rail-pad and trackbed stiffness values were adopted the same as [95, 96]. The value for the trackbed stiffness is an initial assumption and it is calibrated in Chapter 5. Symmetry along the track centre line is assumed for the long bearers, i.e. the same stiffness values are assigned to 6ft and cess side on both tracks (see Figure 4.11 a)).

Table 4.3. Model pad and ballast stiffness and damping parameters

Parameter	Value	Unit
Rail-pad vertical stiffness	120.0	kN/mm/sleeper end
Rail-pad lateral stiffness	60.0	kN/mm/sleeper end
Rail-pad longitudinal stiffness	60.0	kN/mm/sleeper end
Rail-pad rotational stiffness along vertical axis	0.338×10^{-3}	Nm/mm/sleeper end
Rail-pad rotational stiffness along lateral axis	6.83	Nm/mm/sleeper end
Rail-pad rotational stiffness along longitudinal axis	6.83	Nm/mm/sleeper end
Rail-pad loss factor (damping)	0.6	
Trackbed vertical stiffness (no USP)	40.0	kN/mm/sleeper end
Trackbed lateral stiffness (no USP)	10.	kN/mm/sleeper end
Trackbed loss factor (damping)	1.0	
Soft USP vertical stiffness	53.5	kN/mm/sleeper end
Soft USP lateral stiffness	13.4	kN/mm/sleeper end
Soft USP loss factor (damping)	0.2	
Medium USP vertical stiffness	78.5	kN/mm/sleeper end
Medium USP lateral stiffness	19.6	kN/mm/sleeper end
Medium USP loss factor (damping)	0.2	
Trackbed vertical stiffness (with soft USP)	23.6	kN/mm/sleeper end
Trackbed lateral stiffness (with soft USP)	5.9	kN/mm/sleeper end
Trackbed vertical stiffness (with medium USP)	26.5	kN/mm/sleeper end
Trackbed lateral stiffness (with medium USP)	6.6	kN/mm/sleeper end

4.2.4 Output and track file creation

Once the model is fully developed, additional requests can be created in VI-Rail which are used to get information such as displacements, velocities and accelerations in specific locations of the model. In VI-Rail, the VI-Flextrack plugin is loaded to complete the discretely supported track model. This plugin was developed by [4] and allows creating *general force* elements to the markers on top of the railhead. These *general forces* receive

the forces calculated from the contact routine, as explained in the previous chapter, Section 3.1.2.

The plugin also generates automatically a track file with the coordinates from all markers previously selected. In the track file, a constant rail profile and rail inclination are specified. It also specifies the path the vehicle will run on, track irregularities, the gauge and rail profiles. The track file generated from the plugin can be modified later to include for example the switch and crossing profiles definition. There are two types of track file, depending on how the path for the vehicle is described and they are named as measured or analytic. The first one defines track path by the coordinates along the track distance path and the second one gives key coordinates where curvature change are defined. Both types can consider variable rail profiles but the rail irregularities definition did not work for the ‘measured’ track definition, maybe just a problem from the VI-Rail version used. The ‘analytical’ type of track was therefore chosen to work with. Since only the Down through route is being studied in this work, no curvature is needed, and the rail was always assumed vertical even outside the crossover positions (i.e. the twisted rail was not included).

The as-new rail geometry was assumed for both switch, stock rails and crossing. These elements were defined through a series of 2D profiles cross-sections spaced between 20 to 50 mm between them where the rail cross-section shape changes rapidly. VI-Rail uses a 3D interpolation algorithm to calculate the rail shape at each iteration step at the longitudinal position of the wheel as a function of these input profiles. Figure 4.7 a) shows the profiles used for a vertical CV type switch and Figure 4.7 b) the profiles used for an inclined wing rail cast monoblock crossing with a $9\frac{1}{4}$ crossing angle. The length of the crossing was then stretched to match a 1 in 13 crossing angle that is installed on this site. Measurements of the crossing top shape were recorded but modelling the rail shape through measurements requires a complex pre-processing task that is out of the scope of this work.

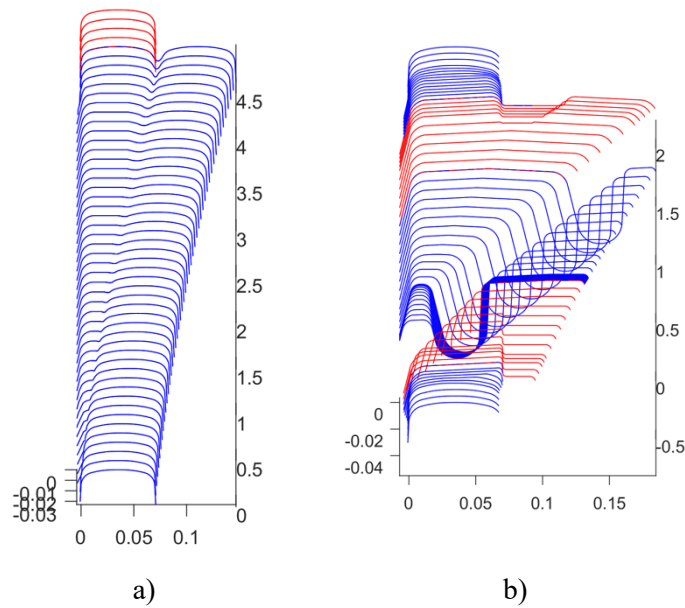


Figure 4.7. 56E1 Rail profiles for: a) CV Switch and b) Full cant crossing 1 in 9.25 [21, 97]

4.3 VI-RAIL CROSSOVER MODEL

4.3.1 Numerical model in VI-Rail

Figure 4.8 shows the railway crossover model built in VI-Rail, for which graphics have been created for rails and sleepers to better visualise the track model. The colour schemes used for the sleeper/bearers are: brown for sleepers G44 without USP; green for bearers with medium USP; and red for bearers with soft USP underneath. This is in agreement with Figure 4.3. Fewer bearers are considered in the Up line to reduce the size of the model, without compromising the accuracy of the model, as this simplification shows no influence on the contact forces predicted on the Down track.

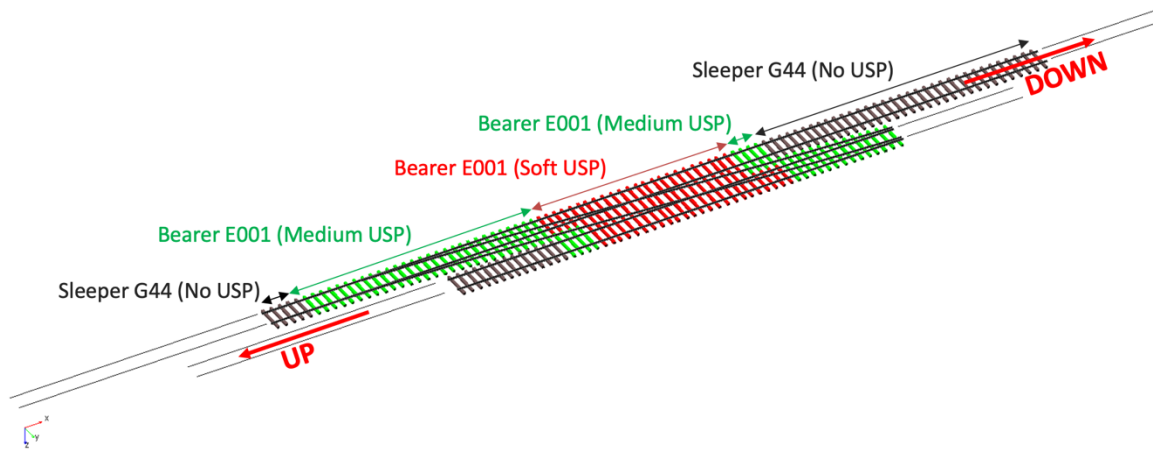


Figure 4.8. Full railway crossover modelled in VI-Rail

When building the full crossover model, the following key assumptions were made:

1. The switch blade is only considered when its head width is equal to the stock rail head width (see Figure 4.9 a)). On the 6ft side of the track, where the switch blade is in contact with the stock rail, a linear increase in mass and inertia is considered up to the point where two separate rails are considered. On the cress side the switch blade is completely neglected;
2. The crossing was initially considered as being two stock rails that were rigidly connected for vertical movements, as shown in Figure 4.9 b). This assumption was later corrected in chapter 5, using the crossing properties shown in section 4.2.1;
3. The long bearers and their connection were both modelled as rigid.

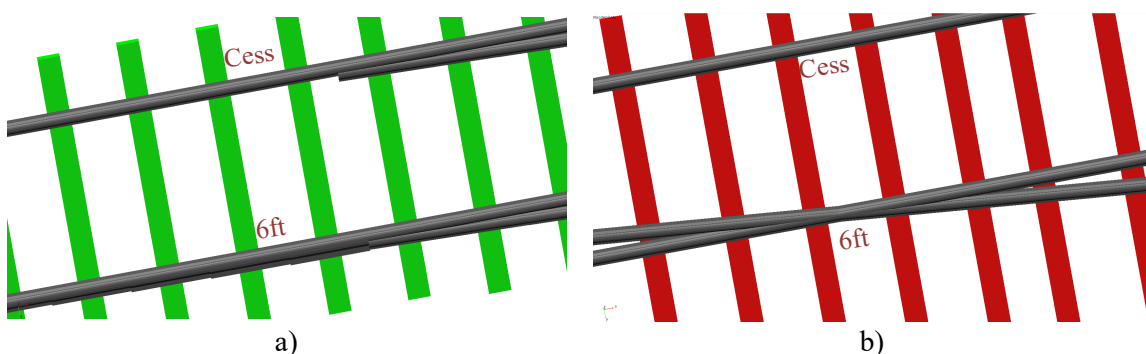


Figure 4.9. Detailed view from: a) Switch and b) crossing

4.3.2 Track irregularities (TRC data)

The rail top level variation or track irregularities are measured by the Track Recording Coach (TRC) in loaded condition. The instrumented vehicle that periodically runs along the whole network to acquire and process the main track characteristics. This vehicle records not only the rail top level but also track alignment and gauge.

Figure 4.10 shows the data recorded from the TRC on the Down line for both rails on 29 of February of 2016. The data was recorded every 0.2 m. The data presented will be used in all the dynamic analyses performed with the VI-Rail model of the crossover.

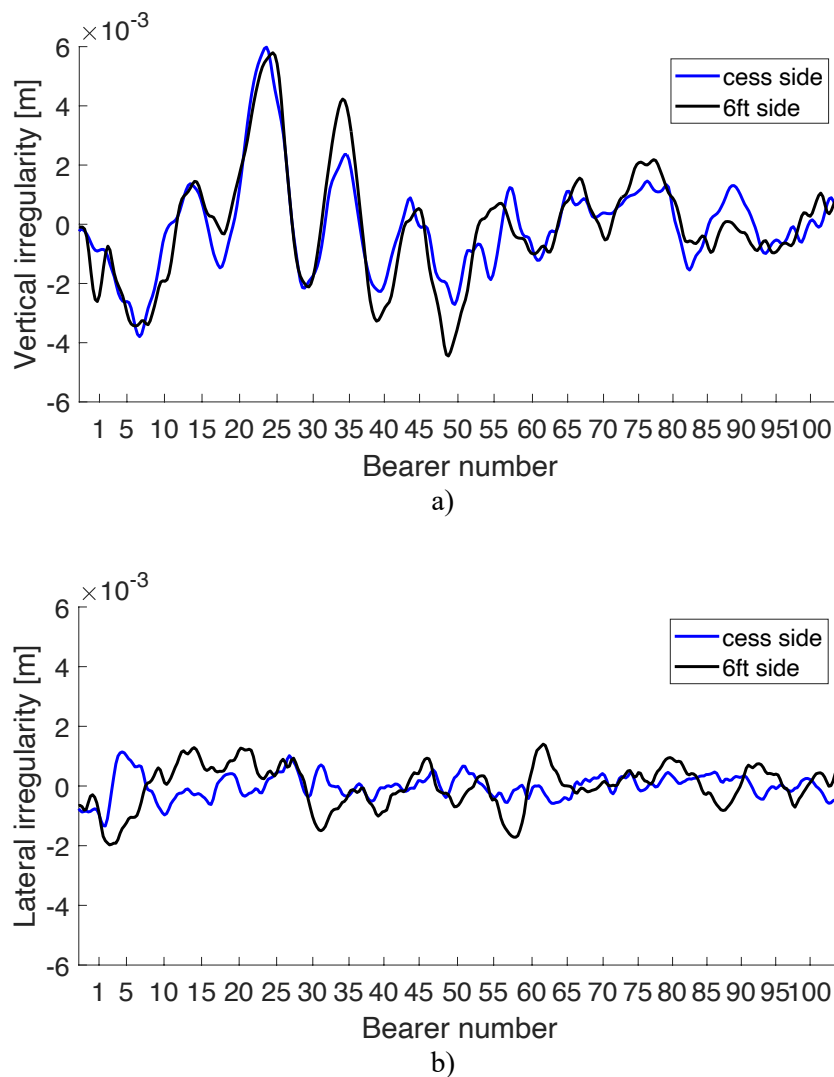


Figure 4.10. Track irregularities for both rails on: a) vertical and b) lateral planes.

4.4 LONG BEARERS FLEXIBILITY IN VI-RAIL

4.4.1 Hypothesis

In the next chapter, site measurements done in this site are explained and considerable bearer deflections were registered. These deflections, especially on the 6ft side cannot be achieved if the bearers are considered rigid. In this section, it is explained the methodology applied to consider the flexibility of the bearers that was later introduced in the model to be able to achieve good agreement with the measured bearer movements.

4.4.2 Methodology

The long bearers flexibility is modelled by a set of rigid bodies connected by massless Timoshenko beams (same modelling feature as used for the rail flexibility). The long bearers, which have been modelled as two connected rigid bodies so far, one for the bearer below the Down track and the other below the Up track, are now divided into 9 or 10 rigid bodies in total, depending on the position of the long bearer connection. The following requisites were taken into consideration to decide on the distribution length of each rigid bodies as shown in Figure 4.11 b) to d): each rigid body has a maximum length of half of the track base (i.e. half of 1.506 m); One rigid body must be defined below each of the rails on both through lines (Up and Down) to receive the vehicle input load. One rigid body is present at each bearer end, allowing to define support elements up to those positions. Figure 4.11 a) shows the rigid bearer modelled with four ballast reaction point below each of the Up and Down rails. Figure 4.11 b) to d) show the three configurations for semi-flexible bearer models. The first configuration (Figure 4.11 b)) is used between bearers number 38 and 49, the second configuration (Figure 4.11 c)) is used between bearer number 50 and 53, and finally, the last configuration (Figure 4.11 d)) is used for the remaining bearers, number 54 to 65. The trackbed stiffness reaction is distributed along the bearers at each rigid body centre of mass. In order to keep the number of variables low, each of the three configuration models (b to d) use the same four stiffnesses defined for the reference model (a).

As for the rails, the full bearer mass is distributed to each individual to each rigid body elements at its centre of mass, highlighted in figure 4.10 with a red star (*). Massless beams elements are used to connect the adjacent rigid bodies at their centre of mass. The beam cross-section was assumed equal to 0.2 m x 0.2 m and the Young's modulus adopted as 30

GPa. All three beam inertias were considered equal to $0.20^4/12$ (square section inertia). The shear area ratio adopted was $6/5$, as suggested in Adams help file [81] for a solid rectangular. The shear modulus is obtained as a function of the Young's modulus and Poisson ratio, same as for the rail beams in section 4.2.1.

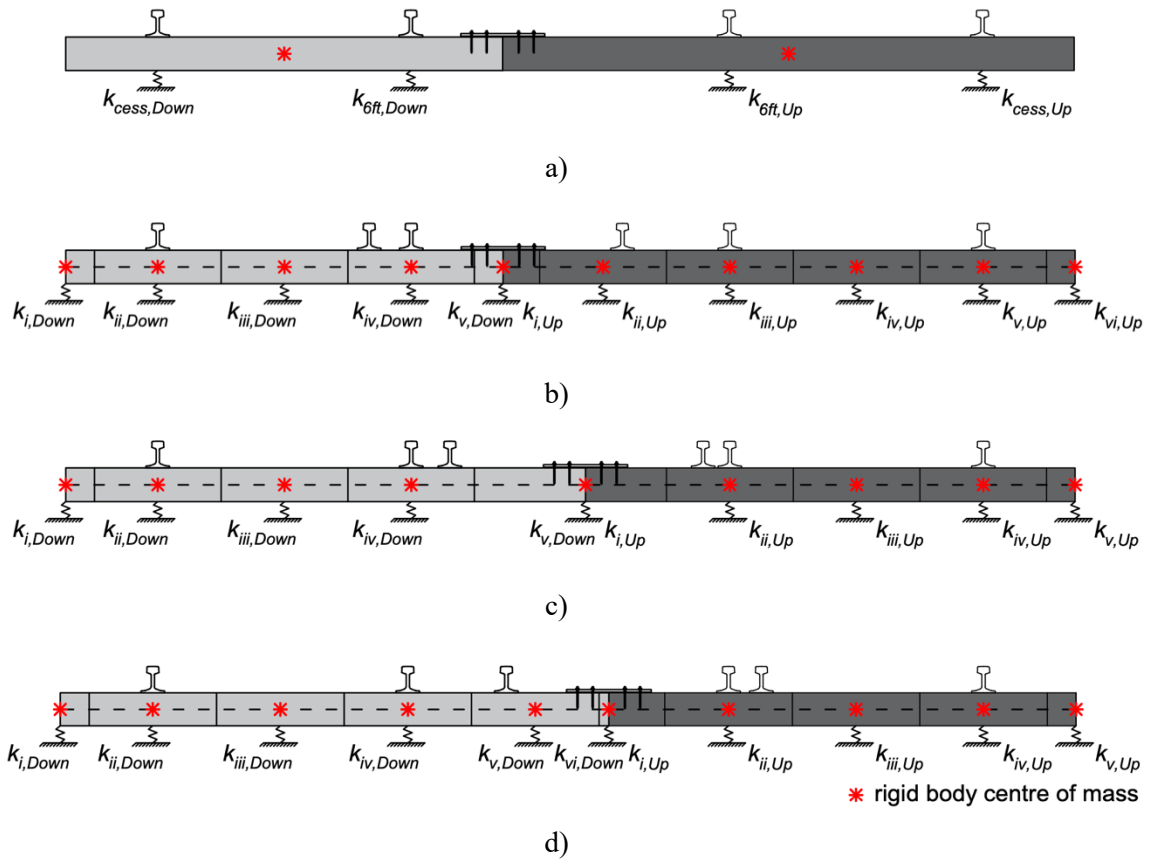


Figure 4.11. Long bearer model: a) rigid, b) semi-flexible type 1 (bearer 38 to 49) , c) semi-flexible type 2 (bearer 50 to 53) and d) semi-flexible type 3 (bearer 54 to 65)

4.4.3 Validation against ANSYS

To validate the modelling approach developed in VI-Rail, a Finite element model built in ANSYS is used as a comparison. One bearer is selected for this comparison and a modal analysis is performed in both VI-Rail and ANSYS software. Finally, the static load of the vehicle is applied on both rails from the Down track and bearer displacements are compared.

Bearer number 38, the first long bearer encountered when travelling in the Down through route, is selected for the comparison analysis. This bearer is represented by the model shown in Figure 4.11 b) that comprises 10 rigid bodies. Figure 4.12 shows three models, namely: a) VI-Rail using rigid bearers with four support locations; b) VI-Rail considering semi-flexible bearer and support below each rigid body and c) ANSYS with a flexible bearer and

distributed support. To keep the model simpler, only a section of 0.71 m of the rails from Down through route is considered.

The ANSYS model uses MASS21 elements to model the rail masses, BEAM188 elements to model the bearer and COMBIN14 to model both the rail-pads and the trackbed support. The rail mass was assumed as 39.973 kg (linear mass of a 56E1 rail multiplied by 0.71 m spacing) and the rail-pad parameters are the same as presented in Table 2.1. The long bearer was modelled with a cubic two-node Timoshenko beam, with a square cross-section of 0.2 x 0.2m and 3000 kg/m of density (this value was adopted instead of the standard concrete density of 2890 kg/m to take into consideration the additional mass from the fastening). A mesh of 25 mm size was adopted for the beams of the bearer. The trackbed stiffness was distributed using springs below each of the bearer nodes.

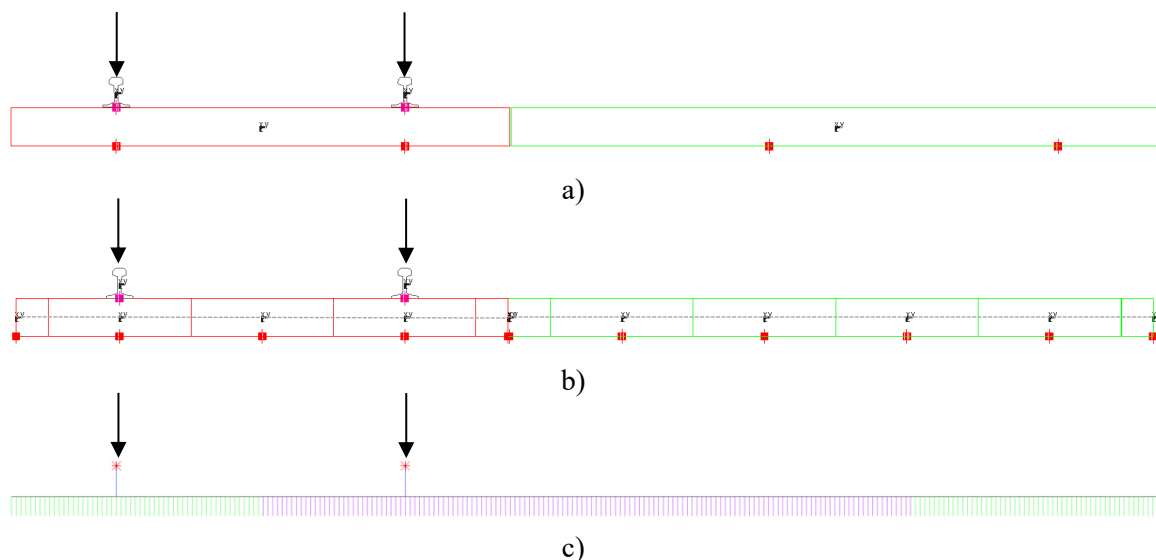


Figure 4.12. Long bearer model comparison: a) VI-Rail rigid model, b) VI-Rail semi-flexible model and c) ANSYS flexible model

The trackbed stiffness is set equal to 40 kN/mm below each rail on both tracks as shown in Figure 4.12 a) for the rigid bearer model. The springs from the cess side of each track have a 1.3 m length distribution and the two middle springs the remaining 3.4 m. This is equivalent to 30.77 kN/mm and 25.53 kN/mm per meter length, as shown in Figure 4.13. Although the positioning of the supports under the rails makes the support not constant along the bearer, it allows considering different stiffness values under the 6ft and the cess sides which are distributed along the two areas mentioned above with 1.3 and 3.4 m.

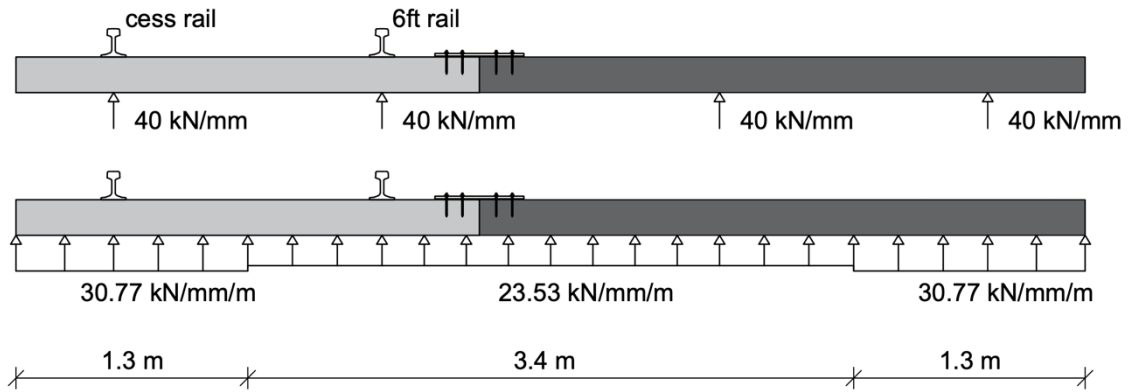


Figure 4.13. Long bearer support distribution

For the semi-flexible model in VI-Rail, the vertical stiffness below each rigid body is given by the relation between the element length and the distributed stiffness, shown in Figure 4.13. A preload is considered for each bushing element, which accounts for the mass of the bearer element and for the mass of the rail where a rail exists above the bearer element. The rotational stiffness K_{TX} in kNm/rad is calculated as a function of K_v in kN/mm and the length of the sleeper element Δl , as shown in Equation (4.6).

$$K_{TX} = \frac{1}{4} \times \Delta l \times K_v \quad (4.6)$$

A modal analysis is performed to compare the vertical mode shapes obtained from VI-Rail and ANSYS. Figure 4.14 shows the mode shapes below 100 Hz, for which a good agreement is observed with differences lower than 4 %. The aim of this work is mainly to look at forces transmitted to the connection and to the sleeper, which are in the range of few hundreds of Hz. It is therefore important to have a good match between the global modes of the two models under 100 Hz.

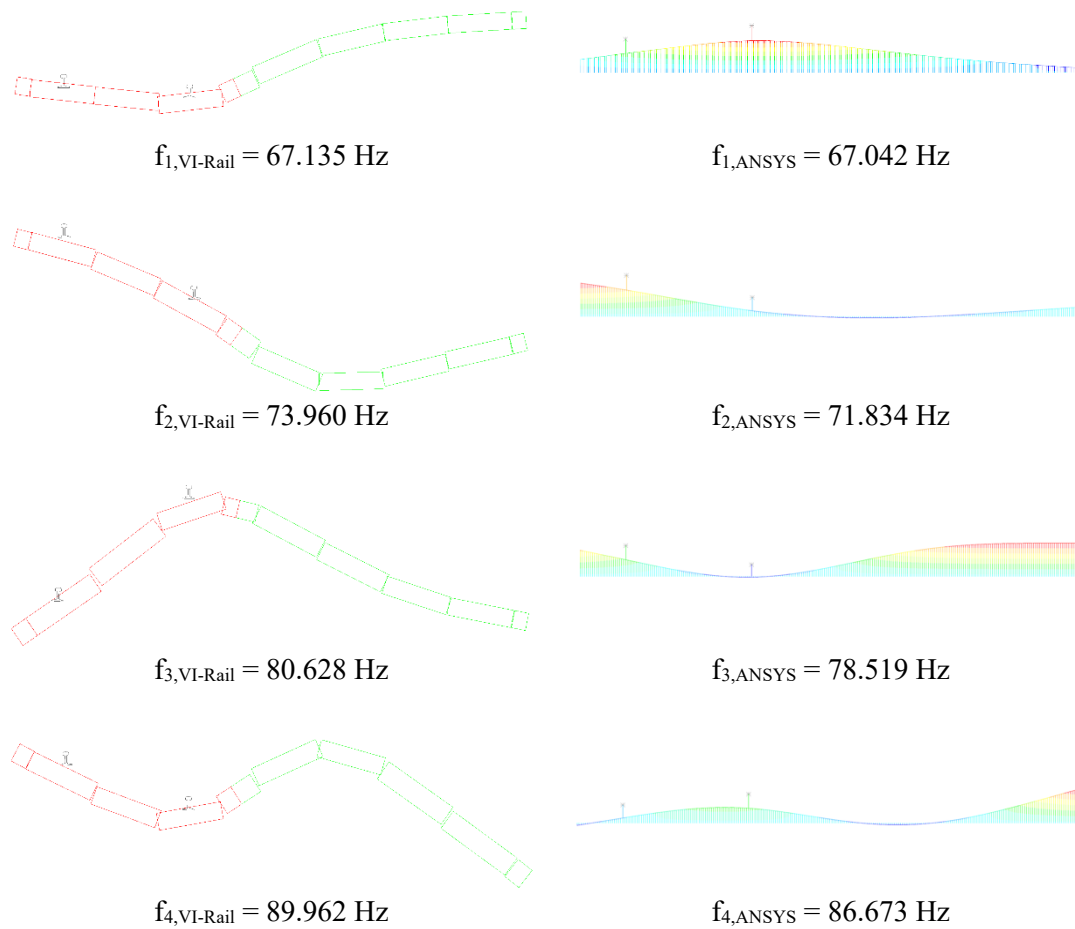


Figure 4.14. Long bearer vertical bending modes for frequencies below 100Hz

Figure 4.15 shows the vertical bending modes for frequencies above 100 Hz where a higher discrepancy is observed, reaching 30 % of difference for the 8th modal frequency. The accuracy could be improved by increasing the number of rigid bodies of the bearer, however, this would increase the computational cost of VI-Rail model.

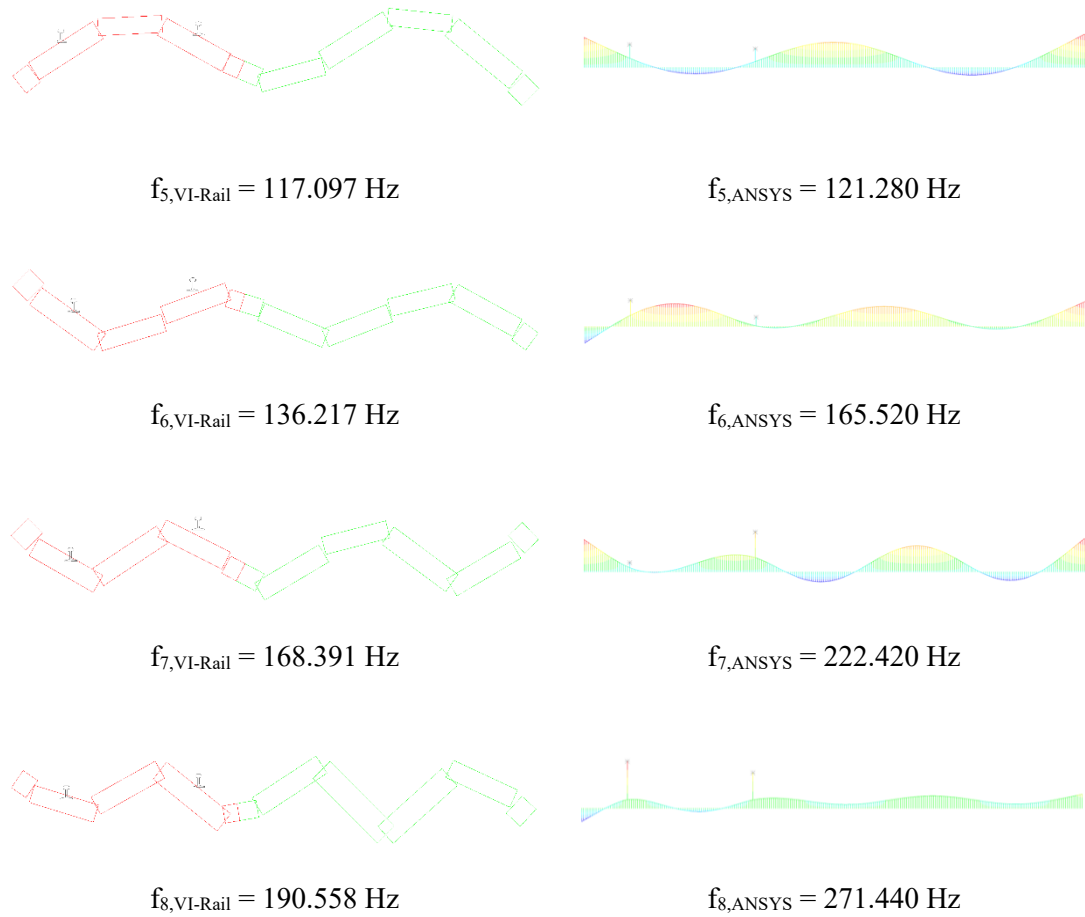


Figure 4.15. Long bearer vertical bending modes for frequencies above 100Hz

Alternatively, a static analysis is performed to observe the bearer deformation when subjected to nominal loads while validating the VI-Rail track model against ANSYS. A force of 5.7 tons is applied on top of each rail element to compare the bearer displacements of the three models shown in Figure 4.12. In VI-Rail, a STEP function was used to get a smooth increase of the force from zero to full value in 0.1 s. Figure 4.16 shows the displacements observed for the 5.7 ton and obtained for the three models with the support stiffness distribution presented in Figure 4.13. A good agreement is obtained between the VI-Rail semi-flexible model and the ANSYS model. The rigid bearer however shows considerable differences, mainly below the 6ft rail (located at 0.753 m) and the 4 ft (between tracks). Note that, in the case of VI-Rail semi-flexible model, the displacements are obtained for the rigid bearer centre of mass positions (see Figure 4.12 b)). A line was used to connect those points, making the results easier to compare, but it does not represent the real displacements between points. To get the real values, the beam shape functions had to be used.

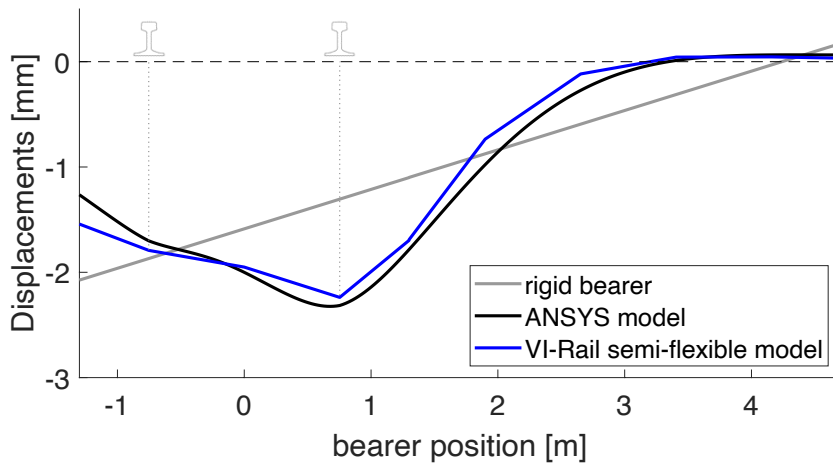


Figure 4.16. Long bearer displacements considering constant support stiffness

4.5 DISCUSSION

In this chapter, the detailed modelling approach of a complete crossover developed in the VI-Rail software and using the discretely supported track model selected from the previous chapter. A detailed description of a UK site considered and all the parameters adopted for the numerical model is given. The model considers the two adjacent Up and Down routes, as well as the diverging route so that the complexity of the layout can be understood. A particular focus is given to the Down through route (Down from London) since most of the site measurements available were taken in this route and the model will later be applied in this direction for dynamic simulations.

A semi-flexible model for the longer bearers is introduced in VI-Rail and compared with a FE model in ANSYS. The model approach in MBS shows a good match with the FE results for frequencies up to 100 Hz and up to 30 % difference for frequencies up to 200 Hz. In terms of bearer displacements, both models show a good agreement. This semi-flexible model was introduced to improve the bearer displacements predictions obtained from the purely rigid bearers approach, initially considered. The results presented in this chapter show that using rigid bearers presents serious limitations both for quasi-static and for dynamics studies. These limitations will be important in the following chapters where the semi-flexible modelling approach needs to be considered.

The parametric definition of the crossover model shows a great potential to be calibrated against site measurement. The next chapter will therefore focus on the site measurements

available, which can be used to calibrate the model behaviour and improve certain areas of the model such as the support stiffness of the bearers or the possible elements which may not be working as intended.

5 CALIBRATION OF THE RAILWAY CROSSOVER MODEL

In this chapter, the numerical model proposed in chapter 4 is calibrated to reach a good agreement with the site measurements obtained from two campaigns performed in the same UK site by the University of Southampton (UoS) and the University of Huddersfield (UoH) in 2016 and 2019. Therefore, two calibrations are performed, one for each campaign. The first calibration was a collaborative work that led to the work published [5] This chapter includes: 1) a description of the site measurements, ii) model adjustments that take into account the track degradations, such as, voids, and iii) the calibration methodology. The trackbed stiffness from the numerical model in chapter 4 is calibrated to match the bearer displacements measured in both campaigns. The first campaign only captured a limited number of bearers in two areas of the site, while the second campaign captured all bearers over an extensive length of track. A second calibration has been performed as the track condition has changed significantly leading to greater bearer deflections when compared to the first campaign. The adjustment of the trackbed stiffness was no longer enough to reach such deflections, therefore, modifications of the track model have been applied to account for the degradation on some components of the track, such as the broken connections between bearers and voids on the ballast. Finally, the results obtained show a good match between the numerical model and the site measurements, which validates the proposed track models, and some conclusions and assumptions were made regarding the degradation state of the crossover for the 3 years that separate the two campaigns.

5.1 MODEL CALIBRATION FOR THE FIRST CAMPAIGN

5.1.1 Site measurements description

The first campaign was carried out over the course of a few days in March 2016 and monitored five zones, as shown in Figure 5.1 [91]. Geophones were used to measure bearer/sleeper movements, as a common practice from other works [13, 98-102]. Geophones are usually attached to small metal brackets glued temporarily to the bearers and wired to a data logger to record bearer movement velocities during train passage.

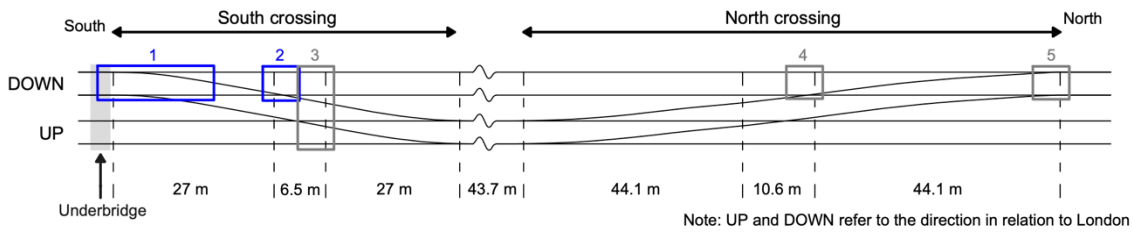
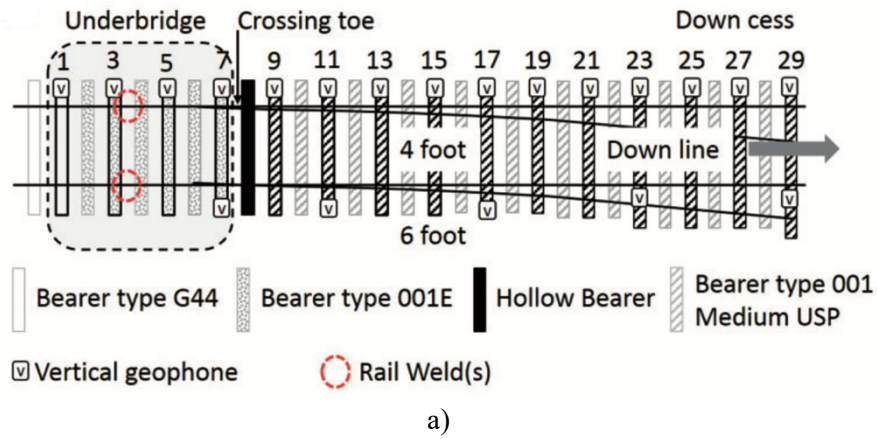
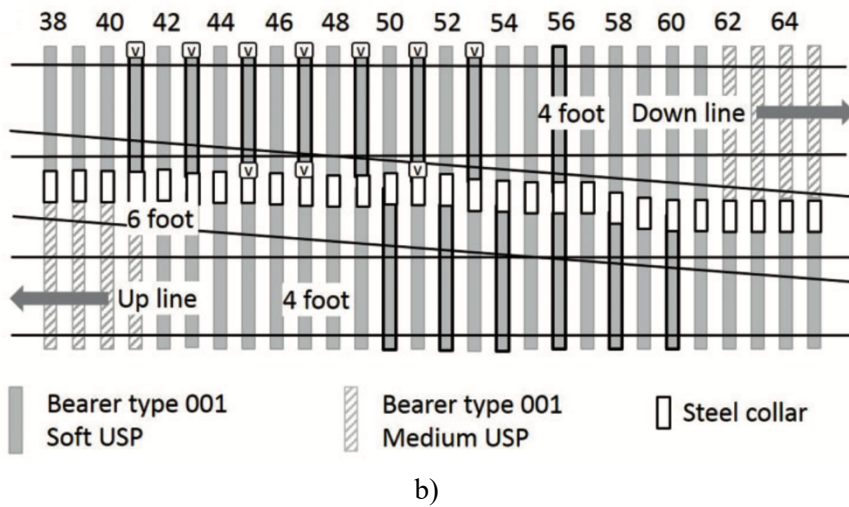


Figure 5.1. Locations monitored on the UK site (adapted from [91]).



a)



b)

Figure 5.2. Monitored locations at a) zone 1 at the switch panel and b) zone 2 at the crossing panel [5].

The focus of this work is on the first crossing, identified in Figure 5.1, with trains running on the Down line (from left to right). Therefore, only measurements from zones 1 and 2, as indicated in Figure 4.3, are considered. These two zones correspond to the switch and crossing panels, respectively. A total of 30 bearer locations were monitored, using 20 vertically oriented geophones and two data loggers, moved between locations to cover the

entire area monitored. The data acquisition system has an acquisition rate of 500 Hz and the loggers have 10 channels [101]. Instrumentation location plans are shown in Figure 4.3.

The model calibration performed in this work intends to reach a good match with the range of displacements of the bearers. These are obtained through the time integration of the velocities measured with the geophones. The sensors start recording automatically with the initial excitation of the approaching vehicle, which leads to significant transient effects on the leading and trailing bogies. From the different vehicle types and train configurations monitored, a Class 91 locomotive hauling nine Mark IV coaches and a Driving Van Trailer (DVT) is selected. Figure 5.3 shows the deflection of the 3rd bearer on the cess side, in which a low pass filter with a cut-off frequency of 1.5 Hz is applied. A repeated pattern of loading and deflection is observed for the nine Mark IV coaches, that is all cars between the first and last car, which can be used to estimate the at-rest sleeper position. The Mark IV coach in the middle, that is, the 5th coach, is selected for the calibration.

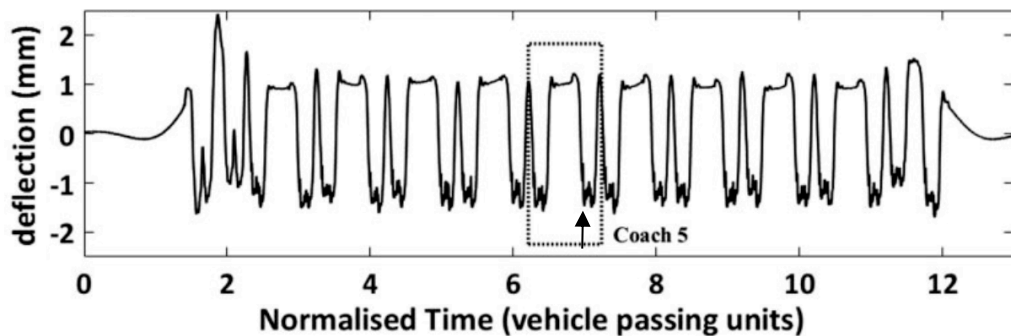


Figure 5.3. Deflection time trace for a Class 91 locomotive hauling nine Mark IV coaches and one DVT (adapted from [5]).

Figure 5.4 shows the measured peak to trough bearer movements as the third axle of the 5th Mark IV coach passes (pointed with an arrow in Figure 5.3). Vertical displacements between 0.5 and 2 mm indicate a good performance of the track [103], while displacements higher than 2 mm may indicate poor support conditions, due either to very soft subgrade or to voids in the ballast below the sleeper/bearer [103].

All bearers before bearer 9 rest directly on top of the ballast. These bearers show an average displacement around 1 mm with exception of the 3rd bearer that exceeds 2.5 mm suggesting that the bearer is voided. The void may result from the change of support conditions in the area of the underbridge or its deterioration with time, the presence of a weld and the twisted rail changing the inclination of the rail to vertical.

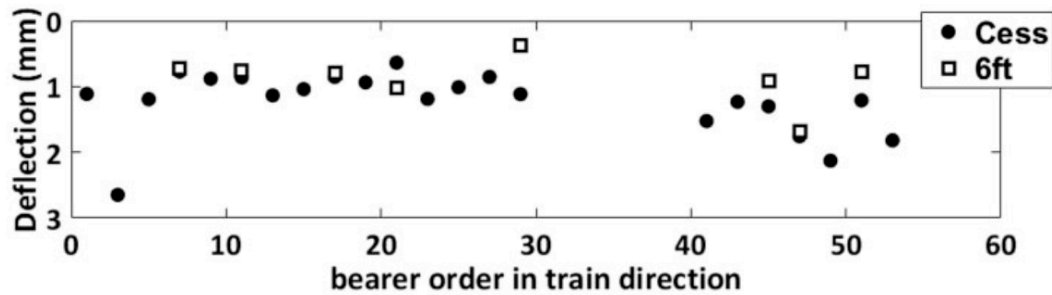


Figure 5.4. Bearer movements for the third axle of the fifth Mark IV coach [5].

Bearers 9 to 29, with medium USPs installed show deflections around 1 mm with the exception for bearer 29 on the 6ft side, moving only about 0.3 mm. This could be explained by the increased length of these bearers compared with the previous ones. Bearers 41 to 53, which have soft USPs installed underneath, are long bearers formed by two shorter bearers rigidly fixed, thus tying the two tracks together. These bearers show higher movements than the previous ones with greater variability, possibly due to being close to the crossing nose and subjected to higher dynamic loading effects. Displacements measured on the 6ft side of the bearers near the crossing show less deflection than on the cess side of the same bearer.

5.1.2 Assumptions from the numerical model used

The calibration for the first campaign is published in [5] and only summarized here. The model used was the same explained in Chapter 4.3 without the bearer flexibility and the varying rail properties on the crossing. The crossing element was approximated using two intersecting plain line rails, instead of the real properties. The bearer movements from 1st campaign on the crossing panel were quite consistent between 1 and 2 mm, which did not justify at the time, the inclusion of the bearer flexibility. Also, low degradation was observed in the crossover, with only one voided bearer at the beginning of the crossover. In [5], the rail-pad stiffness is 70 kN/mm instead of the 120 kN/mm presented in Table 4.3.

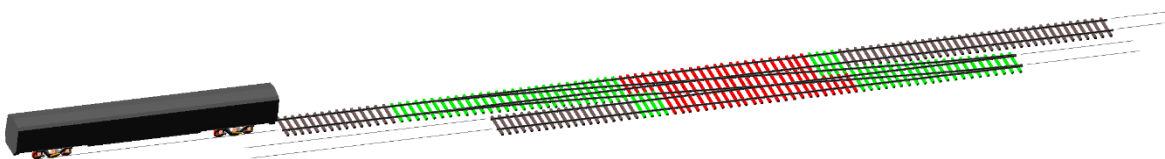


Figure 5.5. Mark IV coach and crossover assembly in VI-Rail.

The simplifications of the VI-Rail model stated previously made the model closer to VTI model and enabled using the simplified VTI model [65] to perform the calibration, which is convenient as both the model and employed calibration method are implemented in MATLAB. It is highlighted that the VI-Rail model is built based on the installation plan where the position and width of the bearers are considered, while the VTI model considers the bearers equally spaced and with only variable mass concentrated always at the centre between two rails. The difference between the two models is significant in the crossing panel with the long bearers connecting the two tracks. In VTI, an equivalent roll spring was used to replicate the roll resistance of connected long bearers with the Up line. The roll stiffness values are obtained by the product of the two vertical support stiffness underneath the Up line and the distance from each support to the end of the connection, as shown in Figure 5.6. Nevertheless, using the VTI model is less time consuming and this calibration leads to good parameters for the VI-Rail model enabling a reasonable match with the experimental results.

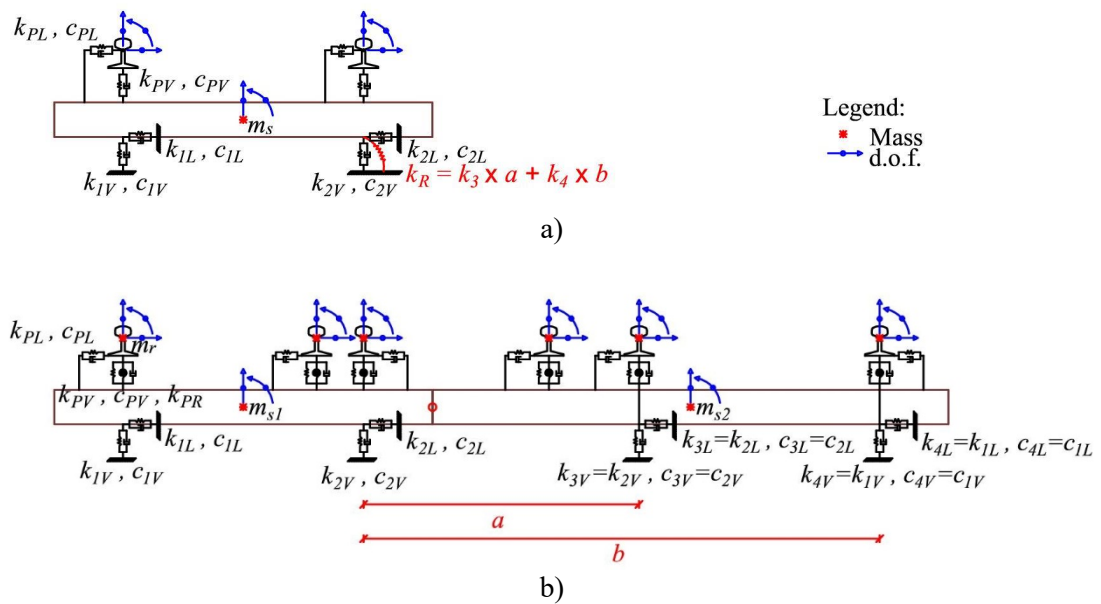


Figure 5.6. Transversal cross-section of a long bearer in (a) VTI model and (b) VI-Rail [5].

5.1.3 Model calibration

The calibration of the model considered for the first campaign consists of running simulations of the Mark IV coach negotiating the turnout in the through direction and the maximum displacement of the bearers are obtained to compare with the measured ones. First, the VTI software is integrated into an iterative process that calibrates the track stiffness to

reach a good match against the experimental data. Then, the calibrated stiffness values are used in VI-Rail, where the same scenario is tested, that is, the Mark IV coach negotiating the turnout. The vehicle in VTI is simplified, where only two-axle are considered with the respective primary and secondary suspensions and the equivalent mass of the bogie and car body on top of each. No interaction between axles is considered. VI-Rail has the full Mark IV coach modelled. The switch and crossing elements are implemented in VTI as a vertical irregularity which can be obtained from VI-Rail running the vehicle slowly and extract the wheel vertical movement. Note that VTI only considers the vertical dynamics. VI-Rail uses the as-new switch and crossing profiles for the contact and includes both vertical and lateral dynamics via the wheel-rail contact coupling algorithm [52, 54].

The vertical stiffness of the trackbed is calibrated through an iterative process, that is schematically described in Figure 5.7. Initial values are given to trackbed stiffness according to the values found in [5]. The dynamic analysis using VTI model is performed and the bearer displacements are calculated. The $error_i$ is the differences between the numerical and measured displacements in percentage. At each step, the average error for all bearers ($fValue$) is obtained and compared with a limit value ε . If the average error is higher than the stopping criteria, new values of trackbed stiffness ($k_{k,i+1}$) are calculated from the previous values of the current step ($k_{k,i}$). For each bearer, the value of the trackbed stiffness underneath is increased or decreased depending if the error between displacements is positive or negative.

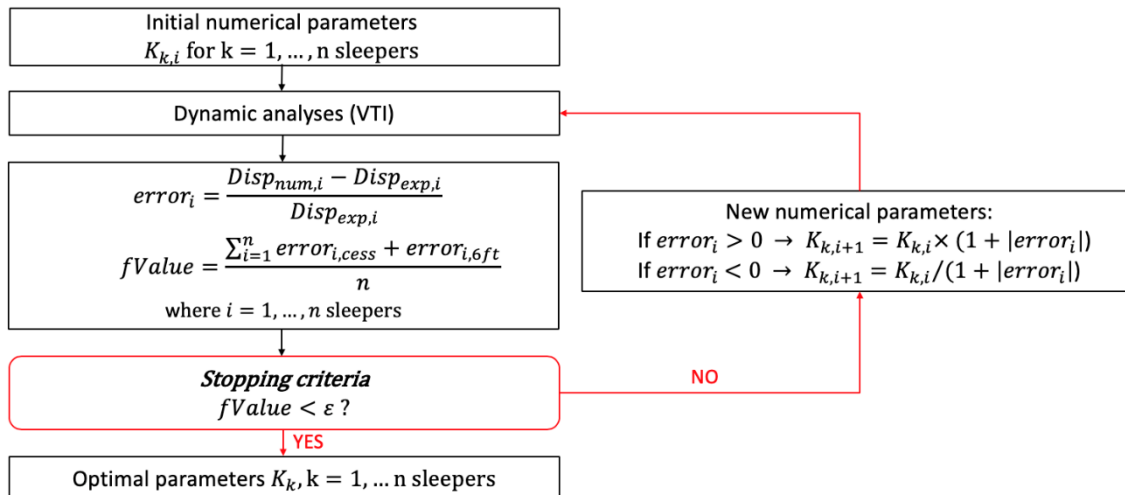


Figure 5.7. Iterative process to tune the trackbed stiffness.

Site measurements are available for every two bearers on the cess side and only a couple of bearers on the 6ft side, as shown in Figure 4.3. For the non-measured bearers, an average

value of trackbed stiffness of the adjacent measured bearers is adopted. In the switch panel, only the cess side is calibrated and the resulting trackbed stiffness values are applied on the 6ft, since there were not enough bearers on the 6ft side to actually perform a good calibration. In the crossing panel, however, both cess and 6ft sides are calibrated. Here also, only a few bearers were instrumented on the 6ft side and where not measured, the same value was assumed on both sides.

The differences between the numerical and experimental results are continuously reduced as shown in Figure 5.7 until the limit value ε is reached, which is assumed to be a sufficient match. The results from the calibration are shown in Table 2.1, which lists percentage differences between the measured and the VTI simulated deflections (ΔDisp) and trackbed stiffnesses (K_b), which are given by sleeper end (se). The differences on the 6ft side are higher than the differences on the cess side in the switch panel as expected, since only the cess side was considered on the calibration procedure. On the crossing panel, the differences are much lower and consistent. The average stiffness on the switch panel, excluding the voided bearer number 3 is 21.12 kN/mm per sleeper end, while on the crossing is 22.9 kN/mm/se and 19.9 kN/mm/se for the cess and 6ft sides, respectively. This is actually interesting, since a softer USP is installed on the crossing panel, which would lead to a softer trackbed stiffness than on the switch panel. The increase of stiffness could be related to the incapability of VTI model to consider the effect of having a second track.

Table 5.1. Final differences and trackbed stiffness values from calibration 1 [5].

Panel	Bearer	cess side			6ft side		
		Disp diff (%)		K _b (kN/mm/se)	Disp diff (%)		K _b (kN/mm/se)
		VTI	VI-Rail		VTI	VI-Rail	
Switch	1	-1.3	-8.2	20.3	-	-	20.3
	3	-19.8	-16.2	3.6	-	-	3.6
	5	-0.5	17.0	16.5	-	-	16.5
	7	1.1	10.8	27.4	14.8	23.9	27.4
	9	-1.4	11.7	24.2	-	-	24.2
	11	1.6	1.2	27.6	26.2	32.4	27.6
	13	-6.4	10.7	13.6	-	-	13.6
	15	-3	27.0	14.8	-	-	14.8
	17	2.8	7.2	25	38	22.5	25
	19	-9.5	-18.0	19.6	-	-	19.6
	21	17.1	-6.1	39	-	-	39
	23	16.1	11.0	10.9	0.9	5.2	10.9
	25	-1	20.9	16.1	-	-	16.1
27	-	-	27.9	-	-	27.9	
29	-6	5.7	12.9	193.5	137.9	12.9	
Crossing	43	3.2	-12.3	23.1	-	-	28.1
	45	5.8	8.6	21.1	3.4	1.6	28.1
	47	1.3	-11.8	18.2	4.2	34.5	13.8
	49	1.2	-25.4	20.4	-	-	6.4
	51	10.3	-14.5	44.8	1.5	9.7	26.6
	53	1.1	17.1	9.8	-	-	16.6

Figure 5.8 shows both simulated and measured bearer displacements along the switch panel. A good agreement between the measured data and both models is observed, with the exception of bearer number 3 on the cess side and bearer 29 on the 6ft. A small trackbed stiffness is considered for bearer 3, which leads to the high measured displacements. Higher differences can be seen on the 6 ft side, Figure 5.8 b). These differences are acceptable since only the trackbed stiffness on the cess side was tuned and considered equal to the other side. Bearer number 29 shows higher displacements on the cess side than 6ft side and that difference is not considered on the trackbed stiffness.

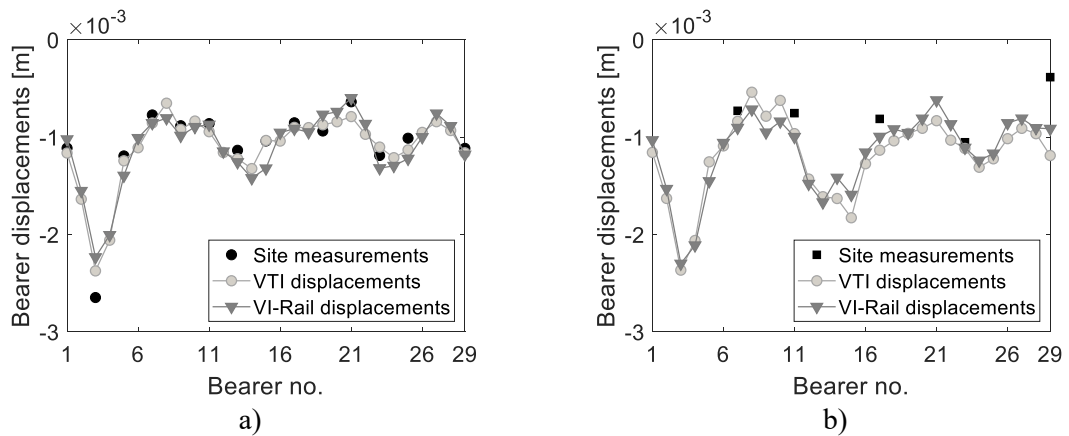


Figure 5.8. Bearer displacements along the switch panel: a) on the cess side; b) on 6ft side.

Figure 5.9 shows the vertical contact forces along the switch panel for both sides. A good agreement is achieved between the two models. The soft spot of bearer 3, located five bearers before the switch toe creates a dynamic load amplification that is apparent between bearer 3 and 11 on both sides. This behaviour is less noticeable from the VI-Rail model which shows similar variability on the contact forces even after the switch, i.e. after bearer 22. Higher transient contact force is observed in the 6ft side, where the wheel load is transferred from the stock to the switch rails, namely, between bearers 11 and 17. These higher contact forces are also responsible for the significant variation in vertical displacements.

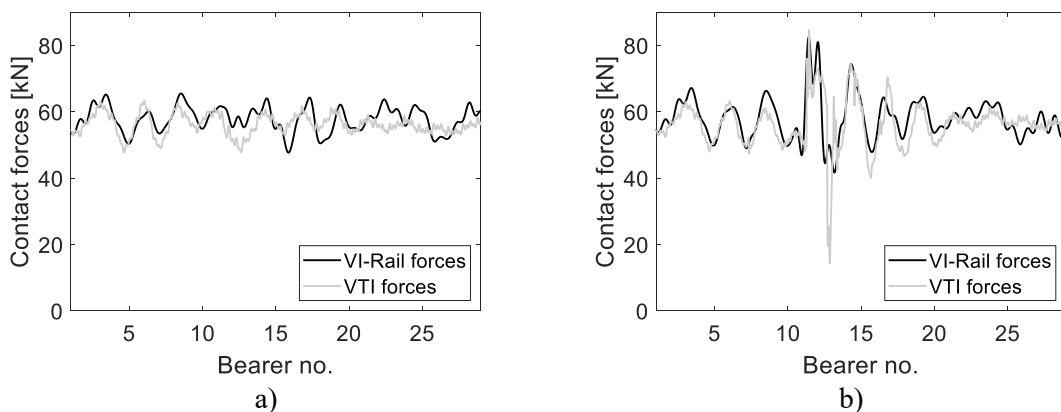


Figure 5.9. Vertical contact forces along the switch panel: a) on the cess side; b) on 6ft side.

Figure 5.10 shows both simulated and measured bearer displacements along the crossing panel. Generally, deflections on the 6ft are smaller when comparing with the cess side, except for bearer 47, which is under the crossing nose.

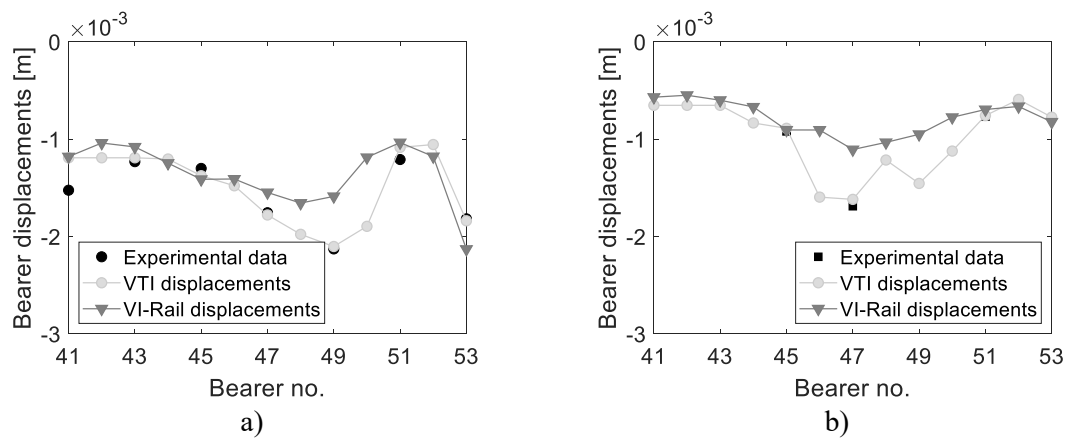


Figure 5.10. Bearer displacements along the crossing panel: a) on the cess side; b) on 6ft side.

The simulations with VTI show a good agreement with the measured displacements since the trackbed stiffness was calibrated to this model, while VI-Rail model shows considerable differences in the area of the crossing panel. Although the two models are similar in the switch panel with the same assumptions, VI-Rail shows a stiffer track reaction in the crossing panel. VI-Rail considers the two tracks with the rigid bearer connection, while VTI has an additional rotational stiffness on the 6ft side as shown in Figure 5.6 to increase stiffness on that area to capture the effect of the second track. From the results shown in Figure 5.10, this rotational stiffness does not represent the complete increase in vertical stiffness and both models give different results.

Figure 5.11 shows the vertical contact forces along the crossing panel for both sides. VI-Rail uses the crossing profiles as new, while VTI considers a vertical irregularity to simulate the wheel facing move on the crossing. Since VI-Rail has the detailed model of Mark IV coach running on the track, there is visible dynamic amplification on the cess side that is not visible on the VTI output because it uses simplified independent moving masses on top of each rail. On the 6ft side, three peaks are observed on the contact forciers obtained with VI-Rail, which are the wheel rolling over the wing rail, the wheel impacting the crossing nose and finally the wheel leaving the crossing component. VTI only considers the irregularity at the area of the gap between rails and the contact on the crossing nose, showing only one peak. It also seems to capture better the P1 and P2 forces on the crossing nose (bearer 47) while VI-Rail has only a single peak. The differences between VI-Rail and VTI are due to the different composite stiffness of the track models and the assumptions considered in VI-

Rail which considers two stock rails rigidly connected instead of the variable rail properties from the crossing.

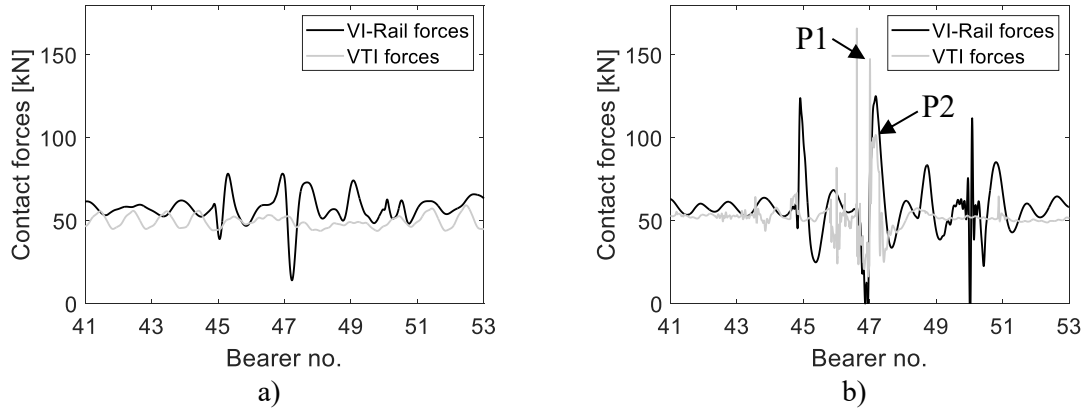


Figure 5.11. Vertical contact forces along the crossing panel: a) on the cress side; b) on 6ft side.

In summary, the two models show a good agreement on the displacements and contact forces on the switch panel and predictable disparities due to the differences from each model approach on the crossing panel. This exercise allowed to compare the two models and understand the limitations of each. Although the same calibration could be done using VI-Rail, by the time this work was done, the VTI was preferred as it was already developed in MATLAB. This work was not so interesting to re-visit at a later stage since the first campaign lacks in data and a lot of assumptions were made during the calibration to be able to guess the trackbed stiffness values for bearers not instrumented. For this reason, this work gives more emphasis to the second campaign explained next.

5.2 MODEL CALIBRATION FOR THE SECOND CAMPAIGN

5.2.1 Site measurement description

Only a few areas with a maximum of 20 geophones each, were considered in the previous campaign. These areas were selected since higher dynamic loads and consequently higher variability on trackbed support stiffness were expected due to the switch and crossing elements. Most measurements were taken on the cress side due to its easier access. Limiting the areas of measurement is a practical decision based on the availability and cost of equipment. With the lower cost transducers and data acquisition systems, e.g. MEMS sensors and microprocessors, a larger scale of sensors distribution is possible [104].

Therefore, three years later the second measurement campaign was performed on a larger scale. The same monitoring and surveying technique applied in [104] was considered. This technique allows to measure the level, dynamic deflection and stiffness of the track for a successive number of sleepers over a long extend of track but fails to S&Cs since a given axle load is assumed and it is not considered the dynamic amplification that happens on a turnout.

University of Southampton (UoS) carried out the 2nd campaign at the same site in 2019, 3 years after the 1st campaign. A wider area on both sides of the Down track and a smaller area around the crossing for the Up track were monitored. 80 Gulf Coast Data Concepts X16 micro-electro-mechanical-systems (MEMS) accelerometers were placed on both sides of the line and moved along to instrument the entire length of track. Each of these devices contains an ADXL 345 digital MEMS accelerometer, a microcontroller programmed as a data acquisition unit, a real time clock, a memory card and a battery [104]. The devices were programmed to record continuously at 400 Hz. Train passages were identified in the acceleration data, which was filtered and integrated twice to obtain displacements, using 4th order high and low pass Butterworth filters with cut on and cut off frequencies of 2 and 40 Hz, respectively [104].

The experimental results comprise the maximum deflections of 117 bearers of the Down line for both sides, cess and 6ft, and the maximum deflections of 30 bearers of the crossing panel of the Up line for both sides too. These results are shown in Figure 5.12. Comparing multiple locations and using a statistical process based on a cumulative distribution function, it is possible to identify the bearer resting position and its downward movement [105]. The average bearer deflections are obtained from several Class 91 train passages.

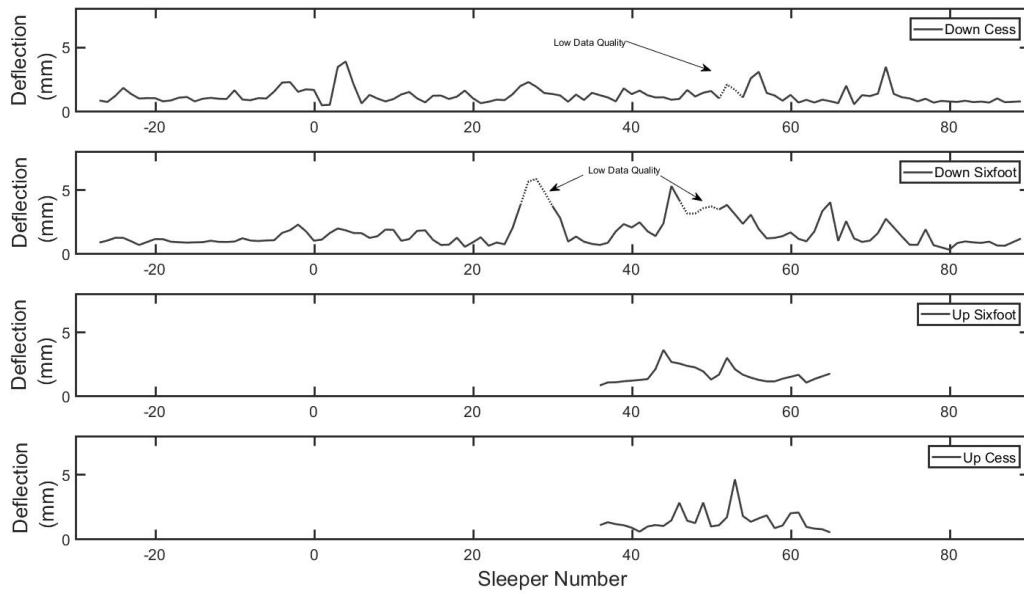


Figure 5.12. Average measured bearer deflections obtained from bearer vibration measurements collected from UoS.

Three main areas are identified with low data quality, one before the long bearers joining the two tracks, one after the crossing nose and one area on the cess side after the crossing where the check rail ends, as indicated in Figure 5.12. Low data quality here means saturation of the accelerometer, reaching its frequency limit or noise in the response after filtering.

A comparison between the first and second site measurements is observed in Figure 5.13 from which the track condition evolution can be analysed. On the switch panel (Figure 5.13 a)), the average difference between the two campaigns is around 32% bigger deflections for both sides, cess and 6ft. The average difference on the 6ft side excludes bearer 29, which shows an increase of 17 times more movement than the previous campaign. This bearer shows the opposite behaviour of the previous measurements, with higher displacements on the 6ft compared to the cess side. Looking at the pictures taken from the site, it is visible a rail weld around bearer 27, which coincides with this peak of deflections.

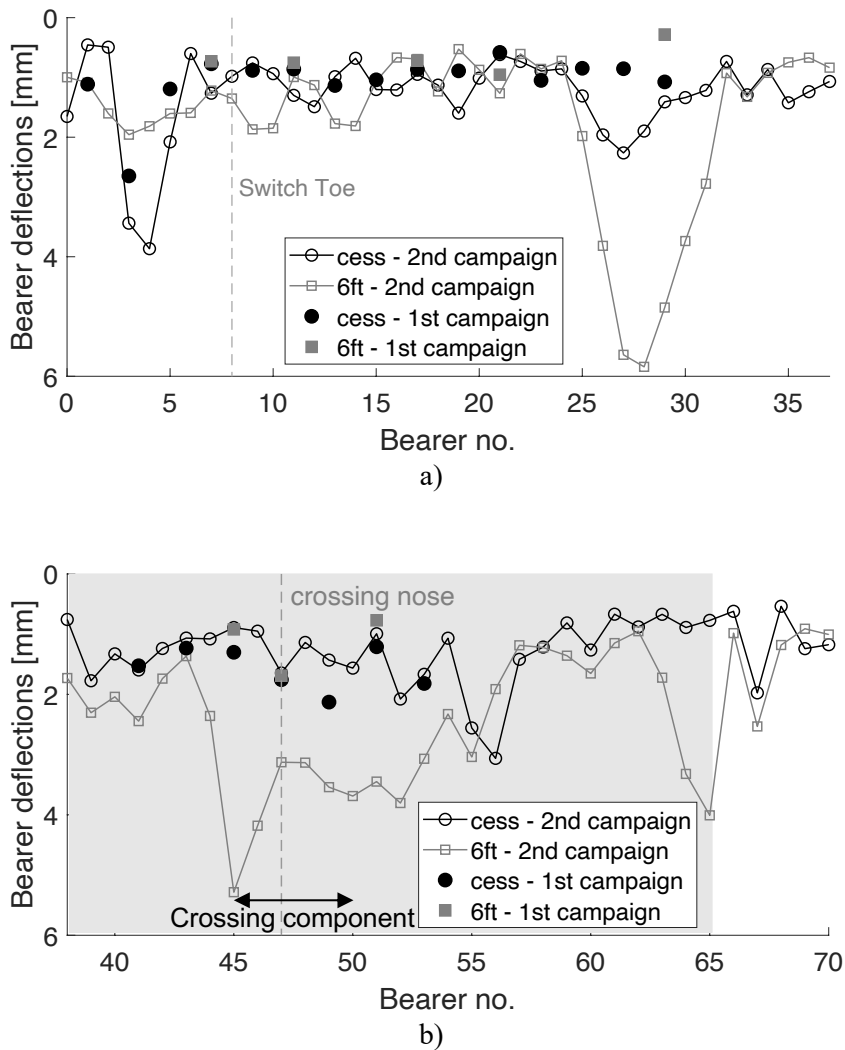


Figure 5.13. Comparison from bearer deflections of first and second campaigns for: a) switch panel; b) crossing panel.

Figure 5.13 b) shows the bearer deflections on the crossing panel. The area highlighted in grey represents the presence of longer bearers using the steel collar fixing both tracks. Comparing the two campaigns, the cess side shows an average difference of 15% less displacements, while the 6ft side shows an average growth of bearer movements of 302%. It is important to mention that only three bearers were instrumented on the first campaign on the 6ft side, which makes it difficult to assume the real state of all that area and compare it with the new measurements. Overall, looking at the displacements from the second measurements only, it is evident that bearers close to the crossing element deflect more on the 6ft side than on the cess side, which can be related to the high transient loads that are expected at the crossing nose. Bearer number 45 shows the highest deflections of around 5.3

mm. This coincides with the entry leg end of the crossing, which causes higher dynamic forces due to the change of profiles from nominal to wing rail shape.

The track condition can also be judged based on pictures taken during the site measurements, namely, loose bolts at the collars joining the bearer running under the leg end and under the crossing nose are observed, as shown in Figure 5.14 a) and Figure 5.14 b), respectively. In this area, high dynamic forces are applied on both casting and wheel, mainly the area where the wheel load shifts from the nominal rail to the wing rail of the crossing and from the wing rail to the crossing nose. Although visible damage on the top level of the crossing is identified, the simulations performed in this work consider the rail surface as-new design as the measured rail profiles were not available in time for this study.

Moving towards the end of the long bearers, a surprising behaviour is observed. An increase of bearer deflections was expected after the long bearers and not before they end. The last 4 long bearers, number 62 to 65, have medium stiffness USP and 3.4 m length, while the bearers after from plain line have no USP installed and are 2.4 m long. These last ones, because they are shorter than the longer bearers that are connecting both tracks, it was expected to have more movement. The fact we observe larger displacements in that area could be related to the traffic on the other track (Up), which move from a single track to the longer bearers. Photos from the site show loosening bolts around the crossing of the Up track at a similar relative location as observed from the down crossing.

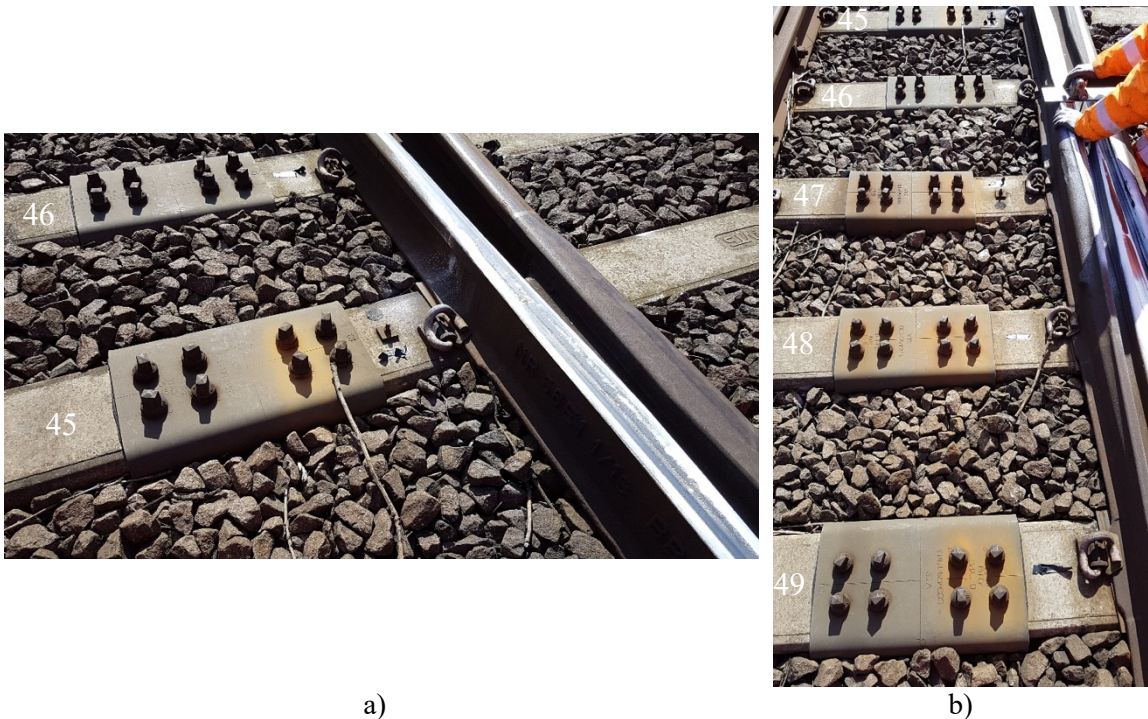


Figure 5.14. Site pictures from the second campaign (photos taken from UoH)

5.2.2 Adjustments of the crossover model

As the track condition indicates voided bearers and loose bolts in the bearer connections, adjustments of the crossover model proposed in chapter 4 have been considered to enable a good match with the experimental results. The required model modifications are presented hereafter.

The difference between displacements from cess and 6ft sides in the crossing panel requires considering the bearer flexibility, which was introduced in chapter 4. A single long bearer (number 38) was selected as an example and used to compare both the displacements from the rigid and flexible approaches. The results from the static analysis were presented in Figure 4.16, where a significant difference from the displacements below the rail on the 6ft was observed. This difference would make impossible to reach a good match with the new site measurements.

In chapter 4 and for the first calibration, only a linear bushing element was considered to represent the support of each bearer element, meaning that the reaction force is linear and depends on the relative motion between the sleeper and ballast. During the 2nd campaign, a lift-off behaviour of the bearers was observed when the train moves in one of the tracks,

lifting the far end of the other track. This behaviour needs to be properly modelled. Therefore, the linear bushing underneath the bearers is replaced by a *general force* element with non-linear properties, where linear force is observed for the downwards motion and no force for the upwards movement, as shown in Figure 5.15. Note that preload is accounted for to balance the weight of the masses supported by the general force elements, namely, the bearers and rails, which ensures the equilibrium in the vertical direction from the beginning of the dynamic simulation.

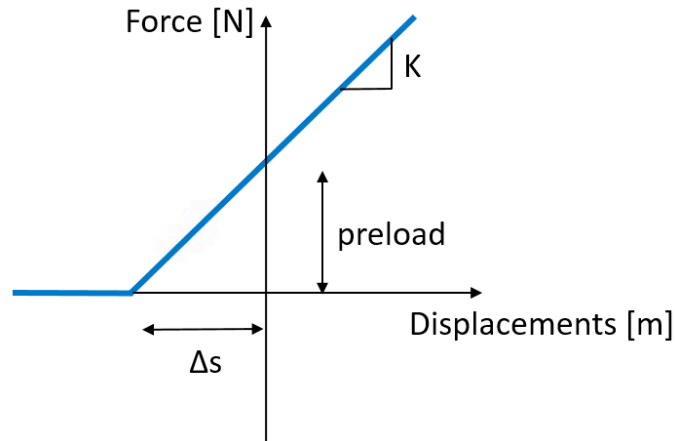


Figure 5.15. Non-linear bushing element characteristic with preload.

Δs corresponds to the distance that the spring has to move to create a certain force corresponding to the preload, to support the structure above, and that depends on the vertical stiffness K_z . The vertical force of the support element is given by the following equation:

$$F = \begin{cases} 0 & D_z + \Delta s \leq 0 \\ K_z \times (D_z + \Delta s) + C_z \times V_z & D_z + \Delta s > 0 \end{cases} \quad (5.1)$$

where F is the force, D_z is the bearer displacement, K_z the vertical stiffness, Δs the additional displacement from the preload, C_z the vertical damping and V_z the bearer velocity. In VI-Rail, a STEP function is used to implement the non-linear behaviour shown in Figure 5.15. When $D_z + \Delta s$ is lower than 0, there is no force and when it is equal or higher than 0.05 mm, the force is given by $K_z \times (D_z + \Delta s)$.

The same long bearer configuration presented in Figure 4.12 with a 5.7 ton force applied in both rails from the Down track and a support of 40 kN/mm/se is used to test the non-linear force element. Figure 5.16 shows a comparison between the new support element and the results obtained before with the linear bushing and rigid bearer. A good agreement is

obtained from the linear and non-linear supports when the element works in compression (negative values of displacement). With the non-linear support, correct behaviour is achieved on the opposite side of the track, where the bearer is expected to lift. Although the differences on the Down track where the measurements were made are not very big, these non-linear bushings were a preparation to consider possible voided bearers.

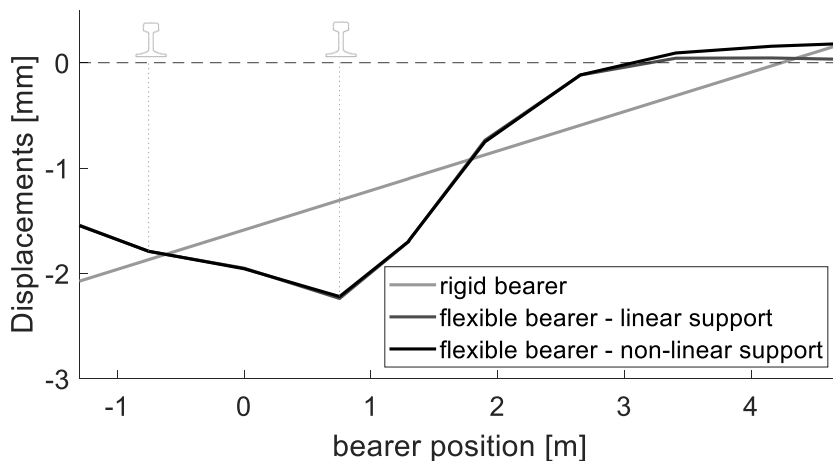


Figure 5.16. Effect on the displacement from using linear and non-linear force elements underneath the long bearer.

Additionally, other changes have been made in the crossover model from the first calibration to the second one in order to improve the model accuracy, which are:

- Rail pad vertical stiffness is updated to 120 kN/mm, as the value of 70 kN/mm is very low and is more a static stiffness than a dynamic stiffness;
- The crossing is no longer simplified as two plain line rails rigidly attached. Instead, the rail properties described in Table 4.2 with area and inertia along the crossing element are considered.

5.2.3 Model calibration

The model calibration performed here consists of comparing the maximum displacements of the bearers obtained from the 2nd campaign and the VI-Rail simulation of the vehicle Mark IV running the turnout at 50 m/s. Note that a lower speed of 30 m/s, which is also a possible speed to negotiate the turnout, has been tested, but little impact was observed on the bearer displacements. Also, the VTI model is not used as it is too simple to represent the crossover at locations where voided bearers, flexible bearers and degraded connections need to be

taken into account. Each simulation takes around 40 min to run VI-Rail plus 10 min to read the output file, which is too long to consider an optimization algorithm that would require a large number of simulation iterations. Instead, a simple tuning of the trackbed stiffness like it was done for the first campaign is preferred, running only a few dozens of VI-Rail runs.

Thus, the iterative process shown in Figure 5.7 is adopted to perform a first model calibration to reach good initial track parameters. The design variables are the vertical trackbed stiffness below the cess and 6ft rails. For each bearer, the difference between measured and simulated displacements is evaluated and the trackbed stiffness is updated with the same order of difference. A minimum value of 5 kN/mm per sleeper end for the track vertical stiffness is considered. This value was introduced in the process to avoid having very low trackbed stiffness in the areas of voided bearers. Lateral stiffness is assumed as 50% of the vertical stiffness. The objective function is given by the sum of the errors on both sides of the track divided by the number of bearers being calibrated (65 in total). The iterative process stops when the variation of the objective function is lower than 0.001%. Figure 5.17 shows the evolution of the objective function, from which a fast convergence is observed in the first 10 iterations and the stop criteria is met after 51 iterations.

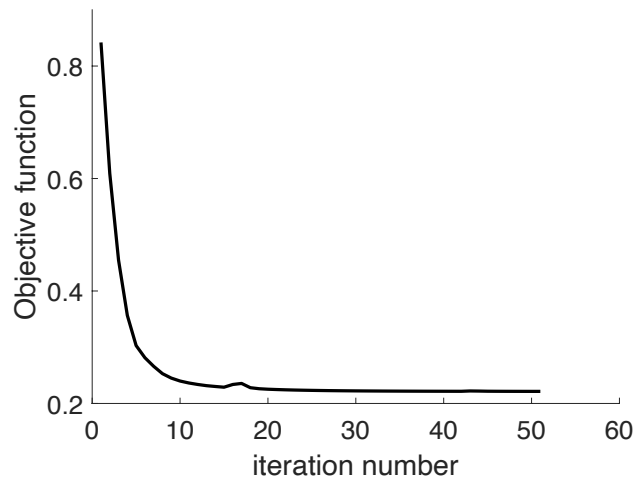


Figure 5.17. Objective function evolution.

The bearer displacements obtained from the calibrated model from the on-site measurements are shown in Figure 5.18. In Figure 5.18 a) for the cess side, a good agreement is obtained between the numerical and the measured displacements. Higher differences are observed between bearers 3 and 4, which were also identified in the first measurements as being a possible voided bearer, and between bearers 55 and 56, which are close to the

crossing on the Up track. Loose bolts on the connection between bearers were also identified, causing the bearer to deflect more locally. On the 6ft side, considerable differences are observed in Figure 5.18 b) around the longer bearers at the crossing panel, i.e. between bearers 44 and 54, and before reaching the longer bearers connecting both tracks, between bearers 25 and 31, which show very big deflections.

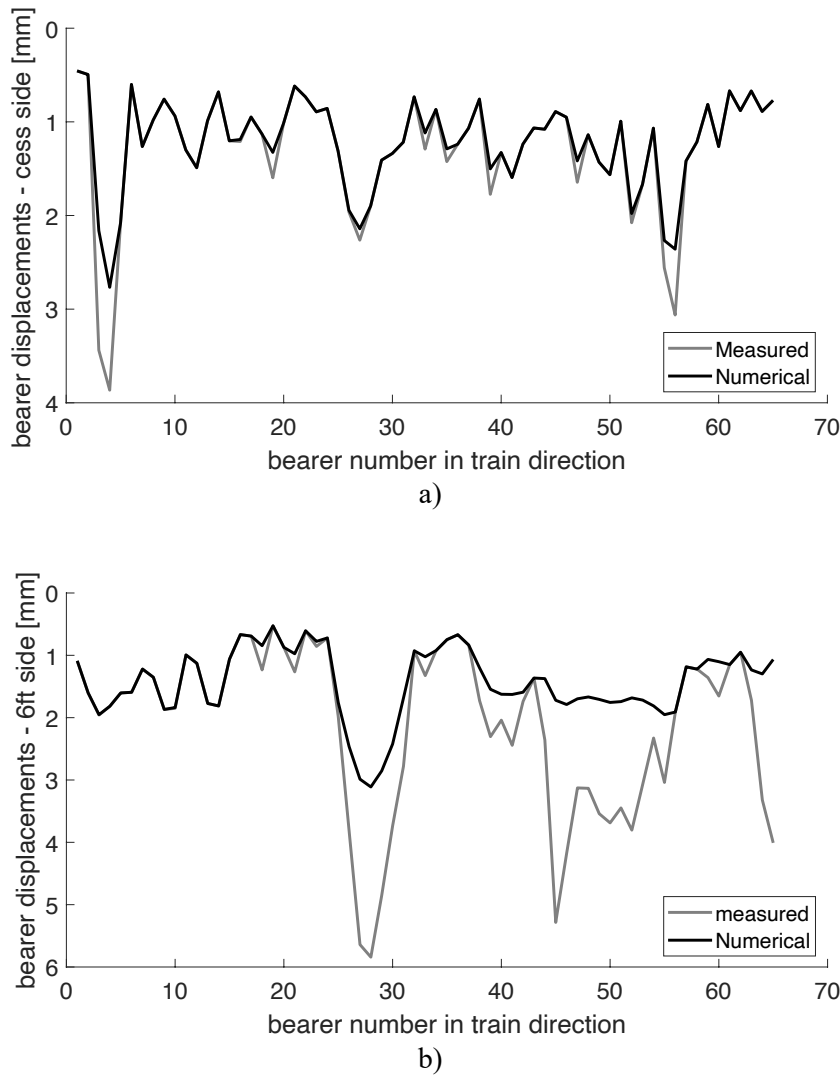


Figure 5.18. Bearer displacements after tuning trackbed stiffness on: a) cress side; b) 6ft side.

All the bearers in Figure 5.18 showing the largest differences have reached the minimum limit of 5 kN/mm per sleeper end, which means they probably have voids underneath that explains why the model cannot match the measurement. Figure 5.19 shows the final trackbed stiffness for each side of the Down track. Table B.2 has the trackbed stiffness values for the switch panel and the difference between the displacements measured and simulated, while Table B.3 has the same values for the crossing panel. The 6ft side has reached the minimum

value more often than the cess side, confirming the trend observed from the measured deflections of the bearers. Therefore, these results suggest that voided bearers need to be considered in the crossover model in order to capture the physical behaviour.

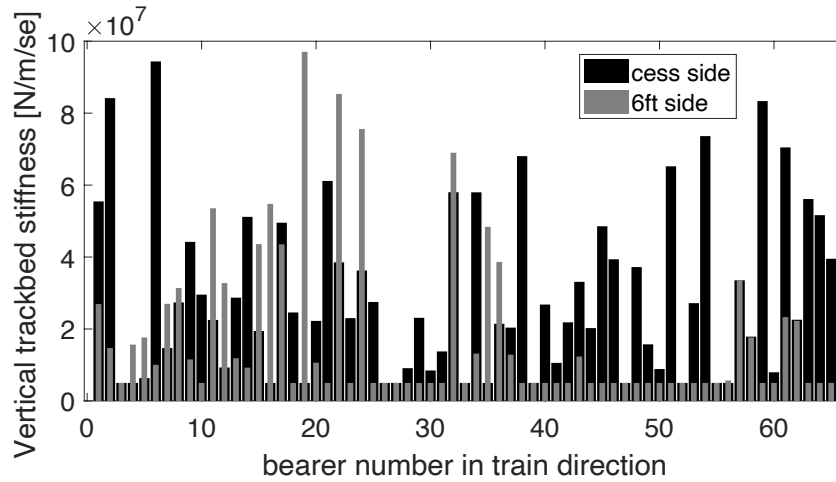


Figure 5.19. Vertical trackbed stiffness after tuning of both sides of track.

Voided bearers are therefore assumed in the areas where bearer displacements are underpredicted. The gaps below the bearers are implemented by increments of 0.5 mm, according to the difference between the measured deflections and those simulated by VI-Rail, as suggested by [104]. These differences are rounded down in multiples of 0.5 mm to get the value of the gap to use. Figure 5.20 shows the differences between numerical and measured displacements for both cess and 6ft sides and the equivalent gaps to consider on VI-Rail. Since the gaps can only be applied on the flexible long bearers, due to these having several springs underneath to distribute the load to the sides of the gap, the rigid bearers require a different approach. For these and since only two supports are considered, a reduction of stiffness in accordance with the gap value is adopted. Equation (5.2) shows how to obtain the reduced trackbed stiffness (K_{eq}) due to the gap.

$$K_{eq} = \frac{K_v}{(1 + \text{gap})} \quad (5.2)$$

For these bearers, the stiffness will be lower than 5 kN/mm/se, which is acceptable since the main focus is on the crossing panel and bearers connecting both tracks. Although in the rigid bearers there are only two supports to each bearer, the flexible bearers are divided between 10 and 11 support elements and the gap should be distributed below a number of

them. Figure 5.20 a) only shows one bearer with a gap on the cress side for the longer bearers (between 38 and 65).

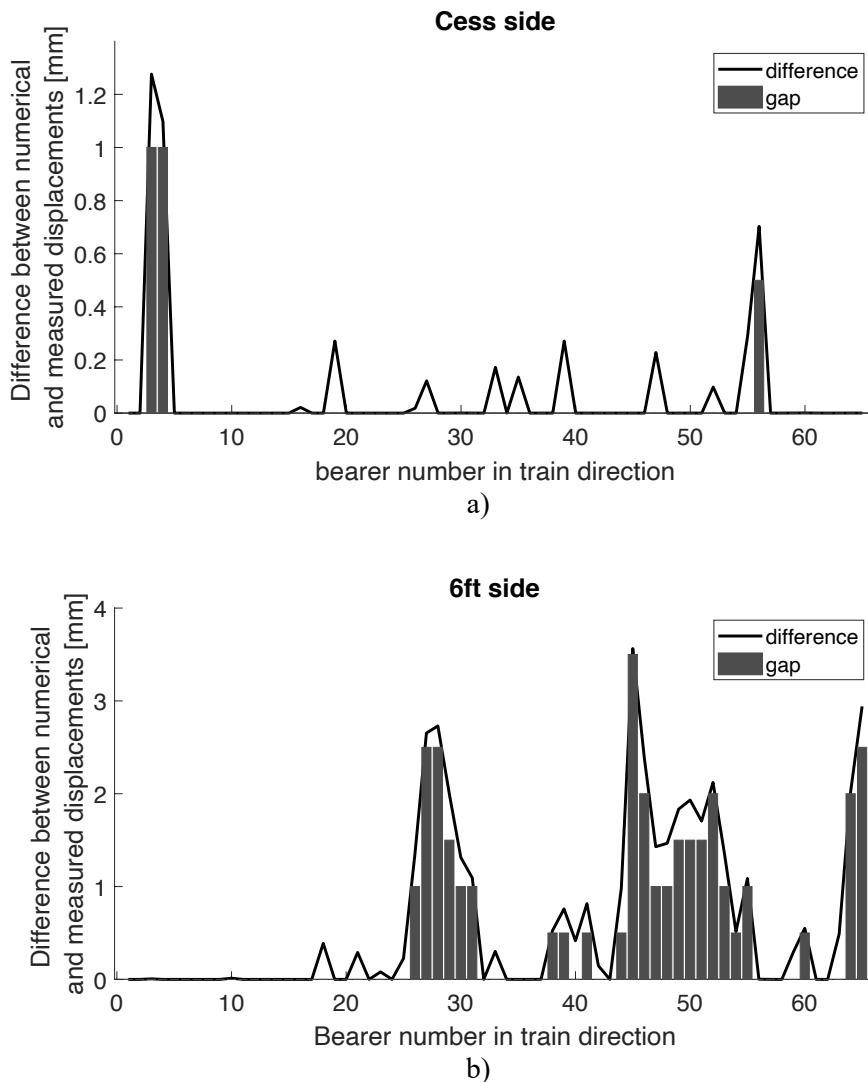


Figure 5.20. Gap values to use on: a) cress side; b) 6ft side.

It is difficult to assume how the void distributes underneath the bearer with only two measurements close to the rails. It could make sense to consider at the centre of the track, below the connection between the bearers because this connection when it fails must deflect more than when it is rigid. But since the two locations underneath the rails are being used to calibrate the trackbed stiffness and the gap underneath the bearer, it is safe to consider this location with the highest gap value and spread it through the neighbour bearer elements. Figure 5.21 shows the proposed gap distribution underneath the bearer on the 6ft side and for the different bearer model types that are considered in the crossover model. The value of the gap obtained from Figure 5.20 b) is applied below the 6ft rail, as highlighted by the

vertical red line. On the two adjacent bushings, the value for the gap is reduced by 0.5 mm. Depending on the configuration of the flexible bearer and the distance between elements, the gap can also be distributed to an extra non-linear bushing from the other track, reduced by 1 mm.

The non-linear bushings not contacting the ground (with gap) have no preload to support its weight and the weight from the structure above. This weight is distributed to the bushing elements with no gap to balance the weight of the bearer. In this work, it has been assumed that the weight of the hanging bearer elements is balanced by the two bushing elements before and after the gap (see Figure 5.21). The load is distributed 75% for the first bushing and the remaining 25% to the next bushing element from each side. The force on the bushing elements with no gap follows the curve in Figure 5.15.

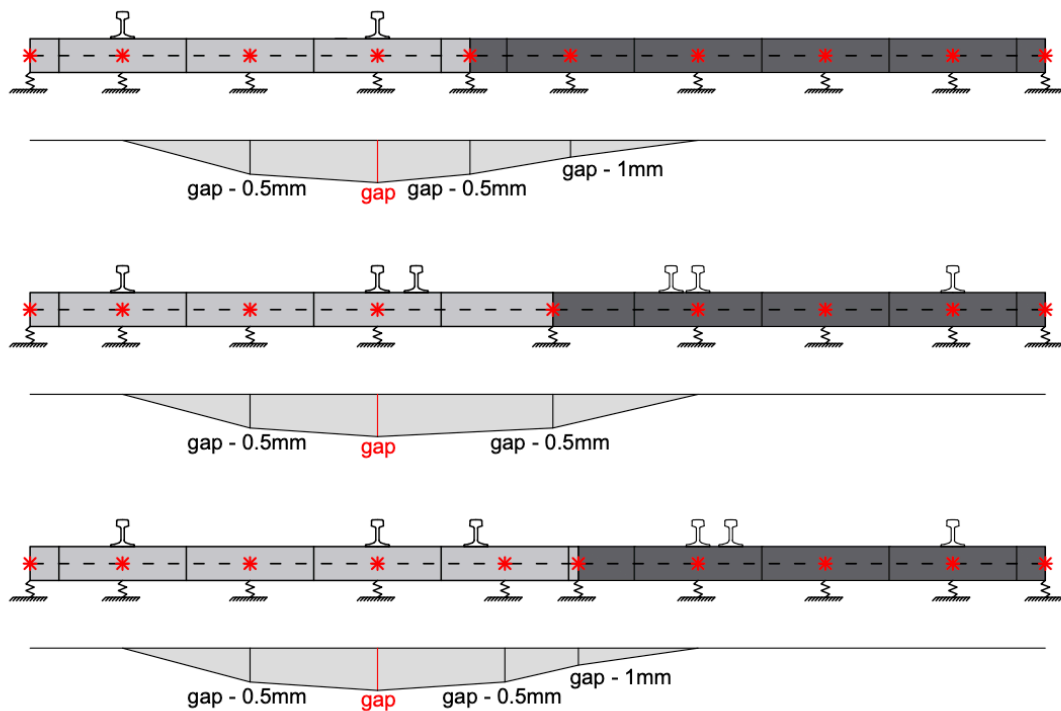


Figure 5.21. Void distribution below each bearer model type.

Contrarily to the constitutive non-linear bushing force element shown in Figure 5.15, here the gap leads to no preload. Figure 5.22 shows the bushing force that is defined as:

$$F = \begin{cases} 0.10 \times Cz \times Vz & Dz - \text{gap} \leq 0 \\ (Kz \times (Dz - \text{gap}) + Cz \times Vz) & Dz - \text{gap} > 0 \end{cases} \quad (5.3)$$

where F is the force, Dz is the bearer displacement, Kz the vertical stiffness, Cz the vertical damping and Vz the bearer velocity. In VI-Rail, a STEP function is used to implement the non-linear behaviour shown in Figure 5.22 and to make a smooth transition between the zero to the linear part of the bushing equation. Figure 5.22 shows the part of the force that is given by the stiffness part $Kz \times (Dz - \text{gap})$.

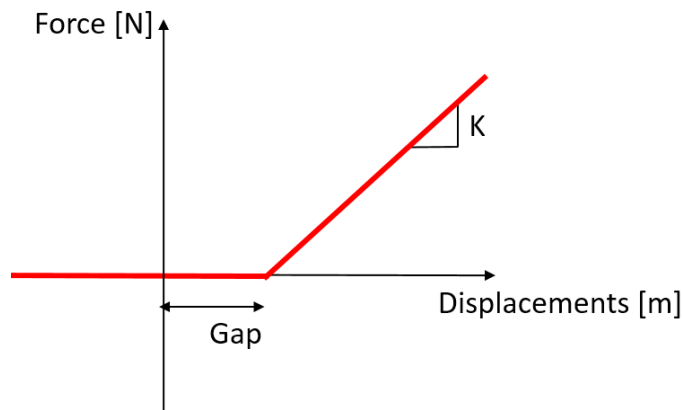


Figure 5.22. Non-linear bushing with gap.

To test the void distribution underneath of a single bearer, the same long bearer configuration presented in Figure 4.12 with a 5.7 ton force applied in both rails from the Down track and a support of 40 kN/mm/se is used. The bearer follows the void distribution showed on top of Figure 5.21 and a gap of 2.5 mm was considered. In the initial static analysis, the bearer naturally deforms because of gravity. Since preloads are considered on the bushings where no gap is considered, the sleeper stays mostly in the initial position. In the area of the gap, slight bending of the bearer occurs, since it is only supported on the adjacent bushings with no gap and not on that area. Figure 5.23 shows the final bearer displacements for the three cases: rigid bearer with no gap, a flexible bearer with the non-linear bushing and no gap and finally the case using the gap distribution mentioned. An increase of deflections around 0.6 mm is observed below the cess rail while an increase of 1.4 mm is observed on the 6ft side. Although this also increases the bearer displacements on the cess side, these are smaller than 6ft side and if not wanted, they could be contradicted by increasing the stiffness on that side. These results are for an isolate bearer and the case of the full crossover will show additional rigidity from the bearers being connected through the rails. Also, important to reflect on the increment of bearer movement against the value of gap used, i.e. a 2.5 mm gap leads to an increment of 1.4 mm. This means the gap values in Figure 5.20 may not be enough to get the displacements measured in Figure 5.12.

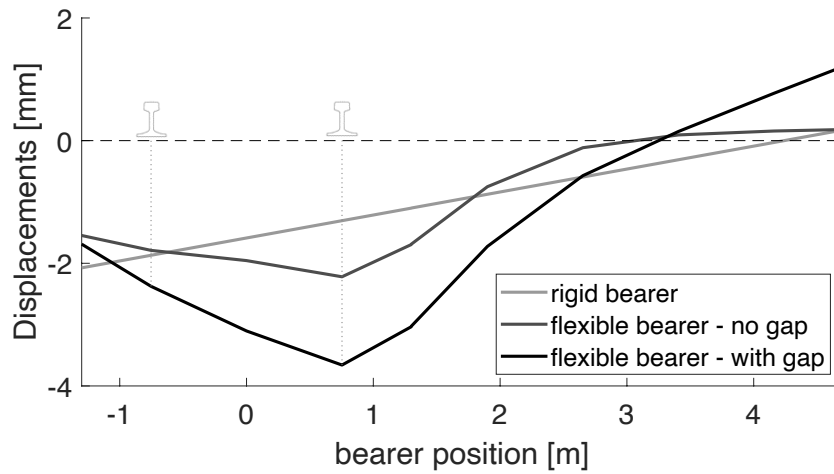


Figure 5.23. Effect on the bearer displacements from considering or not the void underneath.

Figure 5.24 shows the diagram with all the steps for the model calibration. This calibration involved several VI-Rail model variants of the crossover that had to be considered in order to find the model that best reflects the voids and damaged connection. In each case, changes are made in the model, as referred in Figure 5.24.

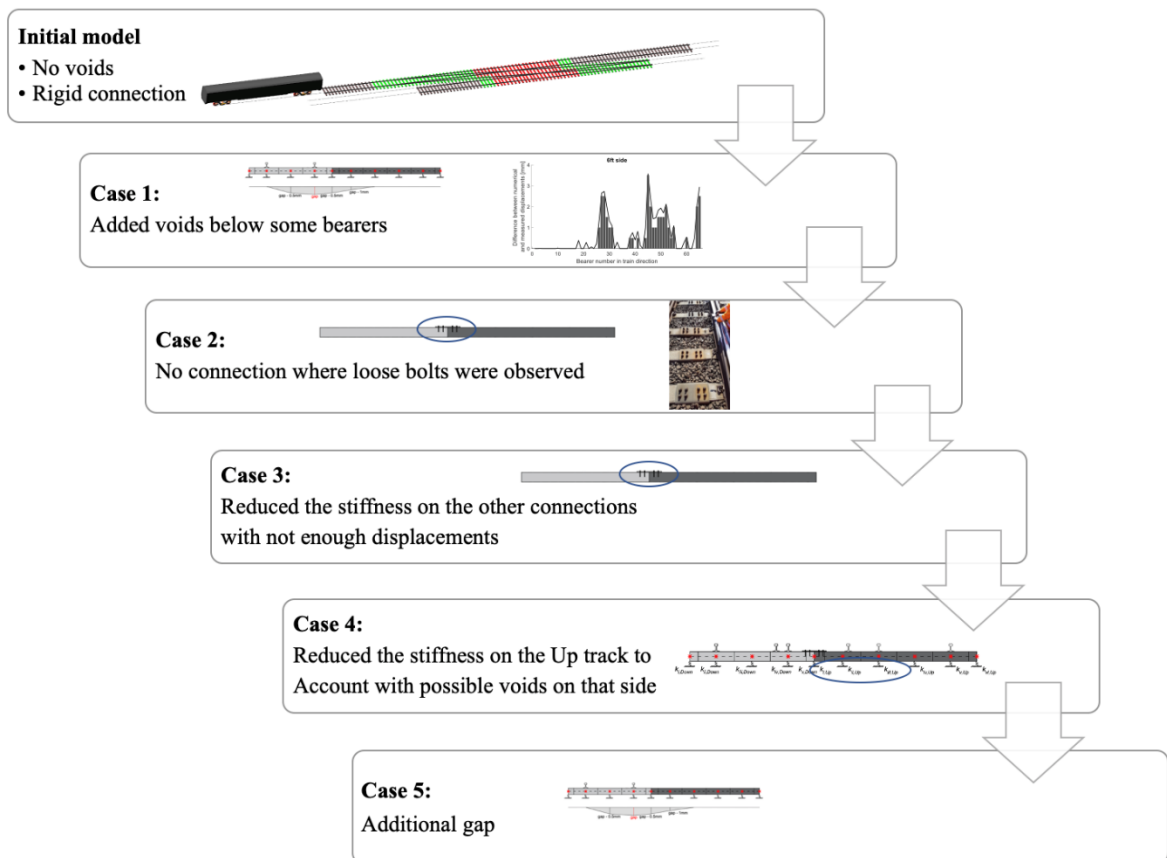


Figure 5.24. Diagram with calibration steps.

The results obtained with the different cases are shown in Figure 5.25 and a detailed description of each case with comments on the respective results are presented as follows:

- In Case 1 voided sleepers with the gap values obtained from Figure 5.20 and the distributions presented in Figure 5.21 are considered. The trackbed stiffness of rigid bearers is reduced according to Equation (5.2). For these last ones, this assumption shows a good improvement, which is noticeable around bearer 29 on the 6ft side. The long bearers show a slight improvement on the 6ft side, but smaller than the gap considered. This also increased the displacements on the cess side and consequently the difference between VI-Rail and measured displacements. The differences on the 6ft are still big and the model still requires some adjustments.
- Case 2: loose bolts were identified at specific bearers which can compromise their ability to keep both tracks rigidly attached. To the bearer identified near the first crossing and shown in Figure 5.14, and also on the second crossing, the connection was removed. The bearers identified were bearer number 45 under the crossing leg, bearer 47 under the crossing nose and the two after and bearer 52 under the crossing nose on the Up track. These changes increased the displacements below the crossing element, i.e. between bearer 45 and 51 with two little spikes at bearers 45 and 47. These changes were still not enough to make the model deflect as much as recorded in situ.
- Case 3: The previous case has shown that the connection has a big effect on the bearer displacements. So far only the bearers with rust on top of the connection and some loose bolts were removed on the model, while the remaining joints were kept nearly as rigid. The values used for the connection were 500 MN/mm to the vertical stiffness and 300 MNm/rad to the rotational stiffness. The connection degrades over time with traffic and bearer movements, which makes sense to assume that they no longer act as rigid. Both vertical and rotational stiffness values of the connection were reduced to 50 MN/mm and 30 MNm/rad, respectively, for bearers where a gap was introduced (i.e. with trackbed stiffness on the 6ft equal to 5 kN/mm). These changes showed a very good improvement around the crossing leg end on bearer 45 and before the crossing, between bearer 39 and 41. The model is not capturing the increase in bearer displacements after the crossing nose on the Down track and the area of the second

crossing on the Up track. It is important to mention that the same rail properties (mass and inertia) for the crossing on the Up track as on the Down track were assumed.

- Case 4: Some of the Up track was also instrumented and bearer deflections are shown in Figure 5.12. There are no evident peaks and high displacement values that could lead to the conclusion of void bearers. Looking at those values is not enough to conclude the existence of any gap below the 6ft side of the Up track. With this in mind, the stiffness on the 6ft side of the Up track that was assumed equal to the Down track, was lowered according to the following equation:

$$K_{reduced} = K_v \div \left(1 + \frac{Disp_{exp,6ft} - Disp_{case\ 3,6ft}}{Disp_{case\ 3,6ft}}\right) \quad (5.4)$$

The equation takes into consideration the displacement from case 3, $Disp_{num,6ft}$, and the increment of displacements needed from the difference between numerical and measured deflections. This approach did not show any improvement on the displacements below the Down track as shown in Figure 5.25.

- Case 5: Last change made to the model was checking the differences between the VI-Rail and measured bearer deflections and add these differences as additional gap. This increase of gap showed a reasonable impact on the bearer displacements near the leg end of the crossing and the second crossing, which were the two areas with the biggest differences. With all these changes, it was possible to reduce the average error on 6ft side of the long bearers (between bearer 38 and 65) from 32.6 % to 9.5 %. The error on the cess side increased from 2.4 % to 13.8 % but can be easily adjusted back with some correction on the trackbed stiffness on that side. Correcting once the stiffness in the same way that it was done in Figure 5.7, the final average errors are 12.3 and 6.4 % for 6ft and cess sides, respectively. This is a very good improvement from the starting model.

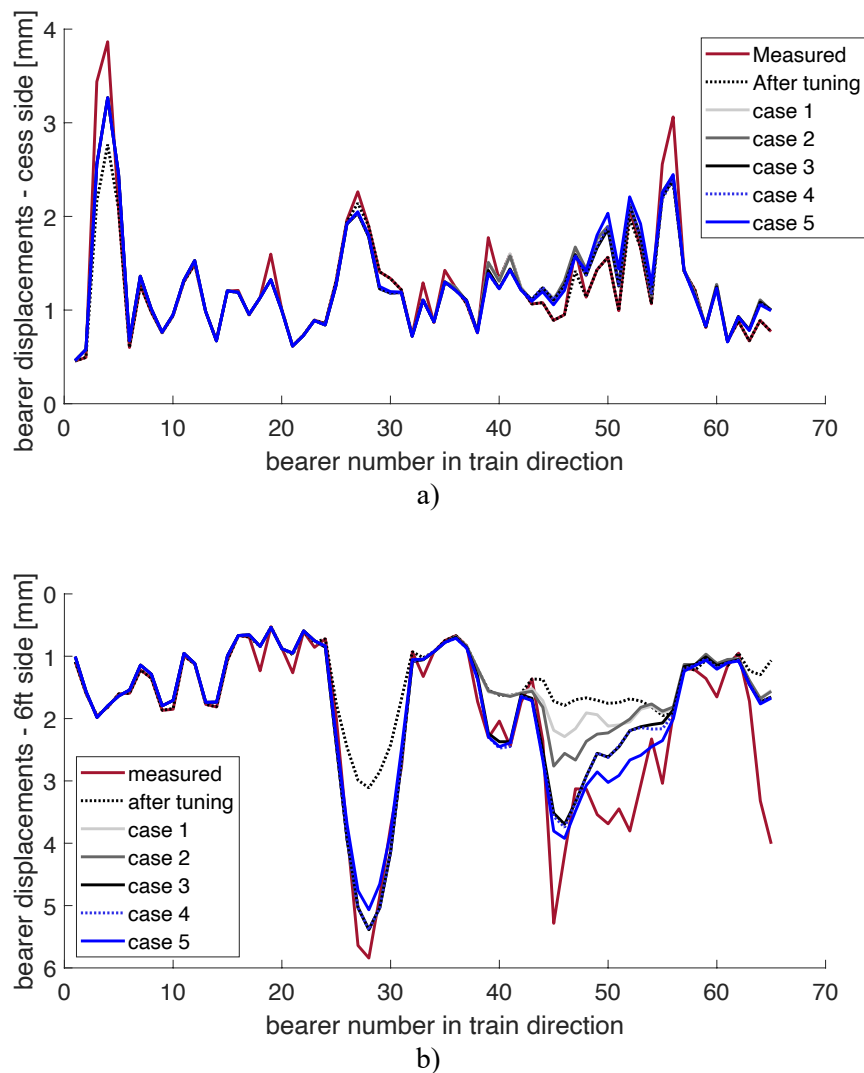


Figure 5.25. Final bearer displacements from different cases studied.

5.3 CONCLUSIONS

In this chapter, the calibration of the VI-Rail model of a railway crossover, presented in Chapter 4, has been performed for the site measurements obtained from two measurement campaigns in 2016 and 2019. Geophones were used to measure bearer velocities, which enabled obtaining peak displacements used to calibrate the numerical model. Since a second campaign was made 3 years after the first one, some conclusions were made regarding the evolution of bearer movements and the state of degradation of the site.

The first campaign concentrated on two areas of the site, one in the switch panel and the other on the crossing panel, with every 2 bearers on the cess side and a few bearers on the 6ft side being measured. The calibration of the trackbed stiffness was carried out with an

additional model which was compared with VI-Rail and a good agreement between the two was achieved, mainly on the switch panel. Due to the limited information on the 6ft side, a second campaign was carried out by the University of Southampton which involved testing every bearer for a long length of the down track and the crossing panel of the Up track. This new data showed an increase in displacements that could indicate the existence of voided bearers and degraded connections between the two tracks. Some observations and photos registered on the site also confirm the degraded state of some connections. With this new data, the VI-Rail model was updated to replicate the deflections measured.

The model had to be updated to consider not only the bearers flexibility but also the voids underneath and the degraded connection. The task of updating the model allowed to understand how important the connection on the long bearer is to the overall behaviour of the site. The increment of displacements in the centre of the track could be related to the existence of voids, caused by the migration of the particles of the ballast, but also from the connection that degrades over time and acts less as rigid or even fails completely to connect the two tracks. Overall, the changes applied to the numerical model led to an improvement close to 20% of the average error between the numerical and measured displacement on the 6ft side of the crossing panel with long bearers.

A void distribution around the 6ft rail was considered, but different combinations could be considered which could lead to similar results. Also, some assumptions were made regarding the types of degradation that could be on site, which may not be correct. All the dynamic analyses were made using as-new crossing element profiles and the irregularities measured in 2016, instead of 2019. The use of the correct information on the analyses could lead to an amplification of the dynamic forces that could lead to higher bearer displacements and different conclusions in terms of gap values. Therefore, the model validation would be possible if void-meters would be used to measure the gaps below the bearers, which would reduce the uncertainty regarding the amplitudes of the gaps.

This chapter allowed for a better understanding of the evolution of the site, which can be translated to other S&Cs. The track model developed here was an essential tool to study some of the degradation mechanisms and can be used to build other S&C layouts. This site has the bearer connection always between rails from the diverging route, but different locations for the connection could be studied to understand its effect on the overall site behaviour. The track model could also be complemented with settlement equations to study

the long-term behaviour of the site, predicting the evolution of voids and the degradation of the connections.

6 APPLICATION OF CALIBRATED MODEL TO CROSSOVER DESIGN

The detailed crossover model that has been proposed in Chapter 4 and then calibrated in Chapter 5 is used here to further understand the dynamic performance of the vehicle-turnout system as a function of the different track components and their parameters. The calibration of the model allowed not only to get the corresponding bearers displacements measured but allowed to identify possible degradation methods, which were key to obtain the level of bearer displacements measured. This chapter allows to study design choices of this site, such as the use of USPs or new designs for the bearer connection and study how the degradation mechanisms identified in the previous chapter relate to each other.

The chapter starts with the assumption of a perfectly homogenous trackbed stiffness and seeks to understand the role played by some elements of the railway crossover, in particular their contribution to the stiffness variability along the track. Many components from the substructure, such as the crossing, the switch elements, the check rails, etc. play an important role in the stiffness variability of the track. To also understand the influence of the trackbed stiffness on the composite stiffness variation along the crossover, two different trackbed stiffnesses are considered and compared to better understand how they interact with the other components of the track.

The case study described in Chapter 4 was the first UK site including Under Sleeper Pads (USPs), which made it an interesting case of study. On the renewal of this site in 2012, two types of USPs were installed, one with a soft and other with a medium pad stiffness, to homogenise the track stiffness along the site and hence reduce the transient track loads. In this chapter, these assumptions are studied and compared to the option of using only the medium USP for the entire length of S&C panels.

Voids are likely to occur due to the high transient track loads that are observed in a turnout, namely in the crossing panel as it is observed in Chapter 5. Hence, reaction forces in the bearer connections increase, leading to its degradation and ultimately to its failure. In this chapter, alternative connection designs are tested to better understand how this element affects the whole crossover behaviour.

6.1 THE INFLUENCE OF TRACK BED STIFFNESS

The trackbed stiffness, which represents the ballast and soil supporting the sleepers and rails, plays a role in the vehicle-turnout interaction for which the lowest possible transient forces are desired. One term used to study the variability of the track stiffness is composite stiffness, which is defined by the ratio of vertical force and vertical deflection measured for each rail. The composite stiffness combines the effects of the bending stiffness of the rails and bearers with the vertical stiffness of the rail-pads and trackbed. In a S&C where the properties of the bearers and rails change significantly, the composite stiffness varies considerably compared with plain line (see section 2.1.2).

The bending stiffness of the rail and the bearer or the rail-pad stiffness are usually well controlled and relatively easy to quantify, while the trackbed stiffness is not. Assuming that during track construction one aims to achieve a homogenous support, a constant value is assumed throughout the entire crossover. To test the influence of the trackbed stiffness on the composite stiffness, two values for the trackbed stiffness were selected. The highest value equal to 40 kN/mm/se, where 'se' means sleeper end, also used in Chapter 4, whereas the lowest value of 20 kN/mm/se to consider a softer track, based on the trackbed stiffness obtained from the 1st calibration presented in Chapter 5, where the track was assumed as in good condition. The damping is obtained from the relation between the mass and the stiffness, as described in Chapter 4. The rail properties from both switch and crossing are considered, the bearers flexibility is taken into consideration and the connection between the bearer is assumed as rigid.

The composite stiffness is obtained at the rail level above each bearer through a static analysis where a load of 100 kN is applied on the Down through line. Figure 4.3 presents the composite track stiffness of the bearers for the Down route, where the crossing nose and switch toe positions are identified, and a grey box highlights the crossover section that comprises the flexible long bearers. The simulation shows that the increasing bearers length, which is observed after bearer 12, and the presence of the diverging rail after bearer 8, which adds bending stiffness in that area, increases the composite stiffness on the 6ft side. The increase of composite stiffness is higher on the 6ft side for bearers fully connected to the Up line, that is, between bearers 38 and 65. The highest composite stiffness is seen at the crossing element of the 6ft side (between bearers 45 and 51). A linear increase of composite stiffness between bearers 8 and 13 is observed, which can be related to the start of the switch

blade before diverging from the stock rail. On the cress side, an increase of composite stiffness due to the presence of check rail is visible between bearer 41 and 49. The check rail located between bearers 53 and 59 on the left side of the diverge route will contribute to the composite stiffness on the 6ft side of the Down track. The crossing on the Up track, located between bearers 52 and 58 do not show much impact on the composite stiffness on the 6ft of the Down track.

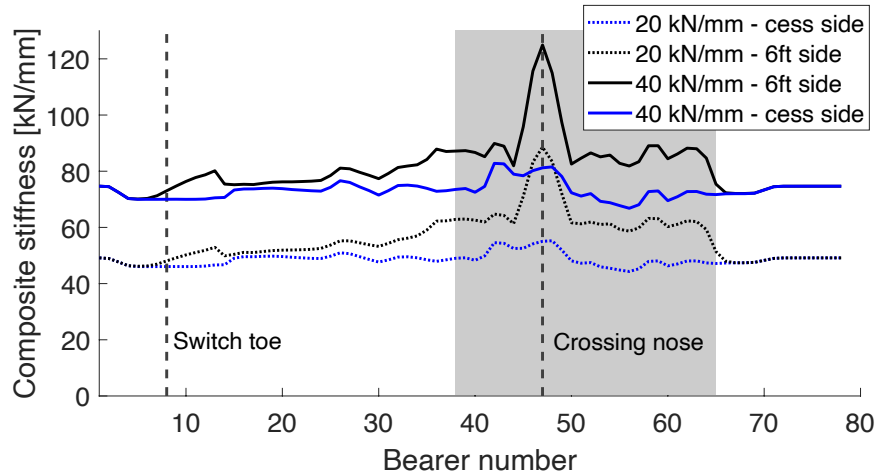


Figure 6.1. Composite stiffness for two different trackbed stiffness: 20 and 40 kN/mm.

When comparing the two trackbed stiffnesses, the differences between the two sides of the track are higher when considering the 40 kN/mm/se support. As an example, the composite stiffness for the track with 40 kN/mm/se is higher than track with softer support of about 30 % at the crossing nose (bearer 47) and 53 % at the end of the switch element (bearer 13).

Although some conclusions were made in how the composite stiffness may affect the vehicle-track coupling system, a simple quasi-static composite stiffness analysis does not provide a direct measure of how the variation in stiffness affects the dynamic behaviour. Thus, a dynamic analysis of the Mark IV coach running at 50 m/s negotiating the turnout is performed. Figure 6.2 shows the vertical contact forces of the front wheelset for the two trackbed stiffnesses, 20 and 40 kN/mm/se.

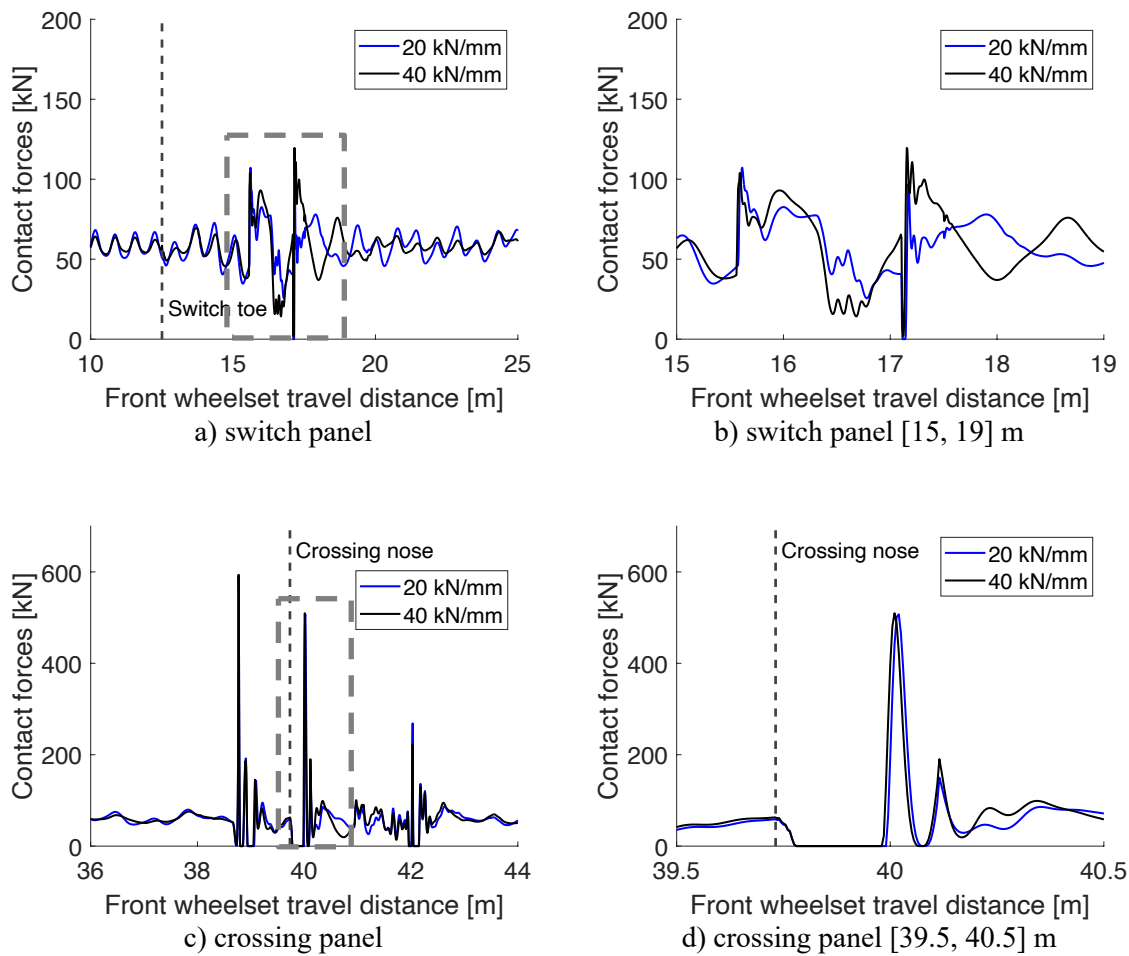


Figure 6.2. Vertical contact forces from the front Wheelset of the Mark IV coach, on the 6ft side for two trackedbed stiffness of 20 and 40 kN/mm

The contact forces on the crossing element, presented in Figure 6.2 c), seem identical with the same peak value but slightly moved. The contact forces in this area are mainly controlled by the wheel interacting with the different rail profiles. On the switch panel shown in Figure 6.2 a), the differences are more noticeable. This could be explained by the lower frequency input in the switch interacts more closely with the track frequency response and we see phase angle response in the interaction forces as a function of track support stiffness. In the crossing on the other hand the frequency impulse of the force is much higher and does not interact with the track response. There is a reduction of the second peak force of about 19 % and the longer wavelength force response that is much changed with reduced overall with the lower track stiffness. The dynamic amplification occurs after the switch, in the area where the wheelset changes contact between the stock and the diverge rails.

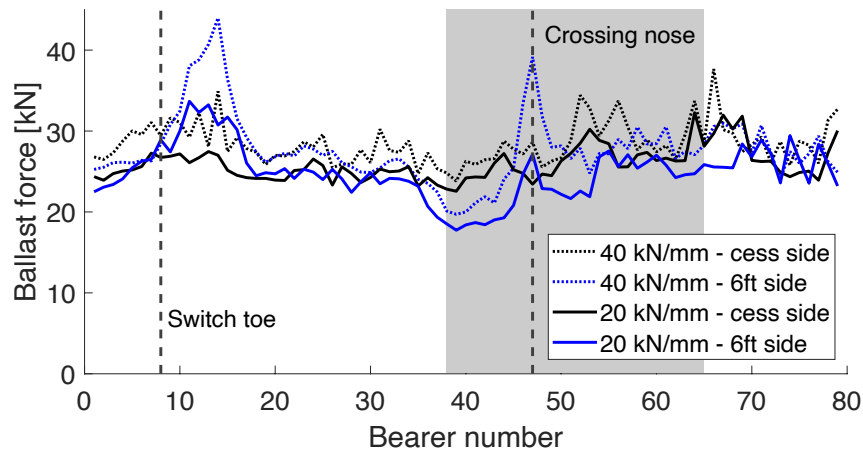


Figure 6.3. Ballast forces underneath the rails of Down through route for two different trackbed stiffness: 20 and 40 kN/mm.

Figure 6.3 shows the maximum ballast forces under each rail from the Down track for the Mark IV coach. For the rigid bearers, the ballast forces are represented by the reaction forces of the bushing elements that are under each rail. For the flexible bearers, which are supported by several bushing elements as shown in Figure 4.11, the ballast forces are obtained as the sum of the forces of all bushings on each respective side, i. e., the reaction force on the cress side is given by the force on bushing *i*, *ii* and half force of bushing *iii*, while the reaction force on the 6ft side is given by the other half force of bushing *iii* and the forces of bushings *iv* and *v*, accordingly with the bushing distribution shown in Figure 4.11. The ballast force on each side is around 25 kN, which represents around 43 % of the wheel force, which agrees with the mentioned in [106]. Amplification of the ballast forces is observed when the wheel load transfer in the switch and crossing occurs, which are the areas with higher dynamic forces on the wheel/rail interface (Figure 6.2). The stiffer trackbed stiffness shows an amplification of the ballast force compared to the softer value on the switch load transfer area of 32 % and underneath the crossing nose of 44 %. Compared to the average 25 kN on the other areas of the track, the increase is 76 % and 57 % for the switch and crossing load transfer, respectively. These increase of ballast forces explain the ballast degradation and voided bearers identified on the crossing panel.

The forces transmitted to the connection between bearers are of great importance to analyse as these components showed severe damage at the site measurements. Figure 6.4 shows the maximum forces and torques registered at each long bearer for the Mark IV coach passage. The two different trackbed stiffnesses do not show significant differences, with the

lower stiffness having an increase of around 2 % and 10 % for the force and torque transmitted to the bearer underneath the crossing nose, respectively. Therefore, the trackbed does not play a role in the reaction forces in the connection between bearers. What is more important to refer is how significant the increase of force transmitted in the crossing is, compared with the remaining track. The force on the bearer at the crossing nose is around four times bigger than the remaining bearers, whereas the torque is eight times bigger.

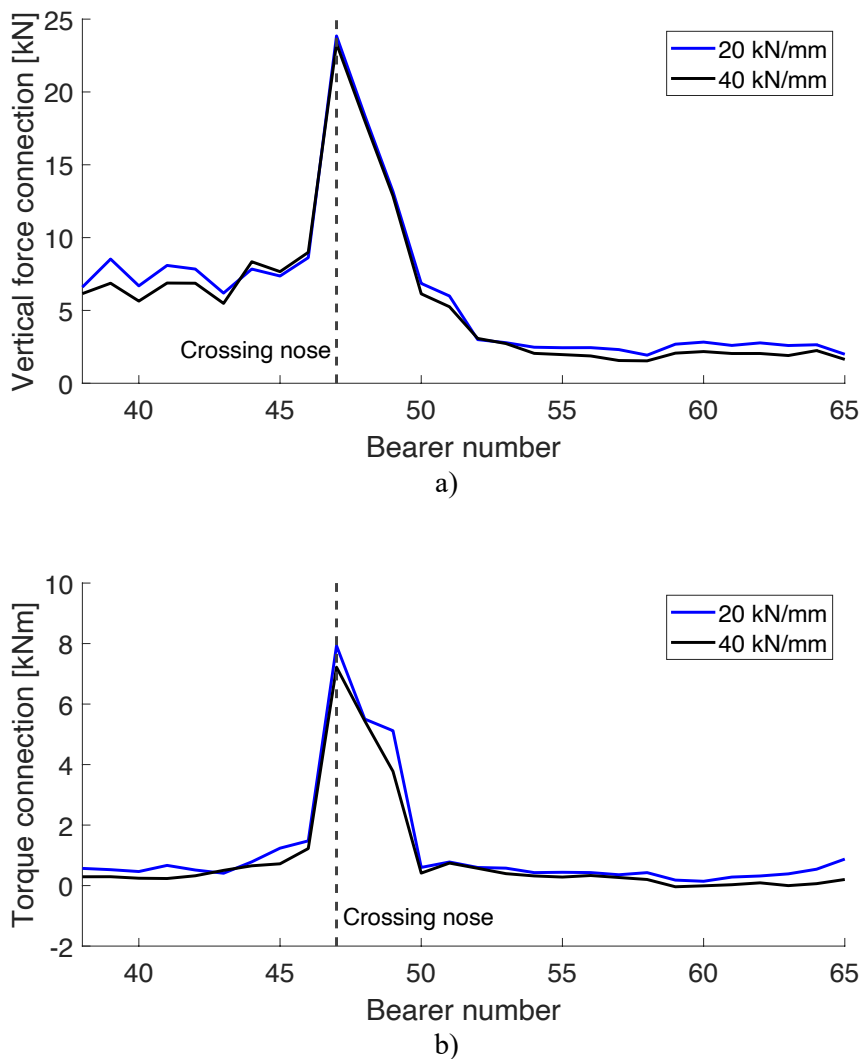


Figure 6.4. Vertical force a) and torque b) at the connection for different trackbed stiffness, 20 and 40 kN/mm

Another important quantity used in the previous chapter to calibrate the model is the bearers displacement. High values of bearer displacements may lead to the appearance of voids due to ballast compaction or migration. Figure 6.5 shows the maximum displacements of each bearer for the Mark IV coach and the two trackbed stiffness. The lower trackbed

stiffness leads to higher bearer displacements, as expected. These differences are about 0.5 mm with the exception of the longer bearers connecting the two tracks (grey box). On the closure panel, both sides of the Down track seem to displace similarly and about 0.6 mm and 1 mm for the stiffer and softer supports, respectively. For the bearers connecting both tracks, overall the 6ft side deflects less than the cess side. This means that overall, the vehicle will see a slight roll of the track towards the cess in those initial conditions. The opposite behaviour is observed on the switch panel and on the crossing load transfer area for the stiffer track, where due to the higher wheel-rail interaction loads on the 6ft side, that same side shows more movement than on the cess side locally. When comparing the two trackbed stiffnesses, there is a significant difference in the area of the longer bearers. The difference between bearer deflection on the 6ft and on the cess sides are more noticeable to the lower trackbed stiffness. This is most probably caused by the overall increased bending of the bearer under the lesser reaction of the lower support which makes it rotate towards the cess side overall.

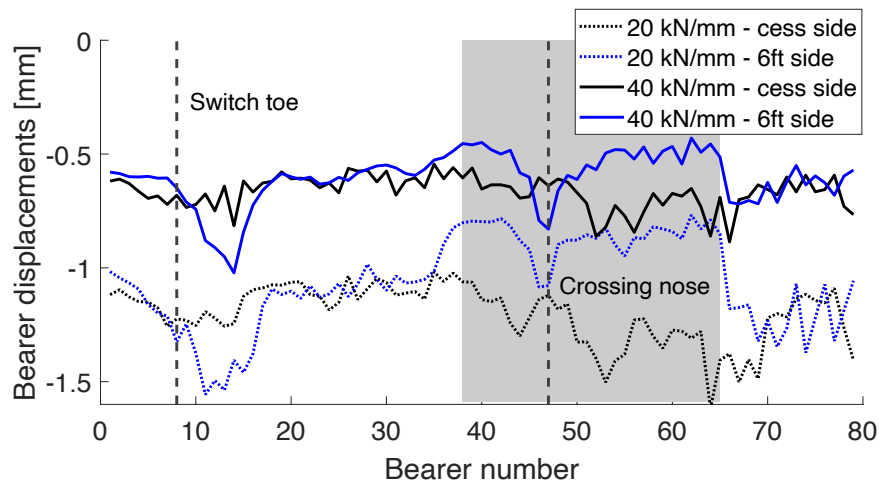


Figure 6.5. Maximum bearer displacements for two different trackbed stiffness: 20 and 40 kN/mm.

6.2 DESIGN CHOICE FOR UNDER SLEEPER PADS

The site selected has two types of Under Sleeper Pads (USPs) installed. While the choice of USP modulus was calculated and defined by supplier Getzner, it was not clear to NR whether the choice of having two different modulus was the best choice, and whether the modulus itself was the best one to use at the site. It is therefore of interest to test the hypothesis that maybe one type of USP is sufficient.

The main goal of using two types of USPs is supposedly to provide a smoother transition throughout the crossover. In order to check if that is the case, the track behaviour should be analysed by looking at the composite stiffness variation along the track and the USP influence on the contact forces and ballast forces. The trackbed stiffness is set to 40 kN/mm/se and USPs are considered by adding a second spring in series with the main one in the model. The values adopted for the USPs stiffnesses are listed in Table 4.3. The composite stiffness is obtained from several static analyses performed above each bearer where a load of 100 kN is applied in each rail from the Down through line.

Figure 6.6 shows the composite stiffness for the rail of each side, cess and 6ft and for the three cases: with no USPs; with medium and soft USPs, as described in Chapter 4; and the hypothesis of using only medium USPs. A substantial reduction of the composite stiffness due to the USP is observed. On the 6ft side, this reduction of composite stiffness is smaller than that observed on the cess side. With the increase of bearers length, the composite stiffness on the 6ft increases being on pair with the composite stiffness measured at the beginning of the track where no USPs are installed. From the results in Figure 6.6, there is not a considerable difference when using two different types of USP, rather than under the crossing nose, where a softer pad will reduce the composite stiffness. Lowering the composite stiffness might reduce the contact forces but might increase the bending stresses and hence reduce the fatigue life of the rail. The increase in composite stiffness on the crossing nose compared with the bearers before is around 53 % for the case with no USPs, and can be reduced to only 48 % and 46 % when using the medium or the soft USPs, respectively.

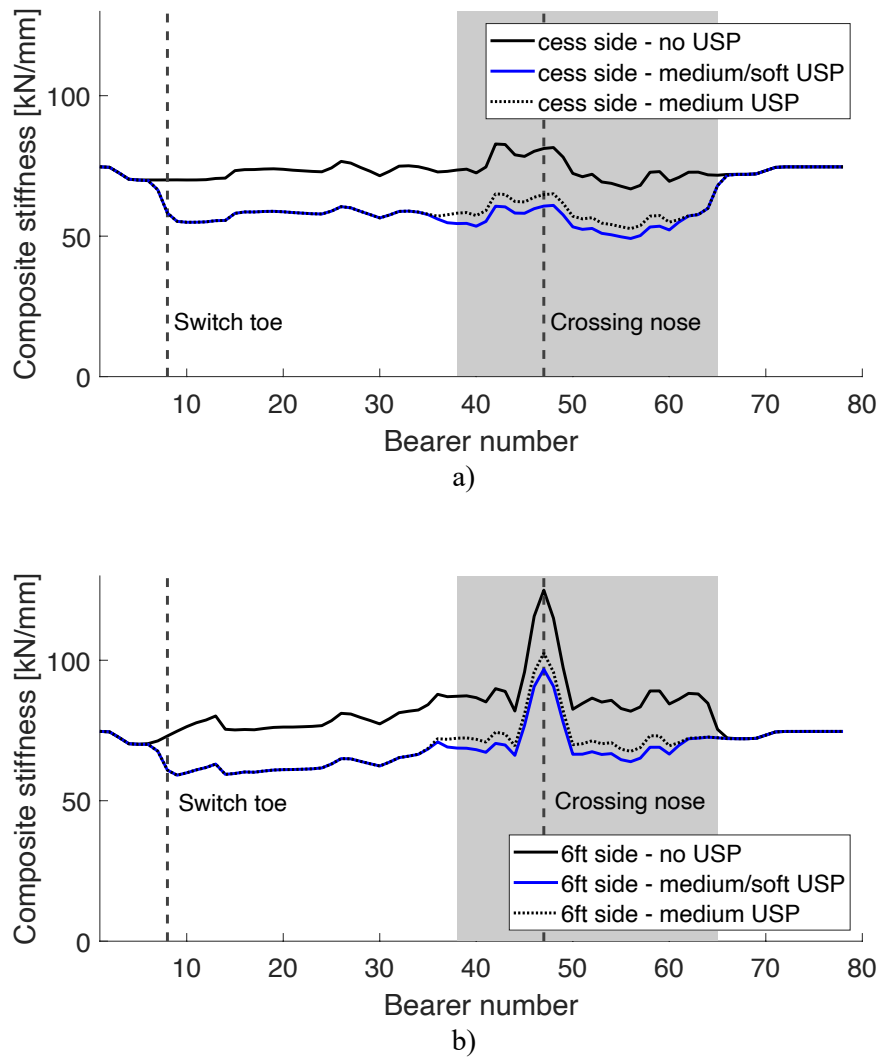


Figure 6.6. Composite stiffness considering constant trackbed stiffness equal to 40 kN/mm and two different USP distributions for: a) cess side and b) 6ft side.

Figure 6.7 shows the vertical contact forces for the front wheelset of the Mark IV coach at 50 m/s speed. The difference between using and not USP is not as significant as the impact on the composite stiffness. The peak force on the switch is about the same as using no USP and the remaining contact forces on that area see an oscillation between 5 to 10 %, either as an increase or decrease. The crossing peak force for the case of the softer USP has a small increase of 2.6 % while the medium USP is just 0.2 % higher (basically the same). The second peak sees a higher decrease of the force on about 11% for the soft USP and 15 % for the medium USP. These are quite interesting observations, where the stiffer pad leads to smaller contact forces on the crossing panel than the softer pad.

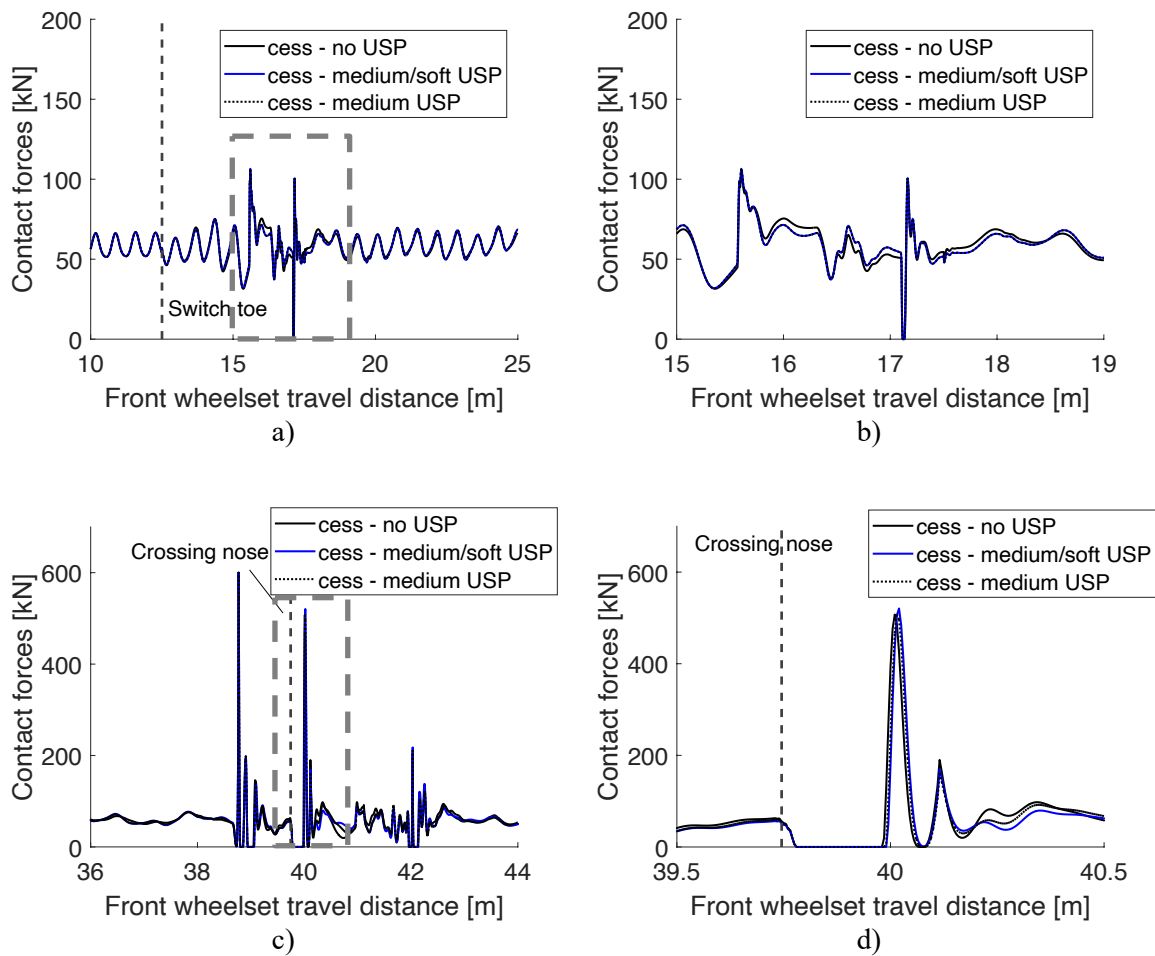


Figure 6.7. Vertical contact forces from the front wheelset of Mark IV coach, a constant trackbed stiffness equal to 40 kN/mm and two different USP distributions for: a) and b) switch panel and c) and d) crossing panel.

One of the main goals of the USP is to better distribute the load to the ballast. Figure 6.8 shows the maximum ballast forces obtained on the cess and 6ft sides for the Mark IV coach passage. The USP, present between the switch toe and the end of the longer bearers (bearers 9 to 65), show an average reduction of 5% on ballast forces from 26 kN to 24.7 kN (calculated between bearer 17 and 37 on the closure panel). On the switch element, the ballast peak force is reduced by 20 % using the USPs. On the crossing panel, this reduction is 22 % and 18 % for the soft and medium USPs, respectively. Since the USPs are considered as a reduction of the trackbed stiffness given by the equivalent value of two springs in series, the consideration of USPs would lead to higher displacements (like in Figure 6.5), which could be assumed as a negative aspect of the crossover behaviour. These conclusions would not tell the whole story since the model does not consider the actual area of contact from the

bearer and the ballast particles and other advantages from using USPs. Using USPs can reduce the damage caused on the ballast by increasing the contact area and reducing the strains on the ballast [107]. [108] shown that the USPs can minimise some of the discontinuities of the track stiffness present in transition zones.

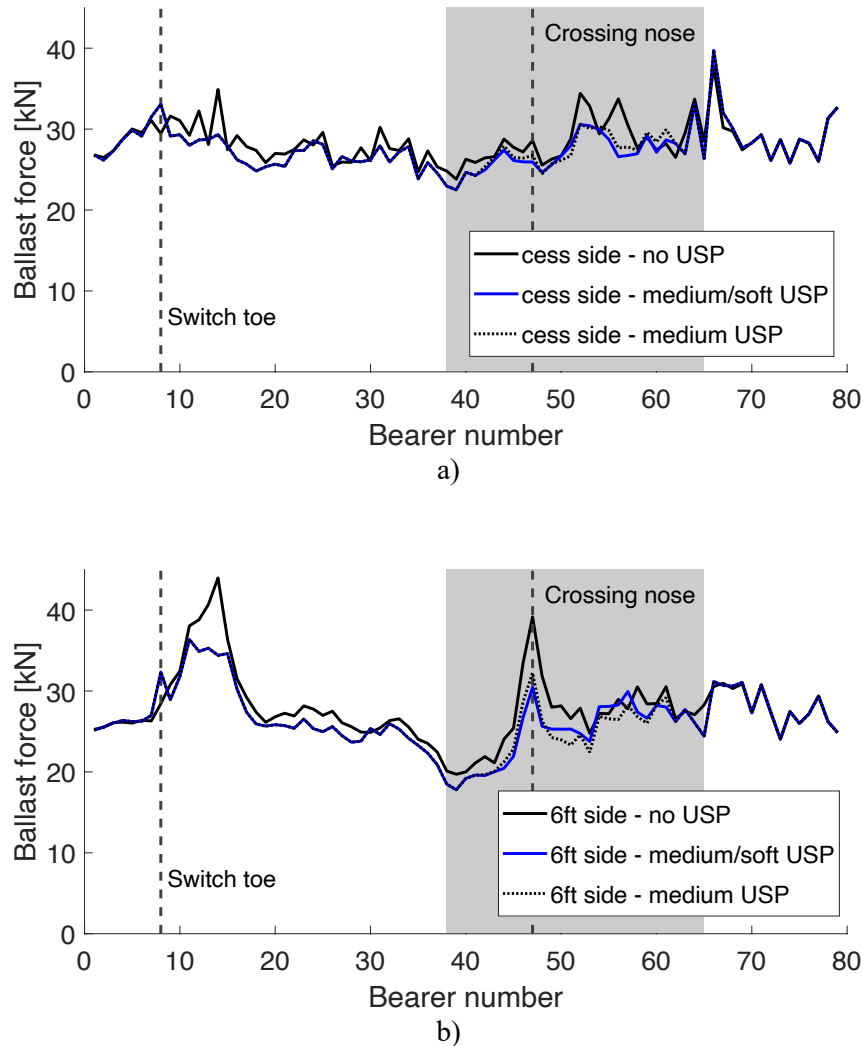


Figure 6.8. Ballast forces for Mark IV coach passage, a constant trackbed stiffness equal to 40 kN/mm and two different USP distributions on: a) cress side b) 6ft side.

6.3 DEGRADATION AROUND THE BEARER CONNECTIONS

The presence of voids underneath the bearers and degraded bearer connections were identified during the two experimental campaigns presented in Chapter 5. The places identified with the higher gap values are where higher dynamic forces are observed, and where the voids are likely to develop first. The degraded connection between bearers was also identified near voided bearers. Both effects are most likely related to each other. The

voids may appear due to the bigger displacements observed in the areas with dynamic amplification of contact forces, which would lead to an increase of the forces and torques on the connection. If the maximum strength of the connection is reached, its degradation would occur. Once the connection is no longer in good shape, it will no longer act as expected to make the quasi-rigid link between bearers of the two tracks less rigid. To prove that the appearance of voids could lead to damage on the connections, the site is assumed with a constant trackbed stiffness of 40 kN/mm/se, the connections are kept as rigid and voids are applied in 4 locations of the crossover: underneath the crossing leg, under the crossing nose and the two bearers after (bearers 45, 47, 48 and 49). Note that these locations are the ones where the biggest displacements were observed in the second instrumentation of the site in 2019. A gap of 3 mm is assumed on 6ft side on the Down track, following the distribution underneath the bearer discussed in Chapter 5.

Figure 6.9 shows the composite stiffness obtained for a trackbed stiffness of 40 kN/mm/se and a load of 100 kN on each rail of the Down track. The gap completely eliminates the local increase of composite stiffness that was due to elements of the track superstructure around the crossing (check rails, longer bearers), and is now replaced with a local soft spot. Although the gap was only applied below the 6ft side, it affects both sides on the composite stiffness. The 6ft and cess sides show similar composite stiffness with the presence of the gap, and this counteracts the previously observed roll of the track towards the cess in Figure 4.3. This change of behaviour was also observed on the site measurements discussed in Chapter 5. In 2016, a roll of the track towards the cess side was observed, showing higher displacements than the 6ft, while, in 2019, the measurements have shown the opposite behaviour with higher displacements on the 6ft side.

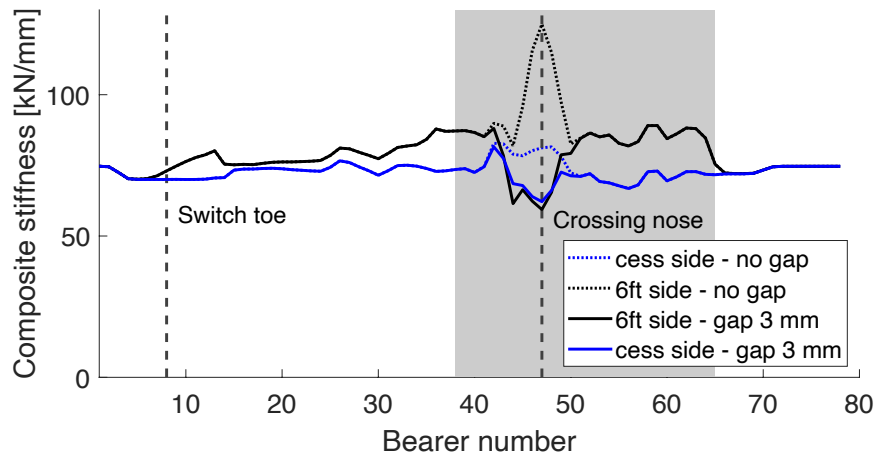


Figure 6.9. Composite stiffness considering constant trackbed stiffness equal to 40 kN/mm and a series of gap of 3 mm.

Figure 6.10 shows the vertical contact forces for the front wheelset of the Mark IV coach at 50 m/s. The presence of a void does not show a significant effect on the contact forces, which was already discussed for the variation of trackbed stiffness. The gap has the same effect as considering a lower trackbed stiffness, shifting the peak and showing a reduction of 5 %. The second peak observed has a more significant reduction of 38 %. These differences are quite small, again showing that the main influence for the wheel/rail contact dynamic load is the crossing element and not the local track support.

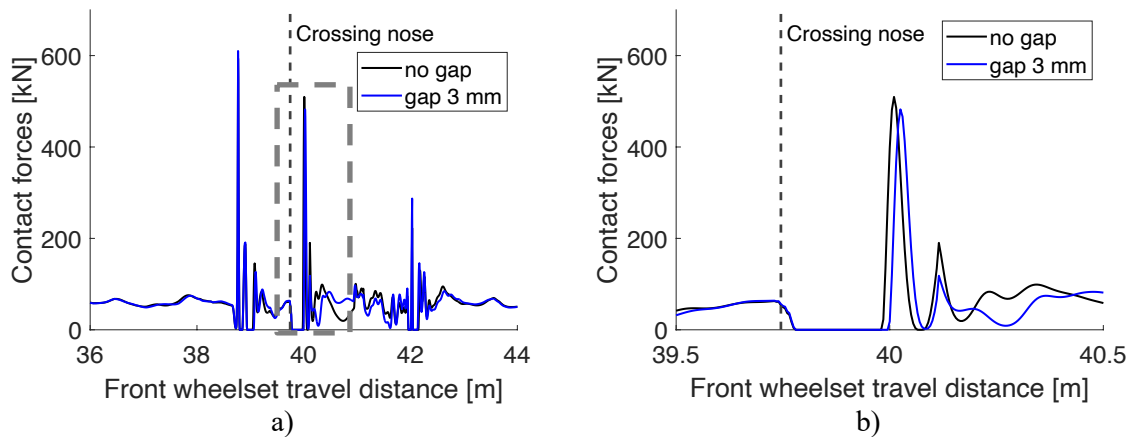


Figure 6.10. Vertical contact forces from the front wheelset of Mark IV coach on the 6ft side considering a constant trackbed stiffness equal to 40 kN/mm and a gap of 3 mm.

The void is expected to affect more the substructure, mainly the displacement and deformation of the bearers, ballast forces and the forces and torques transmitted to the bearer connection. Figure 6.11 shows the effect of a gap of 3 mm on the bearer displacements and

ballast forces underneath the rails of both sides obtained from the simulation of the Mark IV coach running at 50 m/s. An increase in bearer displacements is observed on the 6ft and cess sides. Under the crossing nose, there is an increase of 0.79 mm and 0.24 mm for the 6ft and cess side, respectively, when compared to the non-voided track. This increase is quite small compared to the size of the voids considered. In this area and due to the higher dynamic loads happening on the crossing element, the initial roll of the track towards the cess is reversed and now the bearer bends and rolls towards the 6ft. The increase of deflections on the 6ft side is not enough to reach the gap value, meaning that no force is transmitted to the ballast and it is observed in Figure 6.11 b). The axle load is distributed to adjacent bearers through the rail bending properties and to the remaining bearer where no gap is considered. The bearer just before the nose will probably degrade as well and develop some void pretty quickly under the increased load observed in Figure 6.11 b), therefore the gap will develop fast over several bearers. In the long-term evolution, the gap will spread over an area like it is suspected in the 2nd site measurements. A model to predict settlement would help to test these assumptions.

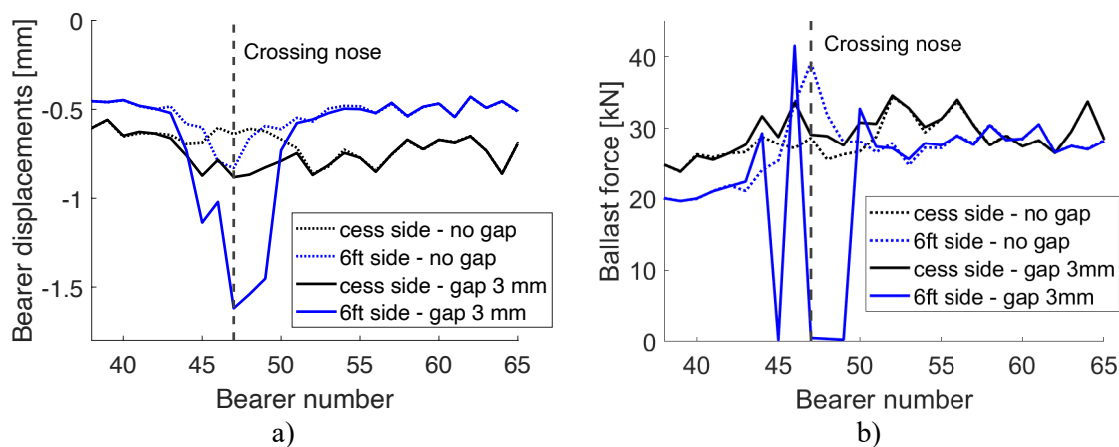


Figure 6.11. Effect of voided sleepers on a) bearer displacements and b) ballast forces.

The increase of displacements on the 6ft side will increase the bearer bending on that side, which will surely increase the stresses on the connection between bearers. Figure 6.12 shows the effect of the gap underneath the 6ft side of the Down track on the maximum reaction forces and torques of the bearers connections. The void underneath the bearer increases the force transmitted to the bearer connection by about 11 % and the torque by 67 %, in the case of bearer 47 where a higher reaction force is observed. If this increase of force and torque reaches the maximum resistance of the connection, it would lead to its degradation. NR

reported that a common failure from this type of connection is the bolts breaking underneath their head from the shear forces on the metal plate. On site, a location with loose bolts was observed. These failures may allow the connection to rotate more and allow the two bearers to separate.

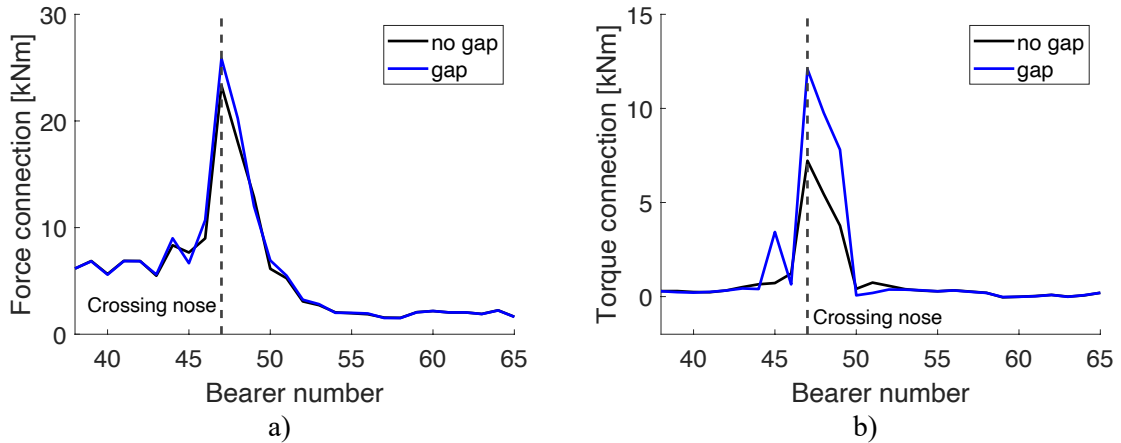


Figure 6.12. Effect of voided bearers on the reaction a) forces and b) torques of the bearer connections.

It is difficult to simulate the whole degradation process of the crossover, which depends on the location of voids and the degradation state of the connection. From the previous chapter, possible causes for the measured displacements were identified and the effect of each assumption was demonstrated. In this chapter, homogeneous support and the connection in good condition have been considered. Figure 6.13 compares the composite stiffness underneath each rail for the case of the homogeneous track and the track calibrated in chapter 5. General ‘noise’ or variability in the composite stiffness from the calibrated case is observed, showing high variability in ballast support conditions throughout the site. A significant lowering of the composite stiffness is observed in the areas where voided sleepers have been assumed. There is a reverse behaviour observed compared to the initial state considered (constant stiffness and rigid connections), whereby the 6ft side on the longer bearers shows higher displacements and a lower composite stiffness than cess side. The local increased composite stiffness due to the switch and crossing elements is no longer visible and the crossing panel effective composite stiffness appears lower on average than the rest of the crossover and plain line. There are also local soft spots observed, which developed around other areas of the crossover and can be caused by local defects on the rail, like welds or ballast problems like ballast migration or compaction/voids.

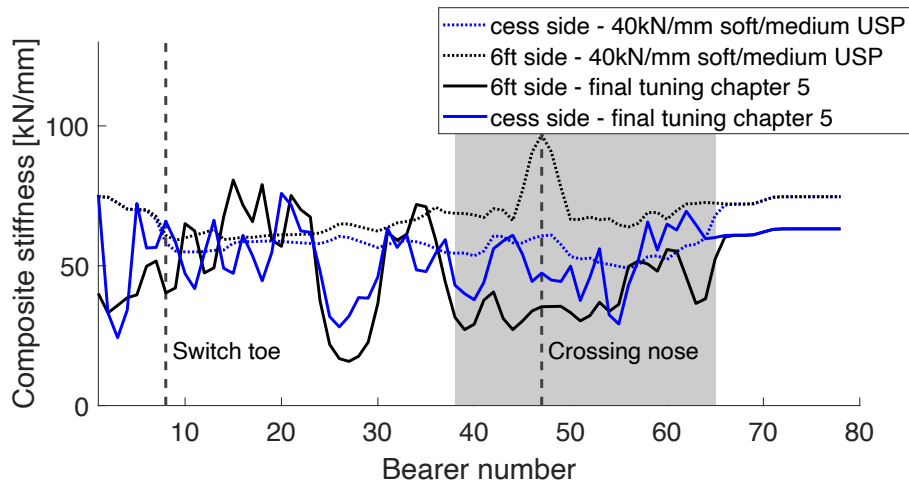


Figure 6.13. Composite stiffness considering constant trackbed stiffness equal to 40 kN/mm and a gap of 3 mm.

6.4 ALTERNATIVE DESIGN TO THE LONG BEARER CONNECTION

The railway crossover studied in this work was built using a NR approved design for a joint, which corresponds to a bent metal shroud with the intention of connecting the two bearers semi-rigidly. This section aims to determine what bearer connection perform better and presents an analysis of two alternative designs, the pinned joint and the sandwich joint.

6.4.1 Pinned joint

The pinned (or pinned–pinned) joint, shown in Figure 6.14, prescribes mainly the relative lateral displacement between bearers, allowing free relative vertical and roll motions. Therefore, in the crossover model, the pinned joint is modelled with a bushing element that only reacts to lateral relative motions, leaving both vertical and rotation movements free.



Figure 6.14. Pinned-pinned joint.

The bearer movements at the 6ft and cess sides for the pinned joint and the original case are shown in Figure 6.15. The major difference is observed on the 6ft side, namely, around the crossing element, where the pinned joint allows a displacement 27 % higher than the rigid joint for the bearer 47. It is worth noting that the difference of displacement of the bearers before the crossing nose is higher than after, due to the bearers on the Down track being shorter between 38 and 44.

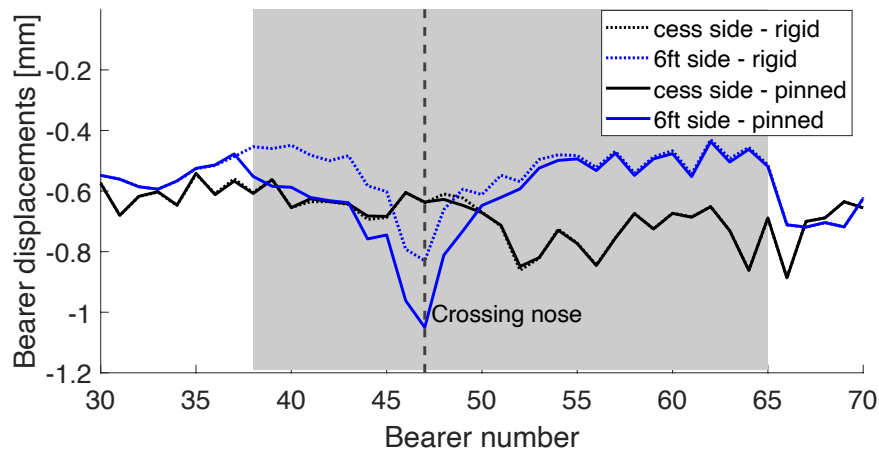


Figure 6.15. Maximum bearer displacements for Mark IV coach considering the rigid connection and the pinned-pinned connection.

Figure 6.16 shows the deformed shape of each bearer for the instant of the simulation where the maximum displacement under the 6ft rail is observed. Due to the pinned joints, the bearers of the Up track are more isolated from the track load applied to the Down track. Before the crossing, the track no longer bends towards the cess side and instead the bearer shows similar displacements on both sides, cess and 6ft. The bearers at the crossing show bending towards the inside of the track (6ft side) due to the increased dynamic loads in that area. After the crossing nose, the bearers start rotating again towards the cess side, since the bearers are longer and no longer centred in the middle of the down track like the bearers before bearer 43.

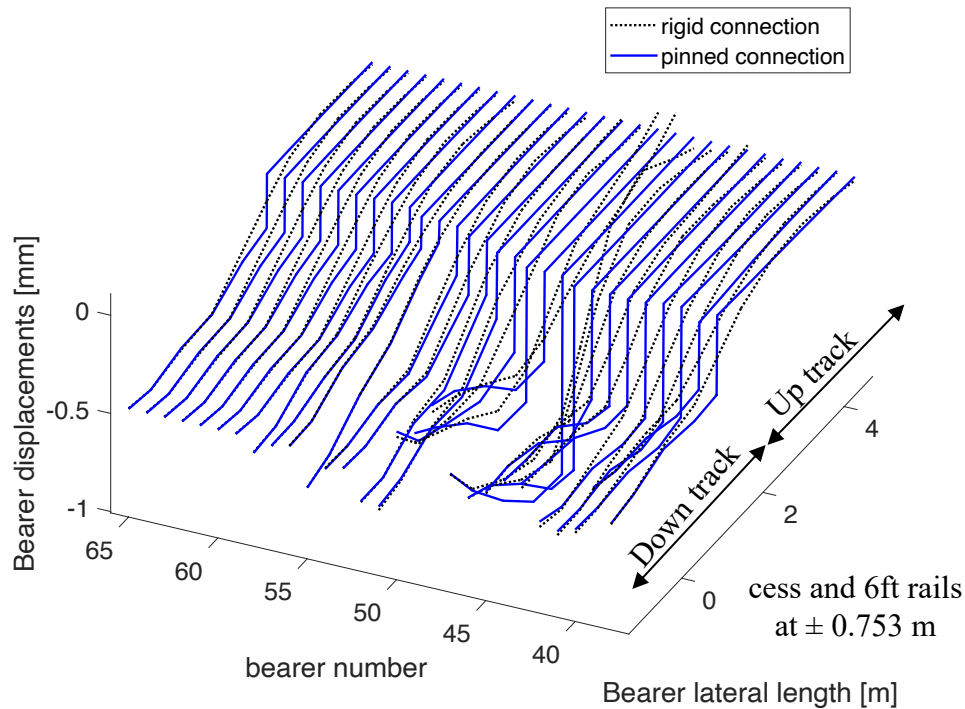


Figure 6.16. Bearer deformation for the maximum displacement under the 6ft rail caused by the passage of Mark IV coach considering the rigid connection and the pinned connection.

Taking the bearer underneath the crossing nose as an example, Figure 6.17 shows the bearer deformation for the two types of joint. The free connection makes the long bearer dissociated which leads to a different deformation/deflection and higher displacements under the 6ft and towards the central area of the double track. At the same time, the bearer of the Down track is disengaged with the pinned connection. Although the pinned connection may not get degraded from the increase of displacements on the 6ft side or possible voids, allowing to deflect this much from the start may also lead to voids developing faster and even affecting the track level.

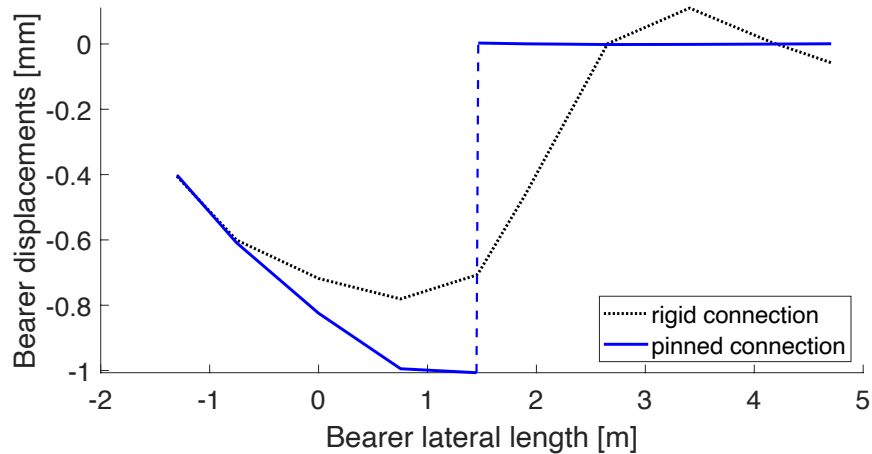


Figure 6.17. Deformation of the bearer underneath the crossing nose using the rigid and pinned-pinned connections.

6.4.2 Sandwich joint

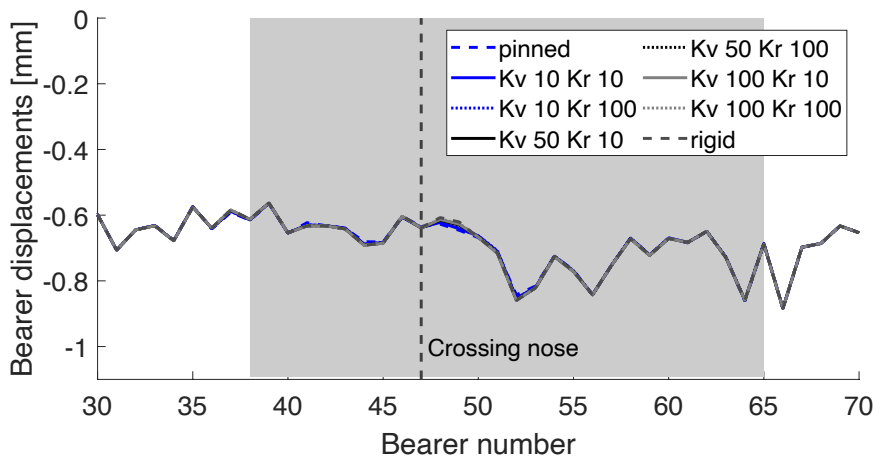
This joint restrains the gauge between the two tracks and has a “sandwich” like design with resilient layers to limit the transmission of high frequency vibration between bearer elements, as shown in Figure 6.18. This component is likely to be less rigid than a metal shroud. Since no data is available about the resilient layers used on this type of connection, this connection will be used to test different combinations for the vertical and rotational stiffnesses of the bushing used to connect the bearers from the two tracks. Three values were adopted to the vertical stiffness, namely 10, 50 and 100 MN/m and two values were used to the rotational stiffness, 10 and 100 MNm/rad compared to 500 MN/mm and 300 MNm/rad for the metal shroud design.



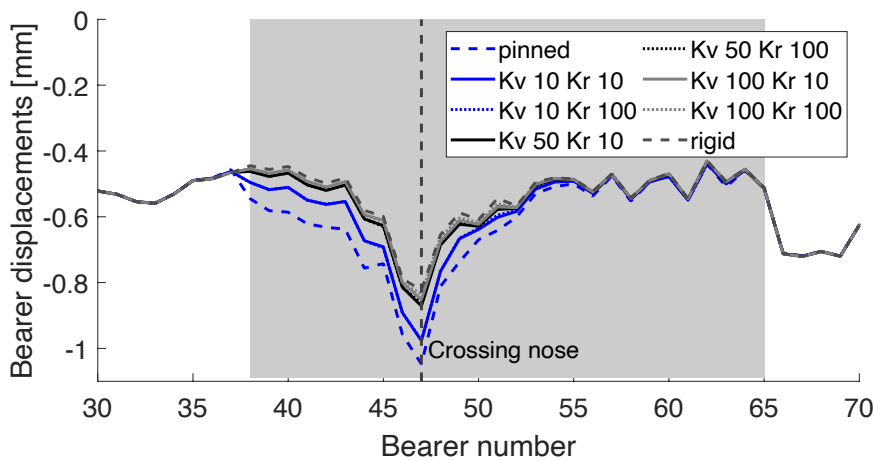
Figure 6.18. Sandwich type joint.

Figure 6.19 compares the bearer displacements underneath both rails for all different combinations of pad parameters on the connection and also compares with the rigid and

pinned joints. The type of connection has almost no influence on the cess side. On the 6ft side, the pinned connection has the biggest displacements and the rigid connection the smallest, as expected. The values adopted for the sandwich connection show results between the other rigid and pinned connections. The results for a pad with 100 MN/m are very close to the rigid connection and the 50 MN/m not far off. The results for a 10 MN/m are close to the middle result between the rigid and pinned joints.



a)



b)

Figure 6.19. Maximum bearer displacements for Mark IV coach considering sandwich joint and for a) cess side; b) 6ft side.

Figure 6.20 shows the deformed shape of the bearer underneath the crossing nose where the highest displacements occur below the 6ft rail. The rotational stiffness does not affect the displacements underneath the 6ft rail (placed at 0.753 m), but affects the area of the connection at 1.3 m, in particular the bearer of the Up track (on the right of the connection

in Figure 6.20). Additional values other than those tested would lead to more result curves between the rigid and pinned joint curves.

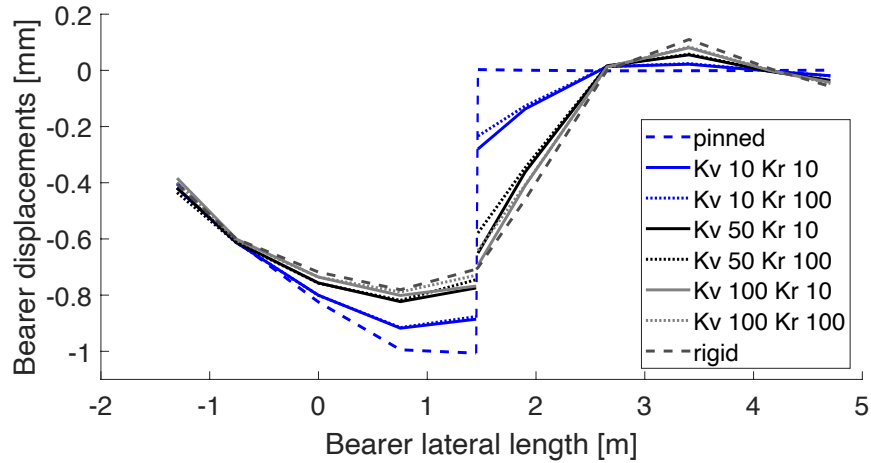


Figure 6.20. Deformation of the bearer underneath the crossing nose for the sandwich joint.

Looking at all these results, it would be easy to assume that the rigid connections seem to perform better for this particular turnout and the positioning on the track, i.e. in the middle of the diverging route. The rigid joint is the connection that leads to less displacements, making the bearer act as one, having more area to transfer the load to the ballast. But, as seen in previous chapters, this connection is also susceptible to degradation mechanisms under all the forces it is subjected to. Figure 6.21 proves this, where the rigid connection is the one with the highest forces and torques applied on it. The softer the connection joint is, the lower the forces and torques applied.

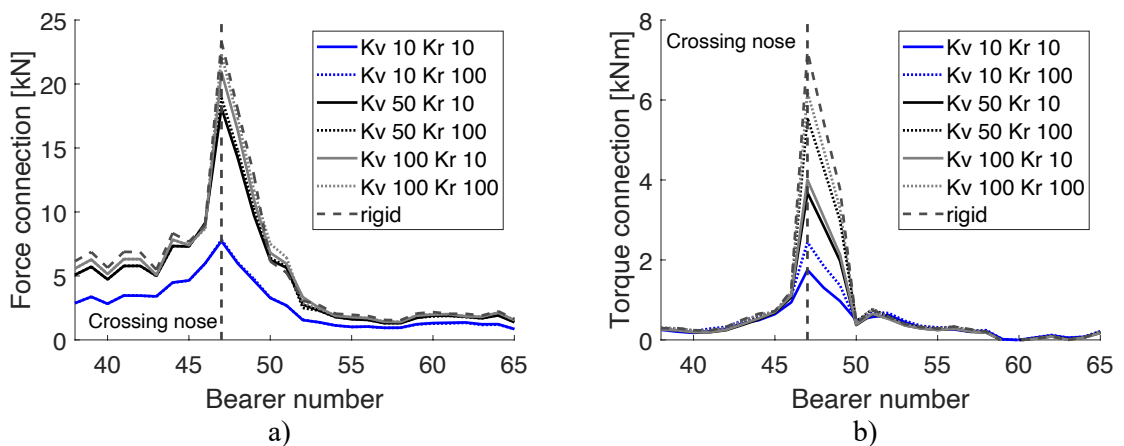


Figure 6.21. Effect of the connection stiffness properties on the a) forces and b) torques transmitted to the connection.

Figure 6.22 shows the ballast forces on the 6ft side of the Down track when considered different vertical and rotational stiffness on the bearer connection. The rotational stiffness has nearly no influence on the results, while the vertical stiffness has a maximum increase of force of around 5%. When compared to the bearer displacements or the forces and torques on the connection, the ballast forces seem to affect only the local area after the crossing nose, which may be related to the higher contact forces observed in this area of the load transferring from the wing rail to the crossing nose that mobilise the connection.

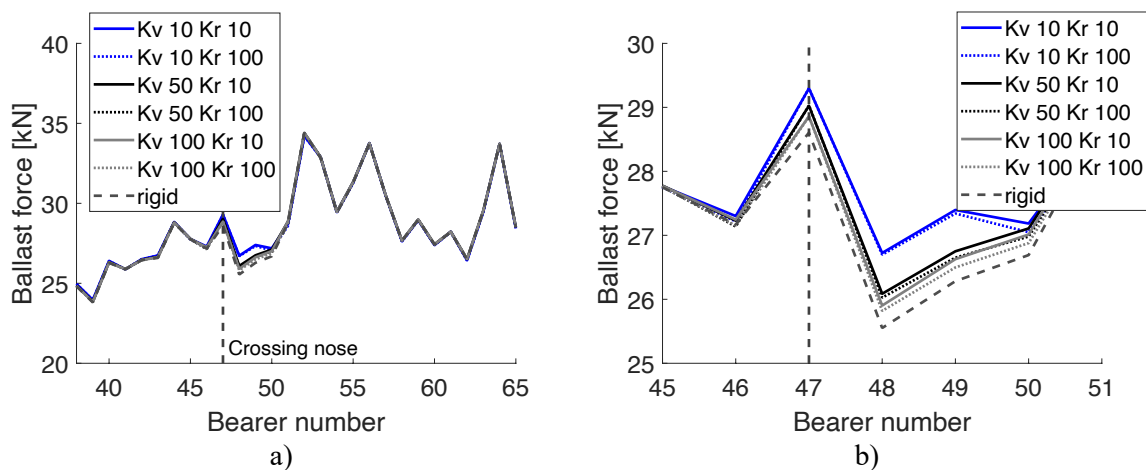


Figure 6.22. Effect of the connection stiffness properties on the ballast force on the 6ft side of the Down track. b) shows a zoom around the crossing nose.

6.5 CONCLUSIONS

In this chapter, two different trackbed stiffnesses were considered and compared to better understand how they relate to the other components of the track. The higher trackbed stiffness led to the highest composite stiffness and the lowest displacements, as expected. However, the highest stiffness enlarged the dynamic effects and the resulting ballast force due to the wheel interaction with the upper structure, namely in the crossing and switch elements. The contact forces do not seem to be affected much by the different trackbed stiffnesses adopted and are mainly led from the kinematics of the wheel and rail contact. The ballast forces are highly affected by the wheel-rail contact forces and show an increase of up to 85 % on the bearer below the crossing nose compared to five sleepers before. Although the trackbed stiffness did not show much influence on the forces and torques transmitted to the connection, the local impact loads on the crossing do have a huge impact on the forces transmitted to those connections.

The choice of installing two different types of Under Sleeper Pads on the site was assessed. The USP leads to a substantial reduction in the composite stiffness, mainly on the cress side, when compared to the areas of the track with no USP installed. This is somehow contradictory to the initial idea of a smoother stiffness transition from the different areas of the crossover. The ballast forces see a reduction on average of 20 % and 22 % for the load transfer area on the switch and crossing, respectively. From the results obtained here, the USPs installed do not offer an ideal smoothing of the track stiffness and a better optimum might yet to be achieved. However, this does not tell the whole story since the model is not able to reproduce the benefits that the USP has, such as better distribution of the load and reduced stress on the ballast particles.

The effect from the presence of voids underneath the bearers of the crossover was also studied. A gap of 3 mm was assumed in four bearers underneath the crossing element. The gap completely eliminated the local increase of composite stiffness that was due to all the elements from the superstructure and replaced it with a local soft spot. Although the voided bearers did not affect the contact forces, they led to an increase of bearer displacements in the surrounding area of the gap and an increase of forces and mainly torques on the bearer joints. If this increment on forces reaches the maximum strength of the connection, it may lead to a faster degradation due to fatigue.

At the end of this chapter, two different types of connection were studied in addition to the NR rigid joint. The pinned joint, which permits some difference in level between the joined tracks, while retaining the gauge between them and a sandwich type joint, which has resilient layers to limit the transmission of high frequency vibration between bearer elements. The last one, since there was no data available on the type of pads used, a combination of values for the vertical and rotational stiffness were adopted to see their influence. The pinned joint leads to higher displacements on the 6ft side compared to the rigid joint as expected, with the maximum value occurring under the crossing nose. Since the bearers get longer throughout the turnout, the deformed shape of the bearers changes along the crossing panel. The values adopted for the sandwich type joint showed deformation falling between the one obtained from the rigid connection (the lowest) and the one obtained from the pinned connection (the largest). Although, the rigid connection is the one that deflects the least, it is also the one that receives the highest load and torque. These joints have not been designed to sustain the peak loads observed here at the crossing nose, but

instead, they were designed under normal load conditions. This may explain why they fail around this area.

In summary, this chapter enables to determine mitigation measures to reduce extend the life cycle of the turnout infrastructure. The USPs can give an attenuation on the ballast forces which can be beneficial to the long-term behaviour of the site. The rigid connection seems to be a good solution if working properly, as it leads to the lowest bearer displacements and ballast forces, but it also creates the highest forces on the connection. In the case of voids developing underneath the bearer, the forces and torques applied to the connection will increase, compromising its original behaviour. Further studies are required to validate these results and better conclude which design performs better. The NR design needs a proper inspection to guarantee the connection performs as intended and no bolts are loose or broken. This would raise the cost in the long-term of using them. It is still a better solution than requiring a full renewal of the site due to the failure of some connections and the increase of ballast settlement.

The discrete track model created in VI-Rail allowed studying several key components defining the overall behaviour in a crossover, which was not possible to achieve with simpler track models. Only one type of crossover was studied here, where the connection is placed between the rails of the diverging route. Other layout arrangements exist where the connection changes location on the track and it would be interesting to study these using the same approach as the failure of those connections have been known to be partly responsible for derailment in one particular instance in the UK [109] and many more failures have been reported over the network. The advanced model developed in this thesis allows to get information about ballast forces and potentially stresses estimate which could be used to study the long-term behaviour of the crossover, coupling with long term settlement equations in an iterative process [110].

7 CONCLUSIONS AND FURTHER WORK

7.1 CONCLUSIONS

A detailed review of vehicle and track dynamic models, including those that account for the vehicle-track interaction is given in Chapter 2, with particular focus given to the studies related to S&Cs. The majority of the work found in the literature lacks in considering the track support stiffness and rail properties variability at a S&C while MBS software. Some authors consider the track support variability, but use software created in-house, usually based on finite element methods with simplified or less robust wheel-rail contact routines or vehicle models. This thesis extends the methodology proposed in [4], which proposed a discrete track model to represent plain track and extend it to S&Cs.

In chapter 3, different track models are compared to understand their advantages and disadvantages at studying S&Cs. The track models considered are the continuously supported track model and three discretely supported track models, two built in VI-Rail and another *in-house* named VTI, which is implemented in MATLAB. Two distinct methodologies are adopted to build the discretely supported track in VI-Rail, the first directly modelled inside VI-Rail using massless beam element based on Timoshenko, and a second approach where the rail is modelled from modal data extracted from the FE software ANSYS. A benchmark study that considers the simulations of a wheelset and a vehicle negotiating a plain line track under the excitation given by a vertical track irregularity is presented. The track irregularity considered in this study combines a medium wavelength irregularity similar to a weld with a short wavelength irregularity to produce a high frequency impact force. All models show a good agreement between all the results compared, including wheel-rail contact forces, and displacements of the bearer and wheelset. The maximum difference between peak values is around 12 % except for the wheel displacement for the case of the short wavelength irregularity, which shows differences up to 33 %. The continuous track model is a good choice to evaluate vehicle dynamics and is computationally efficient. Yet, it cannot simulate the change of rail properties or take into consideration the full layout of a S&C and study discrete events like bearers with different lengths or being badly supported. The discretely supported track model using the modal data from ANSYS

only worked when considering all the modes up to 3kHz, which made it run 20 times slower than the model using ADAMS beam. The discretely supported track model using ADAMS beam is to be the most versatile of the three models in VI-Rail.

A UK site with Under Sleeper Pads (USPs) was selected as a case study. The discretely supported track model is then used to build the railway crossover and all the steps to build the model are described in Chapter 4. Two measurement campaigns, one in 2016 and the other in 2019 were carried out on this site, using geophones to measure bearer velocities which were integrated to get bearer displacements. The first campaign concentrates on two areas of the site, one on the switch panel and the other on the crossing panel, with every 2 bearers on the cess side and a few bearers on the 6ft side being measured. The trackbed stiffnesses of VI-Rail model is calibrated against the site measurements with the support of another *in-house* VTI model partly developed within the same project supporting this thesis by Grosso [5]. The trackbed stiffnesses are used as input to both models and a good agreement between the two models is achieved at the switch panel and expectable differences are observed at the crossing panel due to the more complex VI-Rail model, which includes the contribution from the adjacent track to the overall system stiffness.

The data obtained from the second campaign showed an increase in displacements that most likely indicate the existence of voided bearers. From observations in situ and photos taken from the site, it was possible to assume that some of the connection devices between bearers of the two tracks were damaged. Therefore, the track model is adjusted by including flexible bearers (introduced in Section 4.4) and by using non-linear force elements to model the varying trackbed stiffness as well as voids underneath the bearer (presented in Section 5.2.3). A methodology to calibrate the evolved trackbed stiffnesses is proposed and implemented in VI-Rail and MATLAB. The level of displacements measured is achieved not only by reducing the trackbed stiffness of each bearer, but also by considering voids under the bearers, by removing the connection from bearers where loose bolts were spotted and by considering some level of flexibility at the other connections rather than assuming they are rigid as intended in nominal conditions. Finally, a reduction in the trackbed stiffness of the Up track was included to simulate the hypothesis of voids being present at the adjacent track. The average error of the bearer movements is reduced by 20 % more when considering all the model changes besides the initial calibration of the trackbed stiffness, reaching a final average error of 12 %. From all these changes, the voided bearers and the low stiffness of

the connection are the ones that lead to the biggest increase of the displacements. The incremental process of the model proposed in Chapter 5 was essential to represent the degraded states and hence to obtain a good match with the measured bearer displacements. Also, the data obtained from the two campaigns enables the assessment of the site condition due to the three years of traffic and how the degradation occurs, which can be translated to similar S&Cs. An early intervention correcting the ballast level and replacing loosed bolts from the bearer connections are recommended to mitigate the degradation of the S&C and further expand any future renewal of the site.

The model proposed and calibrated in Chapters 4 and 5, is used to study the non-homogeneous stiffness at S&Cs in Chapter 6. Two different trackbed stiffnesses are considered and compared to better understand how they interact with the other components of the track. The higher trackbed stiffness leads to the highest composite stiffness and the lowest displacements, as expected, while the highest composite stiffness is observed at the crossing element. The areas with an amplification of the contact forces due to the load transfer on the switch and crossing panels are also the areas where a significant increase in ballast forces and the forces transmitted to the connections is observed. The amplification on the ballast forces at the crossing panel is up to 85 % on the bearer below the crossing nose compared to five sleepers before and can result in increased ballast settlement and explains the voided bearers seen in these areas. The force and torques transmitted to the connection between bearers are increased up to four times around the crossing nose, which may be the reason for the failures observed in situ since these devices were not designed for such loads. The model shows how each track component, from the S&C components to the longer bearers, affect the track composite stiffness.

The choice of installing two different types of Under Sleeper Pads on the site is also assessed in Chapter 6. The USPs prove to not offer an ideal smoothing of the track stiffness, but they eliminate the local increase of composite stiffness observed at the crossing panel, replacing it with a local soft spot. The USP leads to a substantial reduction of the composite stiffness on both sides but is more noticeable on the cess side. The ballast forces have decreased by 20 % under the crossing nose and 22 % around the load transfer at the switch panel. Although the voided bearers do not affect the contact forces, they lead to an increase of bearer displacements that also increases the reaction forces of the bearer connection. This increment in forces may lead to faster degradation of the connection under fatigue.

On the second campaign and from observations *in situ* it was identified voided bearer and broken bearer connections. To understand if the two occurrences are connected, a homogeneous trackbed stiffness is assumed, while applying a gap under certain bearers below the crossing. The gap leads to doubling the bearer displacements, increasing the forces and torques transmitted to the connection by 11 % and 67%, respectively, which accelerates the degradation of the bearer connections. An increase of 30% on the ballast forces is observed for one of the adjacent sleepers, which can lead the void to spread across more bearers.

Two European designs for the connection between bearers are studied and compared with the UK NR design. The pinned joint, which permits some difference in level between the joined tracks, while retaining the gauge between them and a sandwich type joint with resilient layers to limit the transmission of high frequency vibration between bearer elements. The pinned joint leads to higher displacements on the 6ft side compared to the rigid joint, as expected, with the maximum value occurring under the crossing nose. For the sandwich type joint, a combination of values for the vertical and rotational stiffness is adopted to see their influence. The values lead the bearer deformation to fall between the one obtained from the rigid connection (the lowest) and the one obtained from the pinned connection (the largest). Barely any effect is observed on the ballast forces due to the different connection types. The two European designs lead, in general, to higher displacements which can accelerate the development of voids, but they lead to less stresses on the connection, increasing itself, thus increasing their longevity.

The detailed S&C model proposed in this thesis represents the main novelties of this work. The model is developed entirely inside a MBS software, without requiring any external FE software. This gives access to robust wheel-rail contact algorithms and a library of detailed and validated vehicle models. The track model is versatile enough to build a complex S&C layout and still have reasonable simulation times. The S&C model developed in this work intended to represent a UK railway crossover. The model is calibrated against site measurements and some level of degradation of the S&C is considered so that a good agreement is achieved. Some of these degradation mechanisms would not be possible to simulate with a simpler model that does not consider all the lines, bearer lengths and connections. Creating such a complex track model, closer to reality, allows to study particular elements of the track, that would not be possible with the simpler model, such as

the long bearers and their connection. Here, different designs for the connection are studied, but it can be used further to study other designs and help to define the best design and location for different S&Cs layouts.

7.2 FUTURE WORK

This work focused mainly on the track dynamics as a detailed model of a railway crossover has been developed. Since the multibody formulation is used to develop the track model, the vehicle can be modelled with great details and therefore can be the focus of extended analysis from the vehicle perspective. For example, determining causes of a derailment in a track under defective or degraded S&C asset, which is where it is more likely to occur, or designing the vehicle suspension for a smoother turnout negotiation, that is, minimized impact load on the track, are other examples of application.

The methodology used in this thesis is recommended to build a numerical model of a different S&C, including following the modelling decisions adopted in this work, which allowed to model bearers at the right position, rails with variable cross-section, voids and USPs. It would be interesting to study other layout arrangements using the same approach as the failure of those connections have been known to be partly responsible for derailment in one particular instance in the UK.

The numerical simulations presented in this work enable predicting the forces transmitted to the ballast. Extending this work to predict also the stresses, enables to study of the long-term behaviour of the crossover, coupling with long term settlement equations in an iterative process.

Voids below the bearers have been identified in the site measurements, but not fully validated. Although care has been taken in their estimation, measuring the magnitude of the voids, with void-meters for instance, would not only simplify the validation procedure but also improve the accuracy of the numerical model.

The methodology here allowed to calibrate a railway crossover model against site data available. This could be extended to other fully instrumented sites and other types of data, taking full advantage of the detailed model built in VI-Rail.

Finally, the methodology implemented in VI-Rail could be used to look at innovative track superstructure designs, such as slab tracks or even transition zones.

REFERENCES

1. Lichtberger, B., Track Compendium: Formation, Permanent Way, Maintenance, Economics. 2005: Eurailpress.
2. Johansson, A., B. Pålsson, M. Ekh, J.C.O. Nielsen, M.K.A. Ander, J. Brouzoulis, and E. Kassa, Simulation of wheel–rail contact and damage in switches & crossings. *Wear*, 2011. 271(1-2): p. 472-481.
3. Kassa, E., C. Andersson, and J.C. Nielsen, Simulation of dynamic interaction between train and railway turnout. *Vehicle System Dynamics*, 2006. 44(3): p. 247-258.
4. Bezin, Y., An Integrated Flexible Track System Model for Railway Vehicle Dynamics, in Department of Engineering & Technology. 2008, Manchester Metropolitan University.
5. Grossoni, I., L.M. Le Pen, P. Jorge, Y. Bezin, G.V. Watson, D. Kostovasilis, and W. Powrie, The role of stiffness variation in switches and crossings: Comparison of vehicle–track interaction models with field measurements. *Proceedings of the Institution of Mechanical Engineers, Part F: Journal of Rail and Rapid Transit*, 2019. 0(0): p. 0954409719892146.
6. Jorge, P., Y. Bezin, I. Grossoni, and S. Neves. *Modelling Track Flexibility in Turnouts Using MBS Approach*. 2020. Cham: Springer International Publishing.
7. Esveld, C., *Modern Railway Track*. Second Edition ed. 2001, Delft University of Technology.
8. Selig, E.T. and J.M. Waters, *Track geotechnology and substructure management*. 1994: Thomas Telford.
9. Standardization, E.C.F., BS EN 13848-1:2019 Railway applications. Track. Track geometry quality. Characterization of track geometry. 2019.
10. Ribeiro, C., *Transições aterro-estrutura em linhas ferroviárias de alta velocidade: análise experimental e numérica*. 2012, Faculty of Engineering of University of Porto Porto, Portugal.
11. Bezin, Y., D. Farrington, C. Penny, B. Temple, and S. Iwnicki, The dynamic response of slab track constructions and their benefit with respect to conventional ballasted track. *Vehicle System Dynamics*, 2010. 48(S1): p. 175-193.

12. Grossoni, I., A.R. Andrade, Y. Bezin, and S. Neves, The role of track stiffness and its spatial variability on long-term track quality deterioration. Proceedings of the Institution of Mechanical Engineers, Part F: Journal of Rail and Rapid Transit, 2018: p. 0954409718777372.
13. Le Pen, L., D. Milne, D. Thompson, and W. Powrie, Evaluating railway track support stiffness from trackside measurements in the absence of wheel load data. Canadian Geotechnical Journal, 2016. 53(7): p. 1156-1166.
14. Sussman, T.R., W. Ebersöhn, and E.T. Selig, Fundamental Nonlinear Track Load-Deflection Behavior for Condition Evaluation. Transportation Research Record, 2001. 1742(1): p. 61-67.
15. Standardization, E.C.F., BS EN 13674-1:2011 Railway applications — Track — Rail, Part 1: Vignole railway rails 46 kg/m and above. 2017, British Standards Institution (BSI).
16. Pålsson, B., Optimisation of railway switches and crossings. 2014, Chalmers University of Technology.
17. Cope, G.H. and P.W. Institution, British Railway Track: Design, Construction and Maintenance. 1993: Permanent Way Institution.
18. Wan, C., Optimisation of vehicle-track interaction at railway crossings. 2016, Delft University of Technology.
19. Pålsson, B.A., Optimisation of railway crossing geometry considering a representative set of wheel profiles. Vehicle system dynamics, 2015. 53(2): p. 274-301.
20. CAPACITY4RAIL, Deliverable 13.2: Innovative concepts and designs for resilient S&Cs (intermediate) 2016.
21. CAPACITY4RAIL, Deliverable 13.3: Innovative concepts and designs for resilient S&Cs (final) 2017.
22. Flores, P., Concepts and Formulations for Spatial Multibody Dynamics. 2015: Springer International Publishing.
23. Weidemann, C., State-of-the-art railway vehicle design with multi-body simulation. Journal of mechanical systems for transportation and logistics, 2010. 3(1): p. 12-26.
24. Choros, J. and G. Adams, A Steadily Moving Load on an Elastic Beam Resting on a Tensionless Winkler Foundation. Journal of Applied Mechanics, 1979. 46: p. 175.

25. Jezequel, L., Analysis of the critical speeds of a moving load on an infinite periodically supported beam. *Journal of Sound and Vibration*, 1980. 73(4): p. 606-609.
26. Kenney, J., Steady-state vibrations of beam on elastic foundation for moving load. *Journal of Applied Mechanics-Transactions of the ASME*, 1954. 21(4): p. 359-364.
27. Mathews, P.M., Vibrations of a beam on elastic foundation. *ZAMM-Journal of Applied Mathematics and Mechanics/Zeitschrift für Angewandte Mathematik und Mechanik*, 1958. 38(3-4): p. 105-115.
28. Knothe, K.L. and S.L. Grassie, Modelling of railway track and vehicle/track interaction at high frequencies. *Vehicle system dynamics*, 1993. 22(3-4): p. 209-262.
29. Sun, Y.Q. and M. Dhanasekar, A dynamic model for the vertical interaction of the rail track and wagon system. *International Journal of Solids and Structures*, 2002. 39(5): p. 1337-1359.
30. Bathe, K.J., *Finite Element Procedures*. 2006, Klaus-Jurgen: Prentice Hall.
31. Vale, C., *Influência da qualidade dos sistemas ferroviários no comportamento dinâmico e no planeamento da manutenção preventiva de vias de alta velocidade*. 2010, Faculty of Engineering of University of Porto: Porto, Portugal.
32. Biggs, J., *Introduction to structural dynamics*. 1964: McGraw-Hill College.
33. Frýba, L., *Vibration of solids and structures under moving loads*. 3rd edition ed. 1999, London: Thomas Telford.
34. Majka, M. and M. Hartnett, Effects of speed, load and damping on the dynamic response of railway bridges and vehicles. *Computers & Structures*, 2008. 86(6): p. 556-572.
35. Ribeiro, D., R. Calçada, R. Delgado, M. Brehm, and V. Zabel, Finite-element model calibration of a railway vehicle based on experimental modal parameters. *Vehicle System Dynamics*, 2013. 51(6): p. 821-856.
36. Neves, S.G.M., P.A. Montenegro, A.F.M. Azevedo, and R. Calçada, A direct method for analyzing the nonlinear vehicle–structure interaction. *Engineering Structures*, 2014. 69: p. 83-89.
37. Montenegro, P.A., S.G.M. Neves, R. Calçada, M. Tanabe, and M. Sogabe, Wheel–rail contact formulation for analyzing the lateral train–structure dynamic interaction. *Computers & Structures*, 2015. 152: p. 200-214.

38. Grossoni, I., S. Iwnicki, Y. Bezin, and C. Gong, Dynamics of a vehicle-track coupling system at a rail joint. *Proceedings of the Institution of Mechanical Engineers, Part F: Journal of Rail and Rapid Transit*, 2015. 229(4): p. 364-374.
39. Nielsen, J.C.O., High-frequency vertical wheel–rail contact forces—Validation of a prediction model by field testing. *Wear*, 2008. 265(9): p. 1465-1471.
40. Di Gialleonardo, E., F. Braghin, and S. Bruni, The influence of track modelling options on the simulation of rail vehicle dynamics. *Journal of Sound and Vibration*, 2012. 331(19): p. 4246-4258.
41. Antunes, P., H. Magalhães, J. Ambrósio, J. Pombo, and J. Costa, A co-simulation approach to the wheel–rail contact with flexible railway track. *Multibody System Dynamics*, 2019. 45(2): p. 245-272.
42. Costa, J., P. Antunes, H. Magalhães, J. Pombo, and J. Ambrósio, A novel methodology to automatically include general track flexibility in railway vehicle dynamic analyses. *Proceedings of the Institution of Mechanical Engineers, Part F: Journal of Rail and Rapid Transit*, 2020(<https://doi.org/10.1177/0954409720945420>).
43. Eickhoff, B., L. Mazzola, Y. Bezin, G. Tucker, H. Stradtman, A. Haigermoser, H. Chollet, and J. Landais, Track loading limits and cross-acceptance of vehicle approvals. *Proceedings of the Institution of Mechanical Engineers, Part F: Journal of Rail and Rapid Transit*, 2015. 229(6): p. 710-728.
44. Telliskivi, T. and U. Olofsson, Contact mechanics analysis of measured wheel-rail profiles using the finite element method. *Proceedings of the Institution of Mechanical Engineers, Part F: Journal of Rail and Rapid Transit*, 2001. 215(2): p. 65-72.
45. Blanco-Lorenzo, J., J. Santamaria, E.G. Vadillo, and O. Oyarzabal, Dynamic comparison of different types of slab track and ballasted track using a flexible track model. *Proceedings of the Institution of Mechanical Engineers, Part F: Journal of Rail and Rapid Transit*, 2011. 225(6): p. 574-592.
46. Bezin, Y., S. Iwnicki, M. Cavalletti, E. De Vries, F. Shahzad, and G. Evans, An investigation of sleeper voids using a flexible track model integrated with railway multi-body dynamics. *Proceedings of the Institution of Mechanical Engineers, Part F: Journal of Rail and Rapid Transit*, 2009. 223(6): p. 597-607.

47. Pålsson, B.A. A Parameterized Turnout Model for Simulation of Dynamic Vehicle-Turnout Interaction with an Application to Crossing Geometry Assessment. 2020. Cham: Springer International Publishing.
48. Johnson, K.L. and K.L. Johnson, Contact mechanics. 1987: Cambridge university press.
49. Shabana , A.A., M. Berzeri, and J.R. Sany, Numerical Procedure for the Simulation of Wheel/Rail Contact Dynamics. Journal of Dynamic Systems, Measurement, and Control, 2000. 123(2): p. 168-178.
50. Iwnicki, S., Handbook of railway vehicle dynamics. 2006, London: CRC Press.
51. Magalhães, H., F. Marques, B. Liu, P. Antunes, J. Pombo, P. Flores, J. Ambrósio, J. Piotrowski, and S. Bruni, Implementation of a non-Hertzian contact model for railway dynamic application. Multibody System Dynamics, 2020. 48(1): p. 41-78.
52. Piotrowski, J. and W. Kik, A simplified model of wheel/rail contact mechanics for non-Hertzian problems and its application in rail vehicle dynamic simulations. Vehicle System Dynamics, 2008. 46(1-2): p. 27-48.
53. Sh. Sichani, M., R. Enblom, and M. Berg, A novel method to model wheel–rail normal contact in vehicle dynamics simulation. Vehicle System Dynamics, 2014. 52(12): p. 1752-1764.
54. Kalker, J.J., A Fast Algorithm for the Simplified Theory of Rolling Contact. Vehicle System Dynamics, 1982. 11(1): p. 1-13.
55. Menssen, R. and W. Kik, Running through a Switch - Simulation and Test. Vehicle System Dynamics, 1994. 23(sup1): p. 378-389.
56. Drozdziel, J., B. Sowinski, and W. Groll. The effect of railway vehicle-track system geometric deviations on its dynamics in the turnout zone. in 16th IAVSD Symposium Held In Pretoria. 1999. South Africa.
57. Gurule, S. and N. Wilson. Simulation of wheel/rail interaction in turnouts and special track work. in 16th IAVSD Symposium Held In Pretoria. 2000. South Africa.
58. Bruni, S., I. Anastasopoulos, S. Alfi, A. Van Leuven, and G. Gazetas, Effects of train impacts on urban turnouts: modelling and validation through measurements. Journal of Sound and Vibration, 2009. 324(3-5): p. 666-689.

59. Andersson, C. and T. Dahlberg, Wheel/rail impacts at a railway turnout crossing. *Proceedings of the Institution of Mechanical Engineers, Part F: Journal of Rail and Rapid Transit*, 1998. 212(2): p. 123-134.
60. Kassa, E., Simulation of dynamic interaction between train and turnout, in Department of Applied Mechanics. 2004, Chalmers University of Technology: Gothenburg, Sweden.
61. Wiest, M., E. Kassa, W. Daves, J.C.O. Nielsen, and H. Ossberger, Assessment of methods for calculating contact pressure in wheel-rail/switch contact. *Wear*, 2008. 265(9): p. 1439-1445.
62. Kassa, E. and G. Johansson, Simulation of train–turnout interaction and plastic deformation of rail profiles. *Vehicle System Dynamics*, 2006. 44(sup1): p. 349-359.
63. Markine, V.L., M.J.M.M. Steenbergen, and I.Y. Shevtsov, Combatting RCF on switch points by tuning elastic track properties. *Wear*, 2011. 271(1): p. 158-167.
64. Nicklisch, D., E. Kassa, J. Nielsen, M. Ekh, and S. Iwnicki, Geometry and stiffness optimization for switches and crossings, and simulation of material degradation. *Proceedings of the Institution of Mechanical Engineers, Part F: Journal of Rail and Rapid Transit*, 2010. 224(4): p. 279-292.
65. Grossoni, I., Y. Bezin, and S. Neves, Optimisation of support stiffness at railway crossings. *Vehicle System Dynamics*, 2018. 56(7): p. 1072-1096.
66. Xu, J., P. Wang, X. Ma, Y. Gao, and R. Chen, Stiffness Characteristics of High-Speed Railway Turnout and the Effect on the Dynamic Train-Turnout Interaction. *Shock and Vibration*, 2016. 2016.
67. Wan, C., V. Markine, and I. Shevtsov, Improvement of vehicle–turnout interaction by optimising the shape of crossing nose. *Vehicle System Dynamics*, 2014. 52(11): p. 1517-1540.
68. Pålsson, B.A., Design optimisation of switch rails in railway turnouts. *Vehicle System Dynamics*, 2013. 51(10): p. 1619-1639.
69. Bugarín, M. and J.-M. García Díaz-de-Villegas, Improvements in railway switches. *Proc Instn Mech Engrs Part F: J Rail Rapid Transit*, 2002. 216(4): p. 275–286.
70. Kassa, E., S.D. Iwnicki, J. Perez, P. Allen, and Y. Bezin. Optimization of track gauge and track stiffness along a switch using a multibody simulation tool. in *21st International Symposium on Dynamics of Vehicles on Roads and Tracks*. 2009. Sweden, Stockholm.

71. Pålsson, B. and J.C.O. Nielsen, Track gauge optimisation of railway switches using a genetic algorithm. *Vehicle System Dynamics*, 2012. 50(1): p. 365–387.
72. Sällström, J., T. Dahlberg, M. Ekh, and J. Nielsen, State-of-the art study on railway turnouts—dynamics and damage. Department of Applied Mechanics, Chalmers University of Technology, Göteborg, Sweden, 2004.
73. Nissen, A., Development of life cycle cost model and analyses for railway switches and crossings. 2009, Luleå tekniska universitet.
74. Kassa, E. and J.C. Nielsen, Stochastic analysis of dynamic interaction between train and railway turnout. *Vehicle System Dynamics*, 2008. 46(5): p. 429-449.
75. Wiest, M., W. Daves, F. Fischer, and H. Ossberger, Deformation and damage of a crossing nose due to wheel passages. *Wear*, 2008. 265(9-10): p. 1431-1438.
76. Pletz, M., W. Daves, W. Yao, and H. Ossberger, Rolling contact fatigue of three crossing nose materials—Multiscale FE approach. *Wear*, 2014. 314(1-2): p. 69-77.
77. Xin, L., V. Markine, and I. Shevtsov. Analysis approach of turnout crossing performance by field measurements and finite element modeling. in *IAVSD 2015: 24th International Symposium on Dynamics of Vehicles on Roads and Tracks*, Graz, Austria, 17-21 August 2015. 2015. TU Graz.
78. Kassa, E. and J.C. Nielsen, Dynamic interaction between train and railway turnout: full-scale field test and validation of simulation models. *Vehicle System Dynamics*, 2008. 46(S1): p. 521-534.
79. Yang, J., D.J. Thompson, and Y. Takano. Characterizing Wheel Flat Impact Noise with an Efficient Time Domain Model. 2015. Berlin, Heidelberg: Springer Berlin Heidelberg.
80. Thompson, D.J., *Railway Noise and Vibration*. 2008, Oxford: Elsevier Science.
81. ADAMS, M., *Help Documentation (ADAMS/Solver)*.
82. ANSYS, *17.0 help documentation*.
83. Craig, R.R. and M.C.C. Bampton, Coupling of substructures for dynamics Analyses. *AIAA Journal*, 1968. 6 (7): p. 1313-1319.
84. Sellgren, U., Component mode synthesis - a method for efficient dynamic simulation of complex technical systems, in Department of Machine Design. 2003, KTH: Stockholm, Sweden.

85. Hertz, H., Ueber die Berührung fester elastischer Körper. *Journal für die reine und angewandte Mathematik*, 1882. 1882(92): p. 156.
86. Delgado, R. and S. Santos, Modelling of railway bridge-vehicle interaction on high speed tracks. *Computers & Structures*, 1997. 63(3): p. 511-523.
87. Steenbergen, M.J.M.M. and C. Esveld, Rail weld geometry and assessment concepts. *Proceedings of the Institution of Mechanical Engineers, Part F: Journal of Rail and Rapid Transit*, 2006. 220(3): p. 257-271.
88. Hunt, G.A., EUROBALT vertical dynamic model for track damage studies (RR-TCE-035). 1996, British Rail Research: Railway Documentation and Drawing Services Ltd.
89. Iwnicki, S., Manchester benchmarks for rail vehicle simulation. *Vehicle System Dynamics*, 1998. 30(3-4): p. 295-313.
90. Marques, F., H. Magalhães, J. Pombo, J. Ambrósio, and P. Flores, A three-dimensional approach for contact detection between realistic wheel and rail surfaces for improved railway dynamic analysis. *Mechanism and Machine Theory*, 2020. 149: p. 103825.
91. Le Pen, L., G. Watson, A. Hudson, and W. Powrie, Behaviour of under sleeper pads at switches and crossings – Field measurements. *Proceedings of the Institution of Mechanical Engineers, Part F: Journal of Rail and Rapid Transit*, 2018. 232(4): p. 1049-1063.
92. Le Pen, L., G. Watson, A. Hudson, and W. Powrie, Behaviour of under sleeper pads at switches and crossings–Field measurements. *Proceedings of the Institution of Mechanical Engineers, Part F: Journal of Rail and Rapid Transit*, 2018. 232(4): p. 1049-1063.
93. VI-Grade, VI-Rail Help documentation.
94. Kostovasilis, D., Analytical modelling of the vibration of railway track. 2017, University of Southampton: <https://eprints.soton.ac.uk/413811/>. p. 230.
95. Huddersfield, U.o., IRR Report 81/110 - Tram-Train Track Lateral Resistance. 2018.
96. Pandrol, Report No 65101-87, Issue 1: Testing to BS EN 13481-2 on an F40 sleeper fitted with an RE1800 assembly incorporating Pandrol brand studded rubber rail pads type 15496. 17 April 2015.

97. Bezin, Y., I. Grossoni, and S. Neves, Impact of wheel shape on the vertical damage of cast crossing panels in turnouts, in 24th International Symposium on Dynamics of Vehicles on Roads and Tracks. 2015: Graz, Austria.
98. Bowness, D., A.C. Lock, W. Powrie, J.A. Priest, and D.J. Richards, Monitoring the dynamic displacements of railway track. Proceedings of the Institution of Mechanical Engineers, Part F: Journal of Rail and Rapid Transit, 2007. 221(1): p. 13-22.
99. Coelho, B., P. Hölscher, J. Priest, W. Powrie, and F. Barends, An Assessment of Transition Zone Performance. Proceedings of the Institution of Mechanical Engineers, Part F: Journal of Rail and Rapid Transit, 2011. 225(2): p. 129-139.
100. Lamas-Lopez, F., Y.J. Cui, S.C. D'Aguiar, and N. Calon, Assessment of integration method for displacement determination using field accelerometer and geophone data. Journal of Zhejiang University-SCIENCE A, 2017. 18(7): p. 553-566.
101. Le Pen, L., G. Watson, W. Powrie, G. Yeo, P. Weston, and C. Roberts, The behaviour of railway level crossings: Insights through field monitoring. Transportation Geotechnics, 2014. 1(4): p. 201-213.
102. Priest, J.A., W. Powrie, L. Le Pen, P. Mak, and M.C. Burstow, The effect of enhanced curving forces on the behaviour of canted ballasted track. Proceedings of the Institution of Mechanical Engineers, Part F: Journal of Rail and Rapid Transit, 2013. 227(3): p. 229-244.
103. Cross Industry Track Stiffness Working Group, A guide to track stiffness. 2016, Southampton, UK: University of Southampton.
104. Milne, D., J. Harkness, L. Le Pen, and W. Powrie, The influence of variation in track level and support system stiffness over longer lengths of track for track performance and vehicle track interaction. Vehicle System Dynamics, 2019: p. 1-24.
105. Milne, D., L.L. Pen, D. Thompson, and W. Powrie, Automated processing of railway track deflection signals obtained from velocity and acceleration measurements. Proceedings of the Institution of Mechanical Engineers, Part F: Journal of Rail and Rapid Transit, 2018. 232(8): p. 2097-2110.
106. Rail, N., NR/SP/TRK/9039: Business Process Document Formation Treatments. 2005: London.

107. Johansson, A., J.C.O. Nielsen, R. Bolmsvik, A. Karlström, and R. Lundén, Under sleeper pads—Influence on dynamic train–track interaction. *Wear*, 2008. 265(9): p. 1479-1487.
108. Insa, R., P. Salvador, J. Inarejos, and L. Medina, Analysis of the performance of under-sleeper pads in high-speed line transition zones. *Proceedings of the Institution of Civil Engineers - Transport*, 2014. 167(2): p. 63-77.
109. RAIB, Report 04/2018: Freight train derailment at Lewisham. 2018.
110. Grossoni, I., W. Powrie, A. Zervos, Y. Bezin, and L. Le Pen, Modelling railway ballasted track settlement in vehicle-track interaction analysis. *Transportation Geotechnics*, 2021. 26: p. 100433.

APPENDIX A

[4] compared the receptance curves from three discrete models with the load applied at the rail level and on top of a sleeper. The MATLAB model is equivalent to the VTI model presented in chapter 3, a discrete track model with the rail built with a Timoshenko beam formulation. The other two models are equivalent to the discrete track models built in VI-Rail and also presented in chapter 3.

Table A.1. Receptance peak frequencies [4].

	Frequency (Hz)		
	1 st peak	2 nd peak	3 rd peak
MATLAB	100	410	1005
Adams beam	100	410	880
MNF	100	440	835

Figure A.1 shows the receptance curves, while Table A.1 has a comparison from the 3 peaks pointed in Figure A.1. The first peak is the rail bouncing on the ballast and in phase with the sleepers. The second peak is the rail bouncing on the ballast but in out of phase with the sleepers. The third peak identified in Figure A.1 is the pin-pin bending anti-resonance frequency.

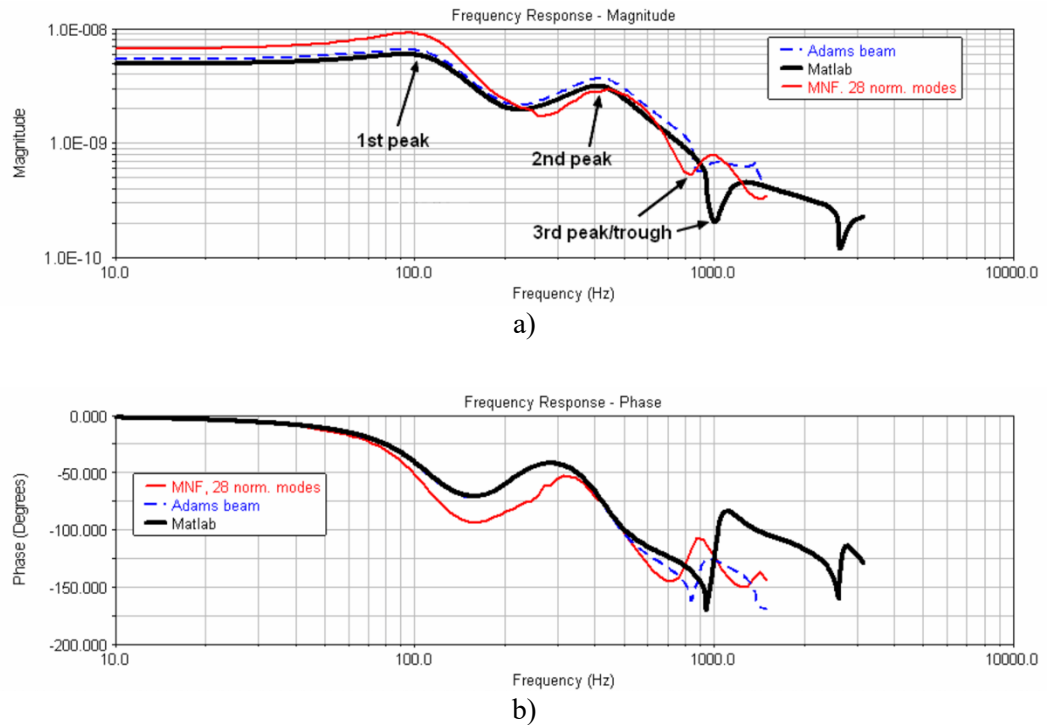


Figure A.1. Receptance curves [4].

APPENDIX B

Table B.2. Final differences and trackbed stiffness values from switch panel for calibration 2.

Bearer	Cess side		6ft side	
	Kb (kN/mm/se)	Disp (%)	Kb (kN/mm/se)	Disp (%)
1	55.46	0.00%	26.93	0.00%
2	84.18	0.00%	14.73	0.00%
3	5.00	-37.12%	5.00	-0.30%
4	5.00	-28.42%	15.65	0.00%
5	6.33	0.00%	17.67	0.00%
6	94.38	0.00%	10.04	0.00%
7	14.69	0.00%	26.99	0.00%
8	27.37	0.00%	31.40	0.00%
9	44.21	0.00%	11.54	0.00%
10	29.55	0.00%	5.00	-0.70%
11	22.52	0.00%	53.56	0.00%
12	9.29	0.00%	32.76	0.00%
13	28.70	0.00%	11.85	0.00%
14	51.17	0.00%	9.25	-0.01%
15	19.44	0.00%	43.59	0.00%
16	5.00	-1.77%	54.78	0.00%
17	49.54	0.00%	43.54	0.00%
18	24.59	0.00%	5.00	-31.47%
19	5.00	-16.97%	97.05	0.00%
20	22.24	0.00%	10.64	-0.04%
21	61.16	0.00%	5.00	-22.96%
22	38.53	0.00%	85.34	0.00%
23	23.02	0.00%	5.00	-9.45%
24	36.25	0.00%	75.61	0.00%
25	27.50	0.00%	5.00	-11.36%
26	5.00	-0.93%	5.00	-35.43%
27	5.00	-5.37%	5.00	-47.04%
28	9.10	-0.01%	5.00	-46.73%
29	23.10	0.01%	5.00	-41.17%
30	8.46	-0.02%	5.00	-35.16%
31	13.75	0.01%	5.00	-39.37%
32	58.02	-0.01%	69.00	0.00%
33	5.00	-13.36%	5.00	-22.77%
34	57.99	0.00%	13.16	-0.06%
35	5.00	-9.52%	48.40	0.02%
36	21.44	0.00%	38.64	0.03%
37	20.38	0.01%	12.87	-0.12%

Table B.3. Final differences and trackbed stiffness values from crossing panel for calibration 2.

Bearer	Cess side		6ft side	
	Kb (kN/mm/se)	Disp (%)	Kb (kN/mm/se)	Disp (%)
38	68.05	0.00%	5.00	-30.41%
39	5.00	-15.30%	5.00	-32.95%
40	26.79	0.00%	5.00	-20.37%
41	10.57	-0.01%	5.00	-33.40%
42	21.85	0.01%	5.00	-8.44%
43	33.11	0.00%	12.33	-0.01%
44	20.25	0.00%	5.00	-41.75%
45	48.55	0.00%	5.00	-67.43%
46	39.38	0.00%	5.00	-57.20%
47	5.00	-13.86%	5.00	-45.71%
48	37.21	0.00%	5.00	-46.78%
49	15.73	0.00%	5.00	-51.79%
50	8.86	0.00%	5.00	-52.39%
51	65.22	0.00%	5.00	-49.46%
52	5.00	-4.72%	5.00	-55.76%
53	27.18	0.00%	5.00	-44.01%
54	73.62	0.00%	5.00	-22.13%
55	5.00	-11.38%	5.00	-35.77%
56	5.00	-22.95%	5.67	-0.11%
57	33.54	0.00%	33.60	0.02%
58	17.87	0.01%	17.64	-0.01%
59	83.35	0.04%	5.00	-21.54%
60	7.96	0.05%	5.00	-33.31%
61	70.48	0.02%	23.30	0.04%
62	22.57	0.00%	22.26	0.01%
63	56.12	-0.02%	5.00	-28.36%
64	51.64	0.02%	5.00	-60.90%
65	39.52	-0.03%	5.00	-73.37%